LORENZ E. ROGNONI

MOLECULAR MECHANISM OF THE MECHANOSENSOR FILAMIN

from Force Sensing to Proline Switches

DISSERTATION AT THE PHYSICS DEPARTMENT E22
TECHNISCHE UNIVERSITÄT MÜNCHEN

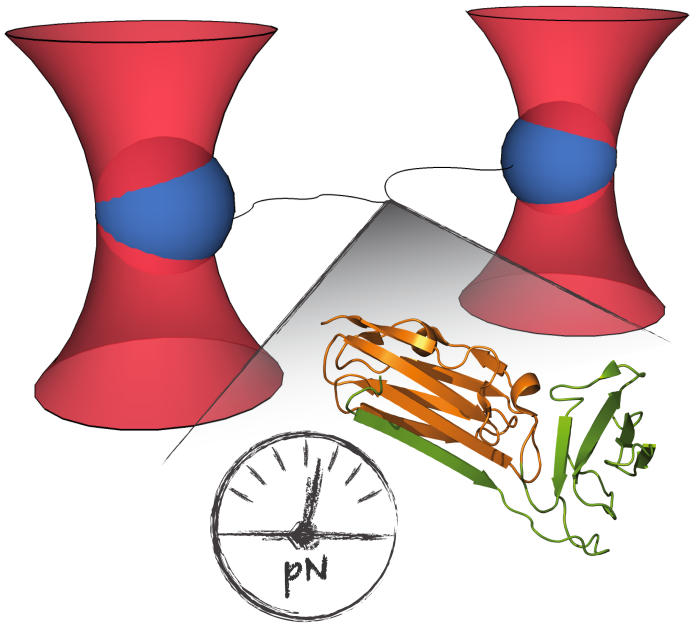

TECHNISCHE UNIVERSITÄT MÜNCHEN
LEHRSTUHL FÜR BIOPHYSIK E22

MOLECULAR MECHANISM OF THE MECHANOSENSOR FILAMIN

from Force Sensing to Proline Switches

LORENZ E. ROGNONI

Vollständiger Abdruck der von der Fakultät für Physik der Technischen Universität München zur Erlangung des akademischen Grades eines

Doktors der Naturwissenschaften (Dr. rer. nat.)

genehmigten Dissertation.

Vorsitzender: Univ.-Prof. Dr. Martin Zacharias

Prüfer der Dissertation: 1. Univ.-Prof. Dr. Matthias Rief

2. Univ.-Prof. Dr. Thorsten Hugel

Die Dissertation wurde am 15.05.2014 bei der Technischen Universität München eingereicht und durch die Fakultät für Physik am 11.06.2014 angenommen.

ABSTRACT

Mechanical forces are important signals for cell response and development, but detailed molecular mechanisms of force sensing are largely unexplored. In parallel, proline switches, controlled by *cis–trans* isomerization, have emerged as a particularly effective regulatory mechanism in a wide range of biological processes. Both aspects, mechanosensing and proline switches, directly affect filamin, an abundant cytoskeletal protein that constitutes a key connecting element between the cytoskeleton and transmembrane complexes such as integrins or the von Willebrand receptor glycoprotein Ib.

The research presented here uses single-molecule mechanical measurements to show that the recently reported Ig-like domain pair 20–21 of human filamin A acts as an autoinhibited force-activatable mechanosensor. A newly developed mechanical single-molecule competition assay allows online observation of binding events of target peptides in solution to the strained domain pair. We find that filamin force sensing occurs in rapid equilibrium and that it increases the binding affinity for target peptides by up to a factor of 17 between 2 and 5 pN.

Furthermore, this work develops a full kinetic and energetic description of a highly conserved proline switch in the force-sensing domain 20 of human filamin and shows how prolyl isomerization modulates the force-sensing mechanism. Proline isomerization toggles domain 20 between two conformations: a stable *cis* conformation with slow unfolding, favoring the autoinhibited closed conformation of the force-sensing domain pair 20–21, and a less stable, uninhibited conformation promoted by the *trans* form. The data provide detailed insight into the folding mechanisms that underpin the functionality of this binary switch and elucidate its remarkable efficiency in modulating force sensing, and thus combine two previously unconnected regulatory mechanisms, proline switches and mechanosensing. A final set of experiments studies the catalytic effect of peptidyl-prolyl *cis/trans* isomerases on the proline switch of domain 20. This adds an additional step in regulatory complexity and enables us to study enzyme catalysis at the single-molecule level.

The mechanisms reported here can offer a general scheme for cellular force sensing and proline mediated regulation involving isomerases.

ZUSAMMENFASSUNG

Mechanische Kräfte sind wichtige Signale für die Regulierung und Entwicklung von Zellen. Die zugrundeliegenden molekularen Mechanismen der zellulären Kraftmessung bleiben jedoch weitgehend unerforscht. Gleichzeitig haben sich Prolinschalter, die durch eine *cis-trans* Isomerisierung gesteuert werden, als besonders wirksame Regulierungsmechanismen in einer Vielzahl von biologischen Prozessen hervorgetan. Beide Effekte, Kraftmessung und Prolinschalter, haben einen direkten Einfluss auf Filamin. Dieses reichlich vorhandene Zytoskelettprotein stellt ein wichtiges Verbindungselement zwischen dem Zytoskelett und Transmembrankomplexen wie Integrinen oder dem von Willebrand Rezeptor Glykoprotein Ib dar.

Die hier vorgestellte Arbeit verwendet mechanische Einzelmolekül-Messungen um zu zeigen, dass die Ig-artigen Domänen 20-21 aus humanem Filamin A einen Kraftsensor bilden. Ein neu entwickeltes mechanisches Einzelmolekül-Kompetitionsexperiment ermöglicht die Echtzeitbeobachtung von Bindungsereignissen zwischen gelösten Zielpeptiden und einem unter Kraft stehenden Domänenpaar. Die Kraftmessung des Domänenpaars erfolgt in einem Bereich zwischen 2 und 5 pN als dynamischer Gleichgewichtsprozess, der die Bindungsaffinität für Zielpeptide um bis zu 17-fach erhöht.

Darüber hinaus beinhaltet diese Arbeit eine vollständige kinetische und energetische Charakterisierung eines hoch konservierten Prolinschalters, der sich in Domäne 20 von humanem Filamin befindet und den Kraftsensor-Mechanismus moduliert. Die Prolinisomerisierung schaltet Domäne 20 zwischen zwei Konformationen: eine stabile *cis* Konformation mit langsamer Entfaltungskinetik begünstigt den autoinhibierten geschlossenen Zustand des Kraftsensor-Domänenpaars 20-21; und eine weniger stabile, nicht inhibierte Konformation, die durch die *trans* Isoform verursacht wird. Die Daten liefern detaillierte Einblicke in den Faltungsmechanismus, der die Funktion dieses binären Schalters beherrscht, und erläutern seine bemerkenswerte Effizienz bei der Modulation des Kraftsensors. Die Forschungsergebnisse verbinden somit bisher getrennte Regulationsmechanismen, Prolinschalter und molekulare Kraftsensoren.

Eine weitere Reihe von Experimenten untersucht die katalytische Wirkung von Peptidyl-Prolyl *cis/trans* Isomerasen auf den Prolinschalter in Domäne 20. Dies erhöht die regulatorische Komplexität um einen weiteren Schritt und ermöglicht es, Enzymkatalyse auf der Einzelmolekülebene zu untersuchen.

Die hier erforschten Mechanismen liefern ein allgemeines Modell für zelluläre Kraftmessung und isomerisierungsabhängige Regulation in Gegenwart von Isomerasen.

PUBLICATIONS

Some ideas and figures have been adapted from the following publications:

Rognoni, Stigler, Pelz, Ylänne, and Rief (2012) Dynamic force sensing of filamin revealed in single-molecule experiments. *Proc Natl Acad Sci USA.* [91]

Rognoni, Möst, Zoldak, and Rief (2014) Force-dependent isomerization kinetics of a highly conserved proline switch modulates the mechanosensing region of filamin. *Proc Natl Acad Sci USA.* [92].

ACKNOWLEDGMENTS

A number of people helped, directly or indirectly, to realize the work presented here. First of all, I want to thank *Matthias Rief*, my supervisor, for all the helpful, encouraging and inspiring discussions. At E22 he created a unique lab atmosphere – relaxed, creative, and efficient at the same time. The freedom for original ideas paired with the highest standard for data quality have contributed essentially to my scientific development.

In this context, I also want to mention and thank *Morten Bertz*. He introduced me to almost everything in my early stages at E22, and taught me all I needed about biochemistry, cloning and working in a wet lab.

Special thanks go to following people, who directly contributed to the successful termination of my various research projects: *Jari Ylänne* first proposed the autoinhibition mechanism of filamin and contributed with many fruitful discussions; *Gabriel Zoldak* is an expert of proline isomerization and especially the isomerase SlyD and helped a lot in the corresponding projects. As my Bachelor student, *Tobias Möst* demonstrated his talent and endurance by spending innumerable hours in the basement, helping me with the hunt for the perfect over-one-hour-trace.

Whenever I ran the risk of getting lost between physics, biology, chemistry and data analysis, a number of people always helped me out with inspiring discussions and hands-on contributinos: *Johannes Stigler, Christoph Gebhardt, Fabian Ziegler, Tessa Sinnige, Benjamin Pelz, Ziad Ganim, Anja Gieseke, Alexander Mehlich, Uli Merkel* and *Marco Grison*. A special thank goes again to *Ziad Ganim*, who read and improved all my manuscripts and together with *Johannes Stigler* was a great office mate. For all of their technical help, I want to thank *Monika Rusp, Gabi Chmel, Karin Vogt* and *Rudi Lehrhuber*. Additionally, *Elke Fehlsenfeld* and *Nicole Mittermüller* helped me repeatedly to circumvent the pitfalls of bureaucracy.

A big thank goes of course to everybody in the bio corner: all members of the *Rief, Bausch, Hugel* and *Woehlke* groups made my stay at E22 more than a working experience. Especially the winter schools, christmas parties and various "special" seminars were unforgettable.

Finally, I want to thank my family, especially my parents, who supported me and my passion for science from the very beginning until now. During my physics studies my brother enthused me for his field of studies, biochemistry. This ultimately brought me to the thrilling field of biophysics and I thank him for this inspiration. In the end, I particularly thank my girlfriend *Inga Dahl* for assistance in all circumstances.

CONTENTS

LIST OF FIGURES

LIST OF TABLES

Part I

INTRODUCTION AND BACKGROUND INFORMATION

In the first part of this thesis, I give specific background information about the field of research and the open questions that led to the investigations presented here.

1 INTRODUCTION

The ability of cells to react and adapt to changing environmental conditions is based on the capability to sense and process signals, which can be chemical, optical or even electrical in the case of nerve cells. In recent years, mechanical forces have also been identified as important signals for cell development and cytokinesis. For example, mechanical signals have crucial implications for processes such as stem cell differentiation [29] or the remodeling of cardiac muscle tissue [45]. Even though the sensing of mechanical forces has been postulated in various contexts, molecular mechanisms of force sensing have remained to a large degree elusive. The emerging picture can be summarized in that cells contain various mechanosensing components that transduce mechanical signals into biochemical cascades. When cells adhere to the extracellular matrix (ECM), a complex network of molecules mechanically couples the ECM to the cytoskeleton, which is the main force-bearing structure in cells. The filaments constituting the cytoskeleton, namely actin, intermediate filaments and microtubules, along with their cross-linkers are again all mechanically linked and therefore participate in cell mechanotransduction. At the cell exterior, several transmembrane receptors specifically recognize ECM molecules. The main ECM-cell connectors are integrins, which bind to the ECM molecules fibrinogen and fibronectin. On the intracellular side, integrins are linked with their cytosolic end to the actin cytoskeleton through integrin–actin cross-linker proteins. One major actin cross-linker is the dimeric protein filamin that also acts as a signaling hub for various proteins [80]. Two prominent examples of interaction partners involved in mechanotransduction are the aforementioned integrins [36, 35, 56] or glyco protein 1 b (GPIb), a constituent of a transmembrane complex found in platelets that binds to von Willebrand factor during blood clotting [94, 81, 47]. Both the filamin-integrin and the filamin-GPIb interactions have been shown to be exposed to mechanical forces in living cells [73, 19]. The filamin monomer consists of a N-terminal actin-binding domain and a sequence of 24 immunoglobulin-like (Ig-like) domain repeats that form the filamin rod. Within the rod 2 region (Ig-like domains 16-23), filamin can interact with transmembrane protein complexes, thus establishing a mechanical connection between the cytoskeleton and the extracellular side. This puts filamin in an ideal position for mechanotransduction and, as shown in Chapter 7, mechanosensing. The major interaction sites within rod 2 are the odd numbered domains, specifically domains 17, 19 and 21. In contrast to the linear arrangement of domains found in many structural proteins like titin,

fibronectin or rod 1 of filamin, the Ig-like domains 18-21 of filamin's rod 2 are arranged in pairs [65, 42]. In those pairs, the even numbered domains bind to the subsequent odd-numbered domain thus inhibiting the interaction of this domain with its peptide ligand. It has been proposed that this special arrangement into domain pairs effects a force-sensing mechanism in filamin [84, 65].

A further remarkable molecular detail of filamin is a highly conserved native *cis* peptidyl-prolyl bond located in front of the last β-strand of all structurally reported filamin Ig-like domains. Owing to its ring structure, the peptidyl-prolyl bond is special among the peptide bonds in that it can populate slowly exchanging *cis* and *trans* conformations with similar probability [117]. Therefore, proline residues can drastically affect the kinetics of folding [9, 10] as well as conformational changes of proteins [71, 26]. Although most native protein conformations require *trans* prolines, there are a number of examples where native *cis* prolines have been reported [117, 59, 114, 14]. In a few cases, both *cis* and *trans* conformations can be accommodated in the folded state thus leading to two distinct native states [53, 83, 96]. Beyond its importance for protein folding, peptidyl-prolyl isomerization has also been discussed as a molecular timer switch regulating different functional conformations of proteins [26, 70]. The slow isomerization can be accelerated in organisms by an abundant class of enzymes known as peptidyl-prolyl *cis/trans*-isomerases.

The custom-built extremely stable high-resolution optical tweezers used in this work enable us to measure and apply small pN-forces to a single biomolecule for up to one hour. The force-dependent conformational changes of the molecule can be followed with a sub ms time resolution and nm precision. With this powerful technique, we can directly study the molecular mechanisms involved in mechanosensing at the single-molecule level. Thus, we can contribute to laying the groundwork for a quantitative understanding of mechanosensing.

THESIS OUTLINE

This thesis is divided into three parts. In the first part, I provide background information about the field of research and the applied single-molecule techniques. In Chapter 2 filamin is introduced in more detail. This will be followed by a chapter about proline isomerization and isomerases (Chapter 3).

In the second part, I present different techniques used to measure and apply forces to biomolecules (see Chapter 4). Also a more detailed introduction to optical tweezers along with common measurement techniques is provided. Chapter 5 introduces the theoretical models as well as analytical methods necessary for the data analysis.

The third part summarizes and discusses the research results. I developed and performed single-molecule mechanical measurements presented in Chapter 6, which provide a complete kinetic and energetic characterization of the multireceptor binding site found in domain 21 of human filamin A. The interaction of three different binding partners with domain 21 was studied; namely GPIbα and β7 integrin, which are involved in mechanotransduction, as well as the integrin regulator migfilin. I was able to measure the mechanical stability of those interactions under load as well as the zero-load on- and off-rates. This revealed a clear hierarchy of mechanical stabilities governed by different off-rates. In Chapter 7 I provide direct experimental evidence for a force-sensing mechanism of human filamin A. Mechanical single-molecule experiments show quantitatively how force increases the binding rate of interaction partners by shifting the conformational equilibrium of the autoinhibited filamin domain pair 20-21. A detailed investigation of the proline dependent folding of domain 20 is carried out in Chapter 8. We completely characterize a kinetic network comprising four different states and discuss the resulting regulatory consequences for the force-sensing region of filamin. Furthermore, I introduce the first direct measurement of the force-dependent *cis/trans* isomerization carried out with a single peptidyl-prolyl bond. Finally, Chapter 9 presents the experimental findings of the regulatory effect of various peptidyl-prolyl *cis/trans* isomerases on the folding and isomerization behavior of domain 20 of human filamin A.

In summary, this thesis covers various aspects of the domain pair 20-21 of human filamin A and emphasizes the complex and versatile behavior caused by only two domains of a much larger protein. It further combines two previously unconnected regulatory mechanisms, mechanosensing and proline switches.

2 FILAMIN

Filamins are conserved, modular, multidomain proteins associated with the cytoskeleton. Apart from being potent actin cross-linkers, they interact with various structural and signaling proteins. Thus, they contribute to the link between the extracellular matrix (ECM) and the cytoskeleton, and at the same time act as scaffolds for a wide range of signaling pathways. Due to these characteristics, filamins are well positioned to serve as mechanosensors.

2.1 ISOFORM OCCURRENCE AND STRUCTURE

The vertebrate filamin family belongs to the class of actin binding proteins and consists of three isoforms: filamin A (`FLNa`), filamin B (`FLNb`) and filamin C (`FLNc`). `FLNa` and `FLNb` are widely expressed during development and show similar cellular and tissue expression patterns [88]. In contrsat, `FLNc` is restricted largely to cardiac and skeletal muscles.

All vertebrate filamins are large homodimers of 240 to 280 kDa-subunits that associate at their carboxy termini. Each filamin monomer consists of an amino-terminal actin-binding domain followed by 24 β-pleated sheet immunoglobulin-like domains interrupted by two flexible hinge regions between domains 15-16 and 23-24 (see Figure 1). The hinge regions subdivide filamin into a rod 1 (domains 1-16) and a rod 2 region (domains 16-23) followed by the terminal dimerization domain 24. In contrast to the linear arrangement of domains found in many structural proteins like titin, fibronectin or rod 1 of filamin, the domains 18-21 of filamin are arranged in pairs [65, 43]. In those pairs, the A-strand of the even numbered domains is not integrated into the domain structure but binds to the subsequent odd-numbered domain (see crystal structure of FLNa20-21 shown in Figure 2B).

Nomenclature: Individual filamin domains are specified by an abbreviation for the species preceding `FLN` and followed by the type of isofrom (`a`, `b` or `c`) and the domain number, e.g. `hsFLNa21` for domain 21 of human filamin A. For this thesis, only human filamin was investigated and the species abbreviation is therefore omitted.

2.2 INTERACTION PARTNERS

More than 90 binding partners are reported for filamin, including intracellular signaling molecules, receptors, ion channels, transcription factors, and cytoskeletal and adhesion proteins [80]. Two prominent examples for transmembrane receptors involved in mechanotransduction are integrins [36, 35, 56] and glyco protein 1 b (GPIb) [94, 81, 47]. Integrins are essential adhesion receptors found on the surfaces of all metazoan cells. As regulators of cell migration and extracellular matrix assembly, these membrane-spanning heterodimers are critical

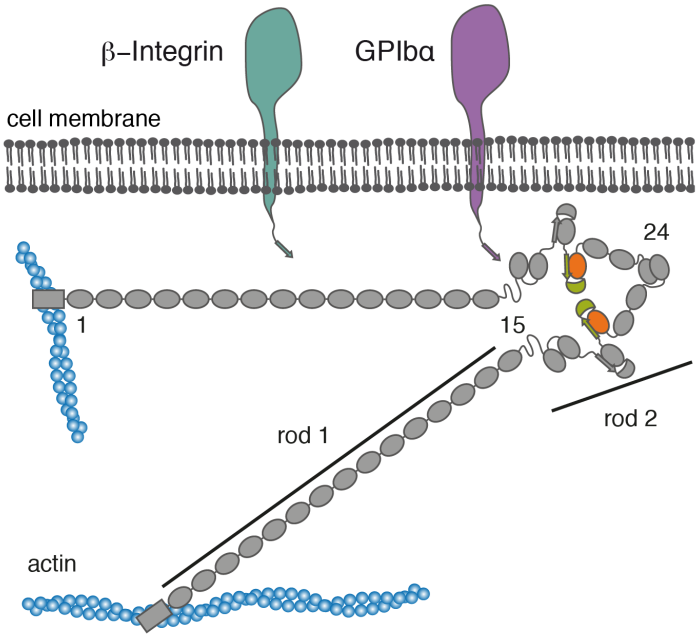

Figure 1: Schematics of the domain arrangement of filamin and its interaction with the transmembrane proteins integrin and GPIbα. Filamin consists of 24 immunoglobulin-like domains that dimerize at domain 24 and carry an N-terminal actin-binding domain. In its rod 2 region (Ig-like domains 16-24), domains 16-21 (FLNa16-21) arrange in pairs that contain binding sites for integrins (dark green) and GPIbα (purple). The domain pair FLNa20-21 is highlighted in orange and green.

for embryonic development, tissue repair and immune responses. Signals transmitted by integrins from outside to inside the cell promote cell survival and proliferation, but integrin affinity for extracellular ligands can also be controlled by intracellular cues. This bidirectional signaling is mediated by the short cytoplasmic tails of the two integrin subunits. GPIb is a constituent of a transmembrane complex found in platelets that binds to von Willebrand factor during blood clotting.

It was shown that apart from the actin binding most of the interactions take place within the rod 2 region (domains 16 to 23) [51, 80]. By binding actin and a transmembrane receptor at the same time, filamin can establish a mechanical connection between the cytoskeleton and the extracellular side. Both the filamin-integrin and the filamin-GPIb interactions have been shown to be exposed to mechanical forces in living cells [73, 19]. The major interaction sites within rod 2 are the odd numbered domains, specifically domains 17, 19 and 21. The transmembrane interaction partners bind to these domains through a C-terminal peptide sequence that forms an additional β-strand extending the β-sheet structure of the domain [79, 60]. A crystal struc-

ture of the complex formed by the C-terminal end of β7 integrin and FLNa21 is shown in Figure 2C.

2.3 AUTOINHIBITION AND MECHANOSENSING

The pairwise arrangement introduced previously implicates that the even numbered domains 18 and 20 cover the binding site of the subsequent domains 19 and 21, thus autoinhibiting the interaction with ligands such as integrins and GPIbα.

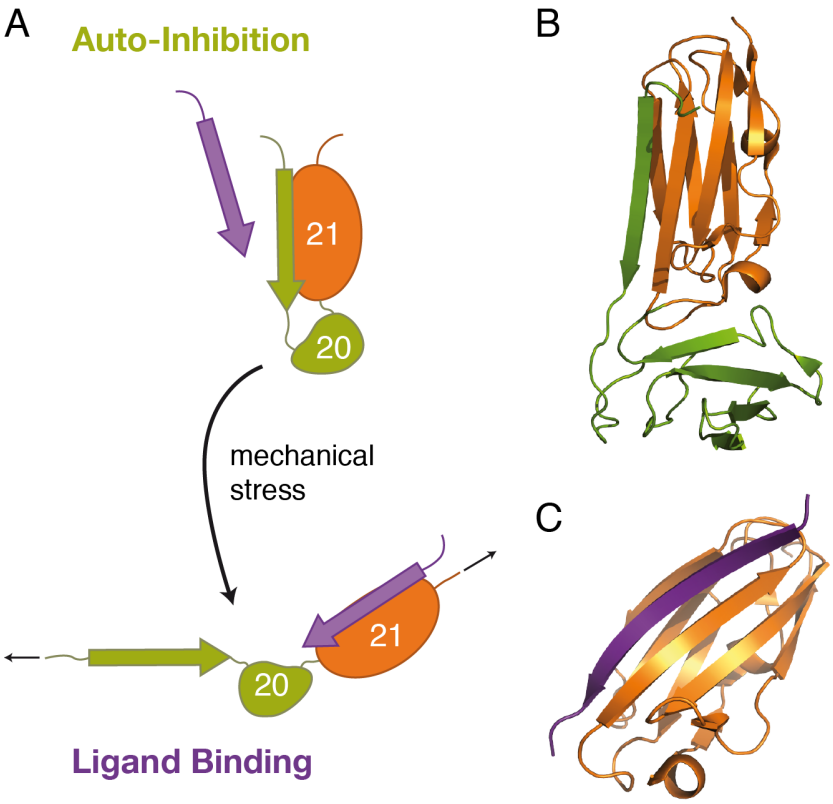

Figure 2: (A) The A-strand of FLNa20 binds to FLNa21 thus autoinhibiting its interaction with the transmembrane proteins. It has been hypothesized that mechanical stress releases the autoinhibition and promotes interaction with binding targets. (B) Crystal structure (adapted from pdbID: 2J3S) of the domain pair 20-21 of human filamin A showing the autoinhibited state. (C) Crystal structure (pdbID: 2BRQ) of domain 21 of human filamin A showing the ligand-bound state. The purple β-strand represents the binding region of the transmembrane receptor integrin β7.

According to numerous studies, filamins play an important role in various mechanical cell processes, including cell motility, membrane stability, mechanoprotection, and ECM stiffness sensing [88]. On a molecular level, it has been proposed that the special pairwise arrangement of rod 2 domains effects a force-sensing mechanism in fil-

amin [84, 65]. Recent *in vitro* studies of mechanically strained filamin-crosslinked actin networks have provided further support for a potential force-sensing role of filamin [27]. The proposed mechanism is shown in Figure 2A. Mechanical stress originating from a stressed actin network acts along the cross-linking filamin and causes the detachment of the covering A-strand. This exposes the binding site of the subsequent domain to potential ligands, thus transducing a mechanical signal into a chemical. First, we will address the interaction of the uninhibited binding site of FLNa21 with integrin $\beta 7$, GPIbα and migfilin (Chapter 6). In Chapter 7 we will turn towards the central question whether the autoinhibition is released by force.

3

PROLINE ISOMERIZATION AND PEPTIDYL-PROLYL ISOMERASES

Proteins are chains of amino acids held together by peptide bonds. These are covalent chemical bonds formed during protein synthesis when a carboxyl group of one amino acid reacts with the amino group of another amino acid under release of one water molecule. Significant delocalization of the lone pair of electrons on the nitrogen atom gives the group a partial (40 %) double bond character (see Figure 3). The partial double bond renders the amide group planar, occurring in either the *cis* or *trans* isomer [70]. In proteins nearly all (1000 : 1) peptide bonds occur in the *trans* isoform [105].

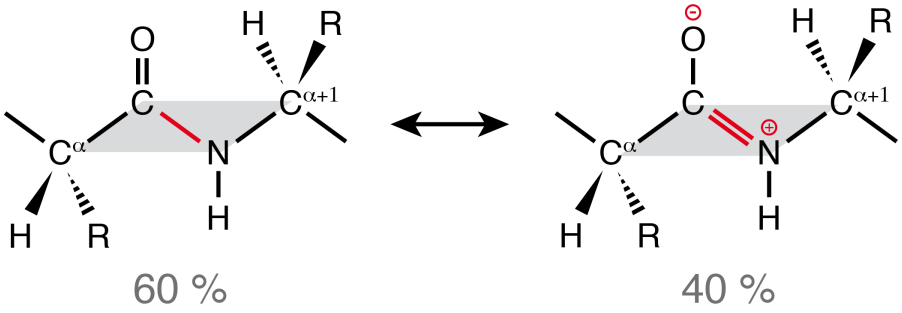

Figure 3: Due to delocalized electrons the peptide bond shown in red is a partial double bond. This leads to a stiff planar structure (grey shaded area).

3.1 PROLINE ISOMERIZATION

Peptidyl-prolyl bonds are formed by an arbitrary amino acid followed by a proline, which are special amongst all amino acids due to their ring structure formed when the residue binds back to the peptide backbone. The resulting rigidity and steric hindrance enables the peptidyl-prolyl bond to populate the *cis* and *trans* conformation with similar probabilities. Because of a high barrier separating both conformations, the interconversion is rather slow, usually on the order of minutes [117]. Figure 4 illustrates the structural and energetic changes during peptidyl-prolyl *cis/trans* isomerization. The folding structure of a protein is usually sensitive to the isoform of the involved peptide bonds and in most cases the *trans* conformation is required. Therefore, proline residues can drastically affect the kinetics of folding [9, 10] as well as conformational changes of proteins [72, 26]. While most native protein conformations require *trans* pro-

Note that in the following peptidyl-prolyl cis/trans isomerization will be referred to by prolyl *or* proline isomerization. *Also the term* proline switch *will be used synonymously.*

lines, there are a number of examples where native *cis* prolines have been reported [120, 59, 114, 14, 117]. In a few cases, both *cis* and *trans* conformations can be accommodated in the folded state thus leading to two distinct native states [53, 83, 96]. Beyond its importance for protein folding, peptidyl-prolyl isomerization has also been discussed as a molecular timer switch regulating different functional conformations of proteins [26, 70].

While proline isomerization has been investigated in numerous bulk studies, the structural heterogeneity caused by a native state isomerization cannot be detected in crystal structures. Even in NMR experiments, native state isomers can only be detected if both states are considerably populated at equilibrium. Recent advances allowing the folding of individual protein molecules to be observed over hours using optical trapping experiments make it possible to observe slow processes, such as proline isomerization events. During the investigations presented in Chapter 7 we discovered a highly conserved native *cis* proline in filamin, which affects unfolding of domain 20, thus modulating the mechanosensing region of filamin. This proline switch will be addressed in Chapter 8.

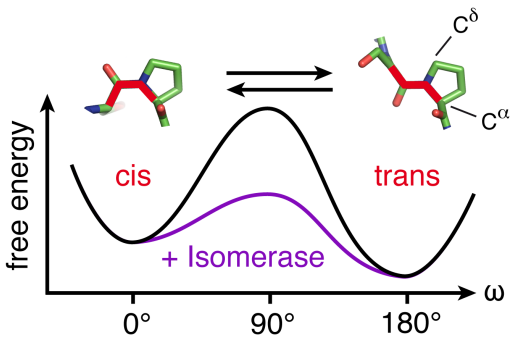

Figure 4: Structural and energetic scheme of *trans* and *cis* isoform of an Xaa-Pro bond. The purple energy landscape shows the reduced barrier upon addition of a peptidyl-prolyl *cis/trans* isomerase.

3.2 PEPTIDYL-PROLYL ISOMERASES

As mentioned above, the intrinsically slow isomerization can trap proteins in undesired conformations or prevent correct folding. Cells can overcome this with the help of a class of enzymes called peptidyl-prolyl *cis/trans* isomerases (PPIases), which catalyze isomerization by lowering the barrier separating the *cis* and *trans* isoform as shown in Figure 4. This speeds up the interconversion rate between the *cis* and *trans* states by several orders of magnitude. PPIases divide into four structurally unrelated families: cyclophilins (Cyps), FK506-binding proteins (FKBPs), parvulins and the protein Ser/Thr phosphatase 2A (PP2A) activator PTPA. Cyclophilins and FKBPs have been the subject

of intense research because they are cellular targets for the clinically used immunosuppressive drugs cyclosporin A (CsA) and FK506, respectively. FKBPs are also targets for the immunosuppressant and anticancer agent rapamycin [70].

3.2.1 *Cyclophilin*

Cyclophilins are a family of ubiquitous proteins from vertebrates and other organisms, which bind with high affinity to the immunosuppressant cyclosporine A and in addition exhibit peptidyl-prolyl isomerase activity [100]. Cyclophilin A (CypA) is a highly abundant

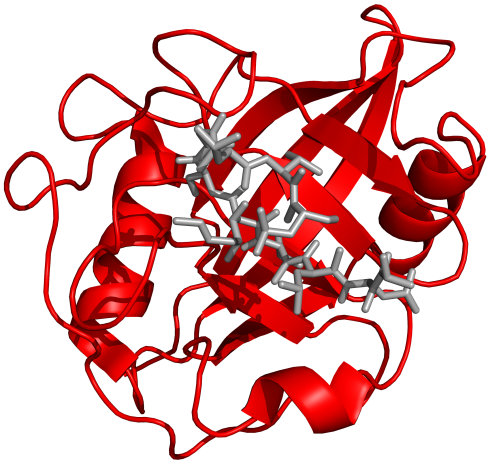

Figure 5: X-ray structure (pdbID: 1CWA) of peptidyl-prolyl *cis/trans* isomerase Cyclophilin A in complex with its inhibitor Cyclosporin A. The isomerase domain is colored in red while the inhibitor is depicted in grey.

member of the cyclophilin family found in the cytosol. It has a β barrel structure with two α helices and a β-sheet. An X-ray structure of CypA in complex with Cyclosporin A is given in Figure 5. It was speculated that the function of cyclophilins in immunosuppression might be linked to prolyl isomerase activity. However, subsequent work indicated that this was not the case. First, yeast mutants lacking cyclophilin A are viable and cyclosporin resistant, indicating that cyclophilin is not essential, and both the protein and the inhibitor are required for drug action [113, 11]. Second, the binary complex between CsA and CypA was found to bind and inhibit the phosphatase calcineurin [67, 31]. Calcineurin inhibition is thought to suppress organ rejection by halting the production of the pro-inflammatory molecules TNF αand interleukin 2.

3.2.2 *SlyD*

In this study, one member of the FKBP family was investigated in more detail. The two-domain protein SlyD (sensitive-to-lysis protein D) of *Escherichia coli* functions as a molecular chaperone, a prolyl *cis/-trans* isomerase, and a nickel-binding protein [64]. Figure 6 shows a solution structure (pdbID: 2K8I) of SlyD with the chaperone domain being colored in blue and the FKBP-like isomerase domain being colored in red [119]. In contrast to filamin presented in Chapter 2, which exhibits a linear arrangement of all domains, the 60 residues comprising chaperone domain is inserted between β-strands 2 and 3 of the 90-residues FKBP domain. In human FKPP12 β-strands 2 and 3 are connected by a loop, which is called the flap. Hence, in SlyD the inserted chaperone domain is also known as the insert-in-flap (IF) domain. The FKBP domain of SlyD is a structural homologe of human FKBP12. In addition to the well-structured two domains, WT

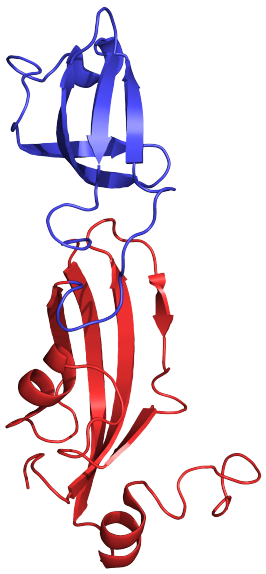

Figure 6: Solution structure (pdbID: 2K8I) of peptidyl-prolyl *cis/trans* isomerase SlyD. The upper chaperone domain is colored in blue while the lower isomerase domain is depicted in red.

Escherichia coli SlyD has also a C-terminal disordered 40 residues long histidine-rich tail that can bind up to 7 nickel ions [58]. In the presence of metal ions, this tail interferes with the isomerase activity of SlyD and can reduce the *in vitro* solubility. For the here presented work only the well described shortened version SlyD* was used, which lacks the disordered tail [101, 127].

3.2.3 *SlyD as a catalyst of protein folding*

In various studies the catalytic activity of SlyD as a folding enzyme was investigated by using the reduced and carboxymethylated form of the S54G/P55N variant of RNase T1 (RCM-T1) as a substrate [101, 69, 125, 128]. RCM-T1 contains only a single *cis* prolyl bond (Tyr38-Pro39) and is unfolded in the absence of salt. Refolding can be initiated by a jump to high salt conditions (2 M NaCl) in the absence of denaturants. During folding a fast ($\tau = 0.7$ s at 15 °C, pH 8.0) and a slow ($\tau = 530$ s) phase are observed [78, 77]. The slow phase is caused by the non-native *trans* Pro39 and the required rate-limiting isomerization step to *cis* before folding. SlyD* catalyzes the folding of RCM-T1 and a Michaelis-Menten type analysis gives a K_M value of 1.7 µM and a k_{cat} of 0.7 s^{-1} [125]. The k_{cat} value for the isomerization of short tetrapeptides by SlyD* is about 100 s^{-1} [62, 125], and the rate of catalyzed prolyl isomerization in RCM-T1 in the SlyD-bound state is also 100 s^{-1} or higher, which suggests that the rate of prolyl isomerization in the SlyD-bound state is similarly high for peptides and for bound protein chains. The measured k_{cat} for the SlyD-catalyzed folding of RCM-T1 is more than 100-fold lower. Thus, the overall reaction is not limited by the catalytic step itself, but instead the rate of folding of RCM-T1 after the release from SlyD* (1.4 s^{-1} [125]) might be a major determinant for the measured k_{cat} value. With these catalytic properties, SlyD resembles trigger factor, a prolyl isomerase that is located at the exit site of the ribosome and is thought to aid in the folding of newly synthesized protein chains. This indicates that both isomerases use a similar mechanism in the catalysis of proline-limited folding.

Throughout this study a shortened version of the 196-residues WT SlyD was used. SlyD corresponds to residues 1 to 165 followed by a hexa-His tag.*

Both the FKBP and the IF domain are required for the catalysis of folding of protein substrates. Deletion of the IF domain from SlyD decreased the activity towards catalysis of the refolding of RCM-T1 100-fold, and the artificial insertion of the IF domain of SlyD into human FKBP12 increased this folding activity by a factor of 200. Remarkably, the prolyl isomerase activities, as measured with short peptides, were independent of deleting or inserting the IF domain [62]. SlyD proteins from other species resemble SlyD from *Escherichia coli* in their catalytic properties [101].

3.2.4 *Substrate binding to SlyD is highly dynamic*

Scholz et al. demonstrated that SlyD binds only the unfolded polypeptide chain with high affinity. To measure substrate binding uncoupled from folding catalysis, Zoldak and Schmid used a permanently unfolded version of the substrate RCM-T1, which can be achieved by introducing the strongly destabilizing substitution P39A [101]. It contains a single tryptophan (W59) that serves as energy donor in FRET-

based binding experiments. SlyD* is devoid of tryptophan and cysteine. To introduce an energy acceptor into SlyD*, Zoldak and Schmid produced variants with single-cysteine residues at different positions and labeled them with an 5-(((acetylamino)ethyl)amino)naphthalene-1-sulfonate (AEDANS) group, which can accept energy from Trp via FRET. The interaction of the unfolded protein RCM-T1-P39A with SlyD* is characterized by a K_D value of about 0.5 µM [125]. Presumably, substrate binding determines the K_M value of catalyzed folding (1.7 µM). As a comparison, the reduced and carboxy-methylated form of α-lactalbumin, which is also permanently unfolded, binds with similar affinity to SlyD* [101]. Binding and release of RCM-T1-P39A from SlyD* is extremely dynamic. The rate of association is $24 \times 10^6\,M^{-1}\,s^{-1}$ [125], which is about 100-fold higher than the expected rate of association between two folded proteins [102]. The dissociation rate is also very high ($k_{off} = 25\,s^{-1}$) [125], and thus, the lifetime of the complex between the IF domain and the substrate protein is only 40 ms.

3.2.5 *Domain movement and catalysis*

Studies of the domain dynamics of SlyD by NMR [63] and single-molecule FRET [57] experiments indicate a correlated motion of IF and FKBP domain, which is thought to facilitate an efficient prolyl *cis/trans* catalysis. This domain motion is a generic property of the enzyme and is already present in the free form without substrate. For the single-molecule FRET experiments, where fluorescence donor and acceptor were placed in different domains of SlyD, the transfer efficiencies showed a broad distribution of distances with two maxima that were assigned to an open and a closed conformation, respectively. These states exchanged with a rate much higher than the substrate turnover rate k_{cat}.

These dynamics studies together with the substrate binding results can be summarized in the current mechanistic view of the SlyD enzyme function shown in Figure 7. Before catalysis, the substrate first binds unspecifically to the IF domain. The opening and closing movement of the two domains positions the substrate in proximity to the isomerization site in the FKBP domain. This occurs at a rate much faster compared to k_{cat}, indicating that many openings and closings take place before the substrate turns over. In other words, SlyD can sample various orientations and conformations in close proximity to the catalytic center.

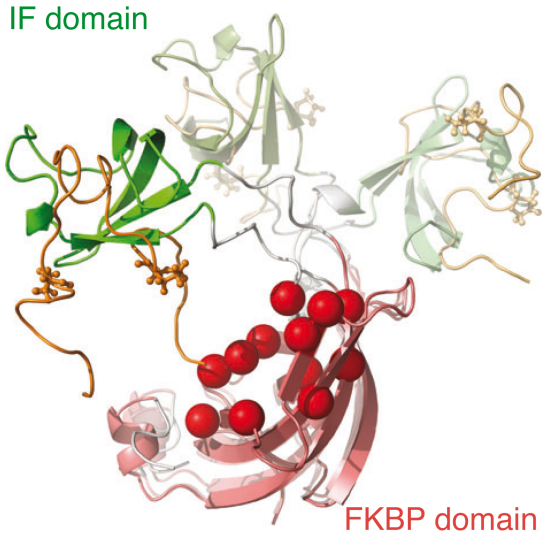

Figure 7: Mechanistic model of SlyD catalysis. Residues forming the catalytic site in the red colored FKBP domain are indicated by spheres. A putative substrate (brown) binds prior to isomerization to the IF domain (green), which moves between an open and closed state relative to the FKBP domain (adapted from [64]).

Part II

EXPERIMENTAL APPROACH, THEORY AND METHODS

In the second part of my thesis, I motivate and describe the experimental approach chosen. The underlying theoretical concepts and experimental procedures are presented as well. I especially emphasize some adaptations of common techniques specially tailored to study proline dependent folding.

4

SINGLE-MOLECULE MECHANICAL MEASUREMENTS

4.1 FORCES IN BIOLOGICAL SYSTEMS

In biological systems force is an omnipresent quantity. At all levels, from single molecules up to whole organisms, forces have to be withstood in order to ensure the structural integrity. Furthermore, mechanical load is actively applied by special biomacromolecules known as molecular motors. These allow for instance an active transport of vesicles or collectively power cell migration or even muscle contraction. Nowadays, we also know that forces have an important regulatory role, for example during embryogenesis. In fact, Engler et al. showed that stem cell differentiation is governed by the mechanical properties of the matrix they are grown on. This was demonstrated by growing stem cells on matrices with different stiffness but identical chemical growth conditions. Stem cells that were cultivated on a stiff substrate (25 to 40 kPa) became osteogenic whereas a low stiffness (0.1 to 1 kPa) caused a neurogenic differentiation [29]. If no appropriate surface for adhesion was present, cells switched to apoptosis. This example demonstrates how forces govern cell development and proliferation. However, there is still not much known about the cellular force-sensing mechanisms at the molecular level. One potential molecular force sensor, domains 20 to 21 of human filamin A, was investigated in this study and the results are presented in Chapter 7.

4.2 HOW TO MEASURE FORCES IN BIOLOGICAL SYSTEMS?

At the cellular level there are different approaches to measure forces exerted during e.g. cell migration. To this end, cells are grown on special surfaces covered with flexible micro pillars or on deformable matrices with embedded particles for motion tracking. If cells move on these surfaces, the pillars or the matrix together with the tracking particles will be displaced according to the elastic properties of the material. This can be used to obtain a rough estimate of the forces exerted by the cell [24].

In order to understand the mechanics on the cellular level, we first have to study the underlying molecular mechanism. There are approaches to accessing forces inside cells by using artificial force probes [37]. These usually consist of a molecule with a defined spring behavior and a FRET based readout of the stretching length. By inserting these probes into force-bearing structures, e.g. proteins involved

in focal adhesions (the connection points during cell migration), we now get a scalar force estimate from inside the cell. Unfortunately, those assays are still lacking the vectorial information as well as a real molecular resolution, because usually thousands of molecules give a superimposed signal, which moreover includes no directional information.

To get a fundamental molecular understanding how forces affect biomolecules, we need techniques that have a force resolution on the order of pN, and a directional control to investigate the force response of single biomolecules in specific directions. Finally, this has to be done in aqueous high salt conditions around room temperature to mimic physiological or at least typical *in vitro* conditions. Such techniques are also necessary to calibrate the previously discussed intra-cellular force sensors.

These requirements are fulfilled by mechanical single-molecule experiments such as optical or magnetic tweezers and atomic force microscopy (AFM), which can measure and apply forces to biomolecules, one molecule at a time along specific reaction coordinates. This allows us to study the load-dependent dynamics of structural conformations of proteins and nucleic acids or molecular interactions. Furthermore, single-molecule experiments can resolve rare events, which are averaged out in bulk experiments. Complex rate networks become also accessible because state transitions of a single molecule can be followed over hours in great detail [108, 92].

Bertz et al. studied the mechanical stability of the titin-telethonin complex and compared the native pulling direction with a non-physiological force orientation [7].

AFM is a powerful technique to apply the high forces (>15 pN up to several nN) necessary for unfolding or dissociating stable proteins and protein complexes. Because of the high spring constant of the cantilever (6 to 100 $\mathrm{pN\,nm^{-1}}$), AFM provides a fast response that is well-suited to observe transient short-lived unfolding intermediates. Refolding rates can be measured and quantified indirectly using double jump force experiments. Magnetic tweezers have the advantage that a very high force range can be covered by applying a homogenous magnetic field to a paramagnetic bead. This is ideal for constant force experiments. The magnetic field can also be turned, thus turning the bead, which is for example used to study the torque dependent coiling of DNA [21]. On the downside, magnetic tweezers have less spatial and time resolution compared to optical traps, which are ideally suited for the low-to-intermediate force regime (0.5 to 65 pN) and can reach sub nm resolution on a sub ms timescale. Because both investigated filamin domains unfold at forces lower than 35 pN and, as it turned out, most of the results depend on forces below 10 pN and in part involve fast kinetics over $1000\,\mathrm{s^{-1}}$, optical tweezers were the method of choice.

4.3 OPTICAL TWEEZERS

Arthur Ashkin and colleagues reported in 1987 the first observation of what is now commonly referred to as an optical tweezer: a tightly focused beam of light capable of holding microscopic dielectric objects stable in three dimensions [4].

Throughout the 1990s and afterwards, researchers like Carlos Bustamante, James Spudich, and Steven Block pioneered the use of optical trap force spectroscopy to characterize molecular-scale biological motors. These molecular motors are ubiquitous in biology, and are responsible for locomotion and mechanical action within the cell. Optical traps allowed the observation of forces and dynamics of these nanoscale force-generating molecules. Meanwhile optical tweezers are also used to study the folding of nucleic acids and proteins [13, 122, 46, 2, 28].

The study presented here uses optical tweezers not only to investigate the complex folding behavior of domains 20-21 of human filamin A, but also to investigate the force-sensing mechanism of the domain pair at low forces between 2 to 6 pN as well as its modulation through a proline switch.

4.3.1 *Working principle of optical tweezers.*

When the size of a microsphere is much larger than the wavelength of the trapping laser, usually $R > 10\lambda$ with R being the radius of the microsphere and λ the wavelength of the laser, the optical forces on the microsphere can be calculated by ray optics [3]. A qualitative view of optical trapping of microspheres in the ray optics regime is shown in Figure 8. The microsphere will be trapped at the focus of the laser beam as shown in Figure 8A (left). If the microsphere moves to the right of the focus (Figure 8A, right), it will deflect the laser beam to the right and thus increase the momentum of photons to the right. The counter force from the deflected photons will push the microsphere to the left, i.e. back to the focus of the laser beam. If the microsphere moves along the propagation direction of the laser beam, it will focus the laser more strongly and thus increase the momentum of photons along the propagation direction. The counter force from the deflected photons will push the microsphere back to the focus of the laser beam. The same thing happens if the microsphere moves away from the focus in other directions. Thus, a focused laser beam forms a stable optical trap in 3D. Actually, the bead is always axially displaced from the focus in the wave propagation direction due to surface reflection of the laser, which is not shown. In fact, the photons reflected back by the surface of a microsphere will push the microsphere forward. If this force is larger than the restoring force due to refraction, the microsphere cannot be trapped. The surface reflection

The ray-path shown in Figure 8A was calculated with a Java applet developed by Di Leonardo.

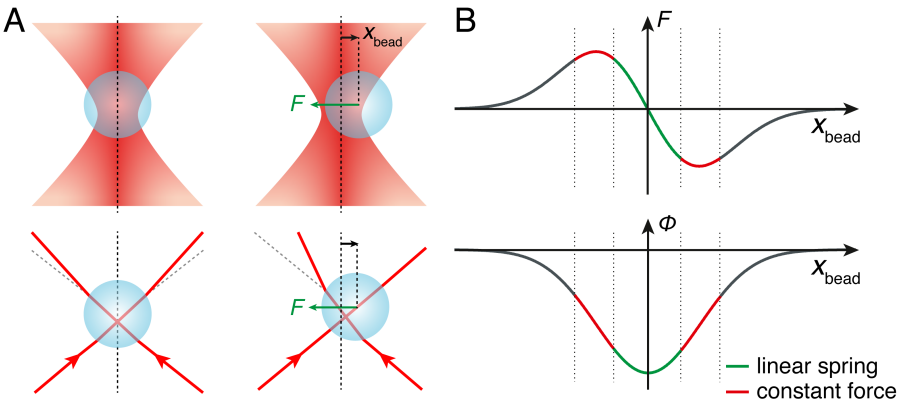

Figure 8: The principle of optical trapping. (A) Schematic representation of a bead trapped in a highly focused laser beam in a relaxed (left) and a deflected (right) position. The upper two diagrams show the intensity gradient of the laser beam, while the lower two depict the path of the outer most rays. (B) Force (upper) exerted on a bead deflected by x_{bead} from the trap center. The lower graph shows the corresponding potential. Green area marks the linear region where the trap is usually operated. For a passive force-clamp mode also the non-linear almost constant red region can be used.

depends on the relative refractive index of the microsphere and the surrounding medium. To increase the restoring force, the laser beam is strongly focused by a high numerical aperture (NA) objective lens. In the setup used for this study the laser light was focussed by an objective with a numerical aperture of 1.45.

The picture gets more complicated for the case $R \ll \lambda$, a condition known as the Rayleigh regime, where light cannot be represented by rays anymore, but trapping still occurs [111]. In this regime, the wave-like properties of light are taken into account and objects can be represented as point dipole scatterers (Rayleigh approximation). Taking into account the finite size of the trapping spot induced by a linearly polarized Gaussian beam, one can use the Rayleigh scattering theory to calculate analytically the optical force acting on the trapped particle [41]. A one-dimensional projection of the position dependent trapping potential Φ and the resulting force $F = -\nabla\Phi$ are shown in Figure 8B (lower and upper, respectively).

In most experiments with optical tweezers, the sizes of the dielectric particles are comparable with the wavelength of the trapping laser ($R \approx \lambda$). In this case, neither ray optics nor the Rayleigh approximation are appropriate. Instead, the electromagnetic theory of light has to be used, complicating theory. For optical trapping of homogeneous and isotropic microspheres, as used in our experiments, one can revert to the generalized Lorenz-Mie theory [109]. This theory was implemented in a computational toolbox by Nieminen et al., which can be used to numerically access optical forces in the intermediate regime [82].

4.3.2 *The setup*

A custom-built optical tweezers setup initially designed by Gebhardt et al. was used for the single-molecule mechanical measurements performed during this study (see Figure 9, for a more detailed description of the setup cf. [33]). It features a dual beam design with back

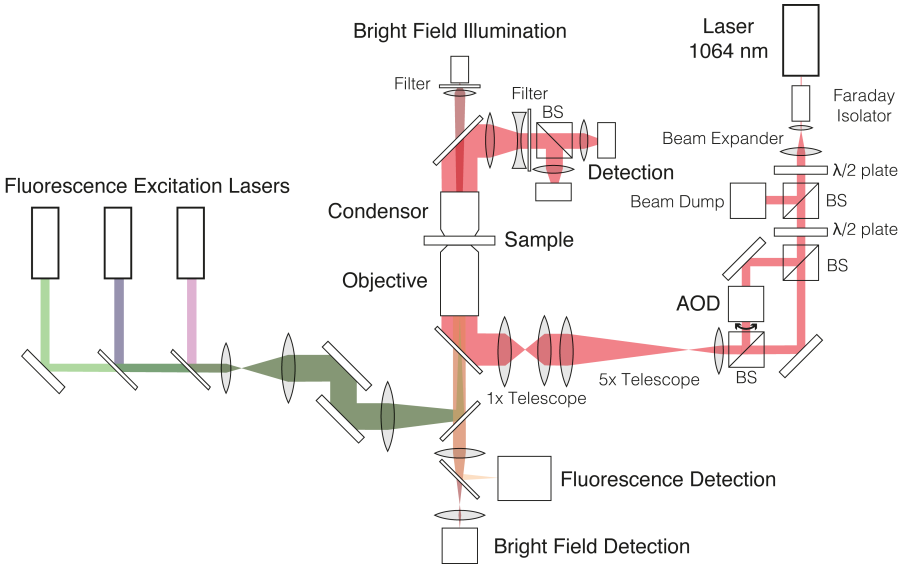

Figure 9: Schematic representation of the optical tweezers setup adapted from [106].

focal plane detection and one AOD-steerable beam. Trapped beads were calibrated with the technique reported by Tolić-Nørrelykke et al. [112]. The trap stiffness could be determined with an error of approximately 10 % and varied between different experiments from 0.25 to 0.30 pN nm^{-1}. Data was acquired at a sampling rate of 100 kHz and averaged to 20 kHz before storage. For data analysis, the difference of both bead signals was calculated after the experiment in order to increase the signal to noise ratio [76]. The signals were corrected for both crosstalk due to depolarization and proximity of the beams. For computational reasons, long passive-mode traces with slow kinetics were analyzed after resampling to 5 kHz.

4.4 THE DUMBBELL ASSAY

The dual beam design of the optical tweezers setup enabled us to use a dumbbell geometry for force application as shown in Figure 10. Therefore, special molecular constructs were created by tethering the protein termini to 180 nm long double-stranded DNA molecules through disulfide bonds. The ends of the DNA were functionalized with biotin and digoxigenin, respectively. This allowed attachment to 1 µm diameter silica beads, which gave the characteristic dumbbell shape

to the stretched bead-DNA-protein-DNA-bead construct [13, 34, 108].

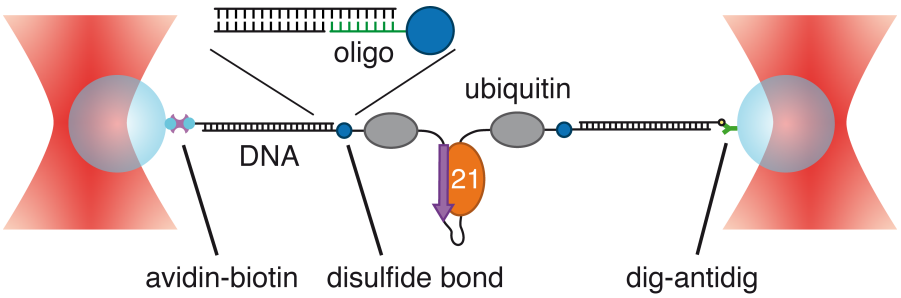

Figure 10: Dumbbell shaped bead-DNA-protein-DNA-bead construct used in dual beam optical tweezer experiments. The DNA is specifically bound to the protein via disulfide bonds and through biotin and digoxygenin to the appropriately functionalyzed beads (see Section B.2).

In more detail, we used the DNA molecules as handles to separate the investigated protein from the bead surface and the trapping lasers. This reduced heating of the protein and prevented undesired surface reactions as well as photochemistry. Another beneficial effect was the protein-independent attachment reaction of the handles to the beads.

Furthermore, all protein constructs were inserted between two ubiquitin domains with terminal cysteines using molecular cloning techniques and expressed in *Escherichia coli*. The ubiquitins serve as spacer-molecules during construct production to prevent direct reaction of the terminal cysteines later used for DNA-handle coupling. Because ubiquitin domains are mechanically much more stable than Ig-like domains [98], they do not unfold at our exerted force range and, thus, do not interfere during the single-molecule mechanical measurements.

For a successful construct formation, one protein had to bind two long double stranded DNA handle molecules. Because attachment of the second DNA molecule was drastically hindered by the electrostatic repulsion of the already bound DNA, we only used short single stranded DNA oligos (shown in green in Figure 10). The oligos were bound to the terminating cysteines of the protein via thiol groups located at the 5′ end of the oligo.

Double stranded DNA molecules were produced by Polymerase Chain Reaction (PCR) on a lambda phage template. The sense primers were triply functionalized with biotin or digoxigenin, while the antisense primers contained an abasic site that caused the polymerase to fall off and left a single stranded overhang. Finally, this overhang was hybridized to the protein-coupled DNA oligos, which resulted in the complete DNA-protein-DNA construct.

The choice of the bead size was a trade-off between good experimental handling, high visibility in the bright field of the setup and good trapping behavior as well as low hydrodynamic drag. As bead

material we chose silica over polystyrene because of the distinct advantage of reduced sample heating [86] and lowered damage to the sample due to the creation of free oxygen radicals [66]. This resulted in choosing silica beads with a diameter of 1 µm.

4.5 MEASUREMENT PROTOCOLS

Throughout the whole investigation mainly three types of protocols were used: constant velocity, passive mode and jump experiments. A newly developed mechanical single-molecule competition assay and protein specific variations of these standard protocols will be discussed in corresponding sections (Section 6.2 and Section 5.8, respectively).

4.5.1 *Constant-velocity experiments*

Constant-velocity experiments are useful for quickly assessing the general force scales for folding and unfolding. In a typical constant-velocity experiment as shown in Figure 11, the mobile trap is retracted from the fixed one with a constant velocity ranging from typically 10 to 500 nm/s. The force generated along the pulling direction stretches the DNA and destabilizes the protein until one domain unfolds, which causes a length increase of the stretched construct and a decrease of the applied force due to bead relaxation in the trapping potentials. From the length increase, the number of amino acids involved in the unfolding transition can be obtained with high precision. Usually the trap centers are approached again and, depending

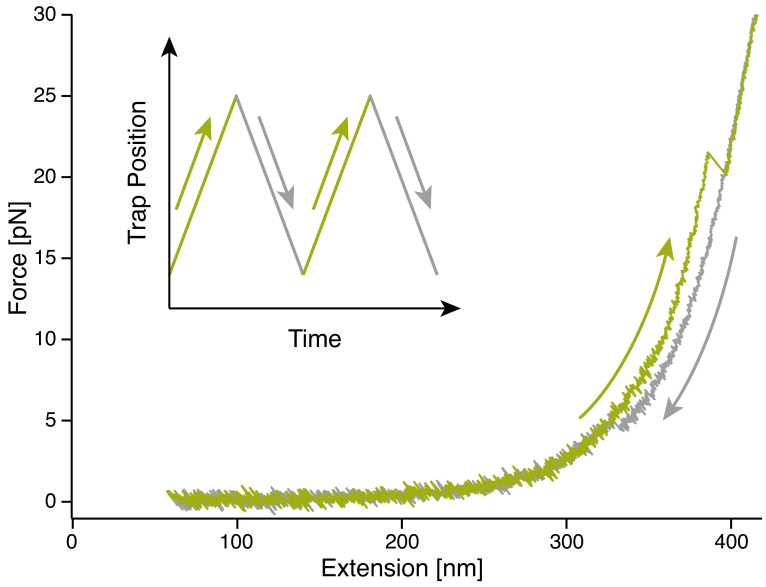

Figure 11: Example trace of a constant-velocity experiment.

on the studied protein, a refolding against force can be observed. This

stretch-and-relax cycle is then repeated many times. The unfolding forces are distributed depending on the unfolding rate constant and the position of the transition state (k_u and Δx in Figure 14) . This information can be obtained by analyzing the pulling speed dependence of the peak of these unfolding force distributions. Various models have been suggested to extract energy landscape information from these data [30, 25, 99].

4.5.2 *Passive-mode experiments*

In our passive-mode experiments the two trap centers are held at a constant separation, thus applying a quasi constant force bias to the dumbbell. Due to the length change caused by unfolding or folding of the investigated protein and the coupled bead relaxation in the non-linear trap potentials, this force bias will be higher for the folded than for the unfolded protein. A theoretically more direct approach is a constant force experiment, where a feedback loop maintains a constant force over time. Because of the response time of this active force stabilization (>1 ms), the force cannot be held constant during the ms timescale occurring in folding/unfolding transitions. Hence, in optical tweezers experiments, it is more advantageous to use a passive-mode approach. An alternative to our passive mode is a passive force clamp mode where one of the beads is held in a flat region of the trapping potential (see red areas in Figure 8) and thus the force does not change with extension of the molecule [39]. For the passive mode used in this study, both beads were positioned in the linear regime of the trapping potential (green area in Figure 8). This gives the best force and time resolution due to a higher effective trap stiffness compared to the passive force clamp mode. In Figure 12 the time trace of a typical passive-mode experiment at three biasing forces is shown. At forces where both the folded and unfolded states are populated, protein folding and unfolding transitions occur, which manifest as abrupt length changes or 'hopping' between two or more states. In the case shown here, we have a two-state folding where the upper (orange colored) state belongs to the folded protein and the lower (grey) state to the unfolded. With increasing force bias (from low to high), the population probability is shifted from predominantly folded to more unfolded. The extracted population probabilities and dwell time distributions of the levels are used to calculate equilibrium free energies and force-dependent microscopic kinetic rate constants. Hidden Markov models (HMM, for details see Section 5.3) and pair-correlation analysis [44] can be used for quantitative analysis. To extract kinetic and equilibrium parameters approaching zero force, all elastic contributions from the trap spring constants as well as the DNA and protein spacers have to be considered (for details see Section 5.6).

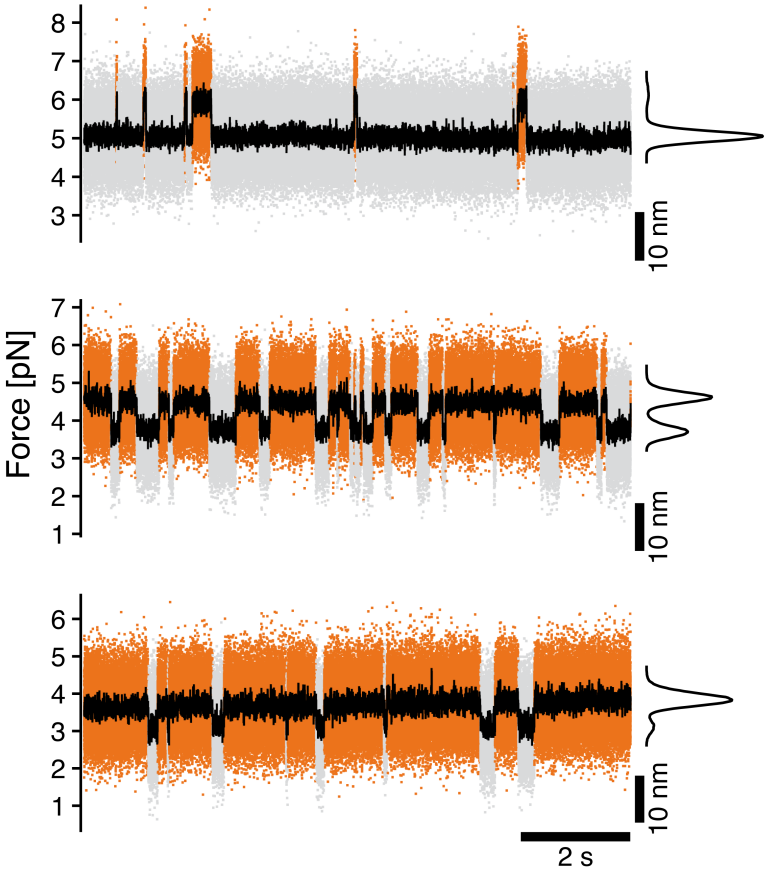

Figure 12: Three sample traces of a passive-mode experiment showing the load dependence of the probability to find a molecule in the folded (orange) of unfolded (grey) state. The black traces are moving-average filtered with a time window of 2.6 ms. The histograms on the right were calculated from the filtered data.

4.5.3 *Jump experiments*

Not for all proteins a passive-mode approach is suitable. In many cases the folding and unfolding rates are too slow to gather significant statistics in the time range of the experiment. A jump protocol can be used in these cases to speed up the kinetics, in that the protein is cycled between two force biases [18, 104, 40, 52]. At higher forces the unfolding will be accelerated while lower forces promote the folding as shown in Figure 13. In contrast to the equilibrium approach, now, only one folding direction can be observed per jump level (unfolding for a high force bias and folding for a low biasing force). The other direction will be drastically slowed down and therefore unmeasurable. From the folded dwell times at high force bias (green, τ_{NU}), the unfolding rate is determined by fitting a single exponential to the accumulated dwell time histograms while the unfolded dwell times at low biasing force (orange, τ_{UN}) give the folding rate. The grey part of the trace is not used for the unfolding/folding analysis. The fold-

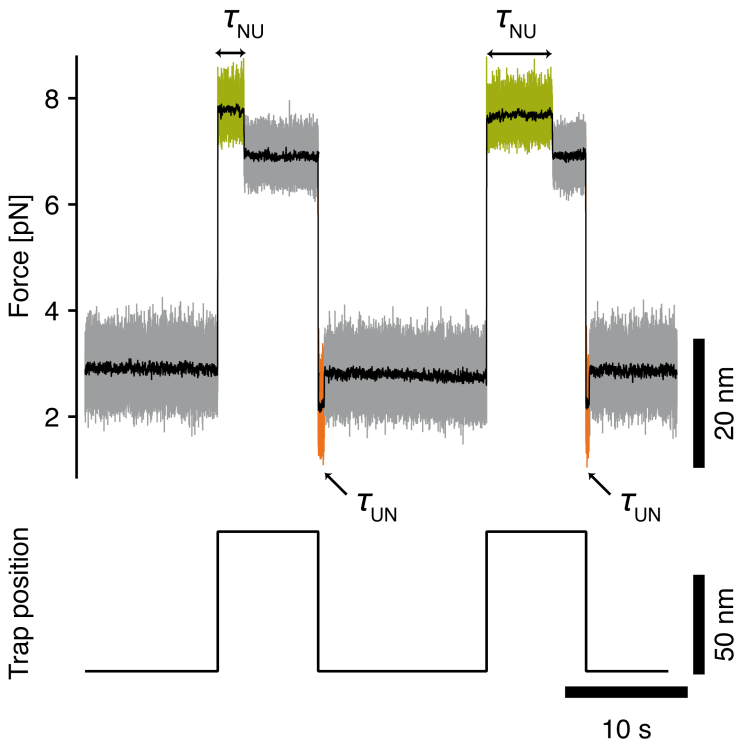

Figure 13: Sample trace of a jump-mode experiment.

ing process can be described as a diffusion process in a potential [8]. In the over-damped case, the fate of the transition is independent of what happened before, resulting in a memoryless process known as a Markov process. Therefore, the jump dwells can also be shorter than a typical dwell time. In case of the high force bias, the folded dwell times are summed up until the first unfolding takes place and vice versa for the lower force bias.

5 THEORY AND DATA ANALYSIS

5.1 POLYMER MODELS

During constant-velocity experiments (Section 4.5.1) force vs. extension curves were recorded as shown in Figure 11. The curve shape can be reproduced with a model describing the elasticity of a DNA-protein-chain. For the low force regime, where the protein is still folded and all tethered ligands bound, we model the DNA handle elasticity with an extensible worm like chain model (eWLC) [13]. In this model, the force is given by

$$F_{eWLC}(d_{DNA}) = \frac{k_B T}{p_{DNA}} \left(\frac{1}{4\left(1 - \frac{d_{DNA}}{L_{DNA}} - \frac{F}{K}\right)^2} - \frac{1}{4} + \frac{d_{DNA}}{L_{DNA}} - \frac{F}{K} \right) \quad (1)$$

with persistence length p_{DNA}, contour length L_{DNA}, elastic modulus K and extension d_{DNA}. The fit yielded persistence lengths of approximately 20 nm, contour lengths of approximately 360 nm and elastic moduli of approximately 600 pN.

Force induced unfolding of the protein adds a flexible polypeptide chain to the compliance of the DNA-protein construct. We account for this by applying the eWLC describing the DNA with the previously determined parameters in series to a worm like chain model (WLC) [12] for the unfolded protein:

$$F_{WLC}(d_{prot}) = \frac{k_B T}{p_{prot}} \left(\frac{1}{4\left(1 - \frac{d_{prot}}{L_{prot}}\right)^2} - \frac{1}{4} + \frac{d_{prot}}{L_{prot}} \right) \quad (2)$$

with persistence length p_{prot} set to 0.7 nm, contour length L_{prot} and extension d_{prot}.

5.2 CONTOUR LENGTH INCREASES

Unfolding leads to a change in contour length of the stretched polypeptide chain. For all investigated constructs the contour length changes were determined through the contour length difference of the fitted WLC models (see Table 1). The corresponding theoretical values were calculated by subtracting the contour length contribution of the final conformational state from the initial contour length. Contributions of folded parts were measured from the crystal structure of the three domains 19 to 21 of human filamin A (pdbID: 2J3S). The unstructured

amino acid sequence contour length was calculated by multiplying the average contour length per amino acid of 3.65 Å by the number of residues [23].

5.3 HMM

During passive-mode experiments the investigated protein fluctuates between various folding states (see Figure 12). We can extract the dwell times with a Hidden-Markov-Model (HMM) based method established by Stigler and Rief for our optical tweezers data (for details see [107]). We use the HMM analysis to assign each data point of the raw 20 kHz difference signal to one folding states. To this end, the raw data (e.g. grey dots Figure 12) are coarse grained into typically 200 bins and a histogram of the smoothed data (black lines in Figure 12) is calculated in order to identify the initial level positions (maxima of peaks in black histograms on the right in Figure 12). The emission values are initialized with Gaussian representation of the states. Each iteration consistes of one pass of the Forward-Backward-Algorithm followed by a re-estimation of the emission probabilities based on the maximum state-probability of each data point. During the iteration process, the emission probabilities are not constrained to Gaussian shapes any more. Iterations are repeated until only negligible numbers of data points (typically less than 0.1%) are reclassified in each step. Afterwards, we compute the lifetime distributions for all assigned states and compare them to fitted single exponentials, which can be used as a measure for the performance of the dwell time assignment. The transition probability matrix is adjusted manually to yield optimal lifetime distributions.

5.4 TRANSITION RATES

After collecting state dwell times, off-rates were obtained from single exponentials fitted to the lifetime distributions of each state. Because all investigated systems could be kinetically separated into two-state systems, this directly gave the transition rates. The single exponential fits were applied to normalized integrated lifetimes and took into account that events shorter than a dead time τ_{min} or longer than τ_{max} could not be observed:

$$p(t) = \frac{\exp(-k_{off} \cdot t) - \exp(-k_{off} \cdot \tau_{min})}{\exp(-k_{off} \cdot \tau_{max}) - \exp(-k_{off} \cdot \tau_{min})} \tag{3}$$

with τ_{max} set to the trajectory's length while τ_{min} depended on the applied force bias and ranged between 200 and 800 µs. Transition rate

errors were estimated by the jackknife method [98, 121]. The jackknife estimate of the standard error of the mean (jSEM) is given by

$$\mathrm{jSEM} = \sqrt{\frac{N-1}{N}\sum_{i=1}^{N}(x_{Ji} - \bar{x})^2} \tag{4}$$

with N being the sample size, $x_{Ji} = \frac{1}{N-1}\sum_{m\neq i} x_m$ the mean of the resampled data set where the point i was omitted and $\bar{x}$ is the mean of the complete data set.

5.5 FORCE-DEPENDENT PROBABILITIES AND EQUILIBRIUM FREE ENERGIES

State probabilities were calculated directly as the sum of all lifetime histograms for a respective state divided by the trace length. The accuracy of this estimation is limited by the finite measurement time. Therefore, uncertainties were estimated by Monte-Carlo simulations by generation of a trace ensemble based on the measured transition rates and their statistical error. The standard deviation of probabilities obtained from the resulting trace ensemble was assigned as probability error. In the following calculations, the system bead-DNA-protein-DNA-bead has been simplified to the equivalent system bead-DNA-protein with one effective trap stiffness $k = (\frac{1}{k_1} + \frac{1}{k_2})^{-1}$. The effective bead displacement $x(F)$ is then the sum of both bead displacements and the DNA contour length is doubled. In our passive-mode measurements, the trap distances are held constant. Every length change of the protein will be associated with a change in the applied force bias due to bead relaxation in the trap potential. This is accounted for in the following calculations. Based on the linker parameters determined by fitting Equation 1 and Equation 2 to the stretch-and-relax curves, the energy $G_i(F_i)$ stored by the bead-DNA-protein dumbbell at a force F_i with the protein being in state i is given by

$$G_i(F_i) = G_i^0 + G_{\mathrm{bead}}(F_i) + G_{\mathrm{DNA}}(F_i) + G_{\mathrm{protein},i}(F_i) \tag{5}$$

with G_i^0 the free energy of the protein in state i,

$$G_{\mathrm{Bead}}(F_i) = \frac{1}{2}F_i x_i(F_i) \tag{6}$$

the Hookean bead displacement energy,

$$G_{\mathrm{DNA}}(F_i) = \int_0^{d_{\mathrm{DNA}}(F_i)} F_{\mathrm{eWLC}}(d_{\mathrm{DNA}})\,\mathrm{d}\,d_{\mathrm{DNA}} \tag{7}$$

the entropic energy of stretching of dsDNA, and

$$G_{\mathrm{protein},i}(F_i) = \int_0^{d_{\mathrm{prot},i}(F_i)} F_{\mathrm{WLC},i}(d_{\mathrm{prot}})\,\mathrm{d}\,d_{\mathrm{prot}} \tag{8}$$

the entropic energy of stretching of the protein in state i. The bead displacement equals the stretching of protein and DNA

$$x_{bead}(F_i) = d_{DNA,i}(F_i) + d_{prot,i}(F_i). \tag{9}$$

When the system undergoes a transition from an initial state i to final state j, the length of unfolded protein changes leading to a force change from F_i to F_j and the energy difference is then given by

$$\begin{aligned}\Delta G_{ij}(F_i, F_j) &= G_j(F_j) - G_i(F_i) \\ &= \Delta G^0_{ij} + \Delta G_{bead}(F_i, F_j) + \Delta G_{DNA}(F_i, F_j) \\ &\quad + \Delta G_{protein,ij}(F_i, F_j).\end{aligned} \tag{10}$$

Because the probabilities are related to energies according to

$$\frac{P_j(F_j)}{P_i(F_i)} = \exp\left(-\frac{\Delta G_{ij}(F_i, F_j)}{k_B\, T}\right), \tag{11}$$

we can obtain the energy differences of the protein between states i and j by performing a global fit to the probability data with

$$P_i(F) = \frac{1}{1 + \sum_{j\neq i} \exp\left(-\frac{\Delta G^0_{ij} + \Delta G_{DNA}(F,F_j) + \Delta G_{protein,ij}(F,F_j)}{k_B\, T}\right)} \tag{12}$$

and weights equal to the inverse of the errors calculated as described before. The experimental uncertainty of the equilibrium free energy difference ΔG^0_{ij} is dominated by the calibration error of the trap stiffness of about 10 %.

How to actually calculate the energies

For computational reasons, the energies stored in the stretching of protein and DNA given by Equation 7 and Equation 8 are calculated via the inverse functions of Equation 1 ($d_{DNA}(F)$) and Equation 2 ($d_{prot,i}(F)$). For a protein in state i being stretched with a force F_i, this gives

$$G_{protein,i}(F_i) = F_i \cdot d_{prot,i}(F_i) - \int_0^{F_i} d_{prot,i}(F)dF. \tag{13}$$

5.6 ZERO-LOAD EXTRAPOLATION OF RATES

Section 5.4 describes how the force-dependent transition rates are calculated from the passive-mode traces. When plotted against force, we get a Chevron-like plot as shown in Figure 21B. In the following, two models are presented that were used to extrapolate the force-dependent rates to zero load.

5.6.1 *Bell model*

The Bell model was introduced to describe the force-dependent dissociation kinetics of receptor-ligand systems [6]. The model assumes that a one-dimensional energy landscape along the reaction coordinate x is tilted by a potential $-\Delta x \cdot F$ when an external force F is applied (see Figure 14). It also neglects all nonlinear contributions of the linkers used in the dumbbell assay and the unfolded polypeptide and also neglects a possible force dependence of Δx. In this study, the Bell model was used to model the force dependence of *cis/trans* isomerization discussed in Chapter 8. For the *cis/trans* isomerization, all nonlinearities were assumed to be negligible due to the small length change of around 1 Å caused by the isomerization. Furthermore, it was assumed that only in the unfolded polypeptide chain the force can propagate to the prolyl bond. In case of *cis/trans* isomerization, the transition rate constant $k_{ct}^{U}(F)$ is given by

$$k_{ct}^{U}(F) = k_{ct}^{U,0} \cdot \exp\left(\frac{F \cdot \Delta x^{ct}}{k_B T}\right) \tag{14}$$

while for the reverse isomerization $k_{tc}^{U}(F)$ is give by

$$k_{tc}^{U}(F) = k_{tc}^{U,0} \cdot \exp\left(-\frac{F \cdot \Delta x^{tc}}{k_B T}\right), \tag{15}$$

where F is the applied force bias, k_B is the Boltzmann constant and T the absolute temperature. $k_{ct}^{U,0}$ and $k_{tc}^{U,0}$ are the isomerization rates for the unfolded protein at zero load. Finally, the distances from the *cis* and *trans* state to the transition state are given by Δx^{ct} and Δx^{tc}, respectively.

5.6.2 *Berkemeier-Schlierf model*

In principle, the Bell model can also be used to describe folding and unfolding of a protein. In this work, we used a better approach, which was introduced previously by Schlierf et al. for protein folding [99, 34]. During the folding process the protein has to overcome a certain energy barrier when contracting from the initial unfolded state i to the transition state T. This model accounts for the energy differences of the DNA linker and bead displacement between the initial state i and the transition state T

$$k_{ij}(F) = k_i^0 \exp\left(-\frac{\Delta G_{iT}^{\#}(F_i = F, F_T)}{k_B T}\right) \tag{16}$$

with k_i^0 being the folding rate constant at zero load used as a fit parameter.

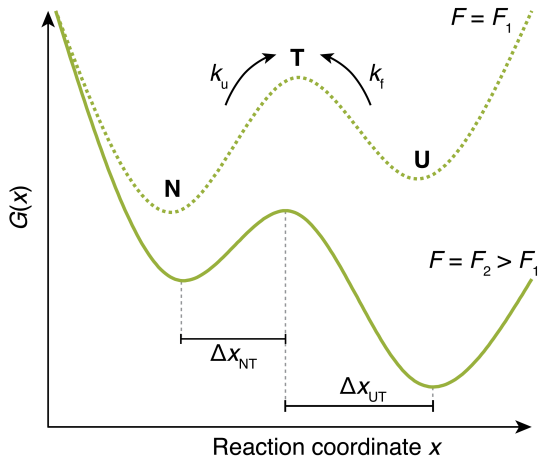

Figure 14: The effect of an external force on an energy landscape. Shown is a hypothetical two-state energy landscape at a low force (dashed line) and at a high force (continuous line). An increasing force leads to a tilted energy landscape, where the basin for the unfolded state U lies lower than the folded state N. This also results in an increased unfolding rate k_u and a decreased folding rate k_f. In case of the Bell model, the distances to the transition state Δx_{UT} and Δx_{NT} are force independent.

The additional activation energy under force

$$\Delta G^{\#}_{iT}(F_i, F_T) = \Delta G_{bead}(F_i, F_T) + \Delta G_{DNA}(F_i, F_T) + \Delta G_{protein,i}(F_i, F_T) \tag{17}$$

consists of the contributions discussed in Section 5.5. F_T denotes the force acting on the construct at the transition state T between initial state i and final state j. The protein length change ΔL_{iT} associated with a transition from i to T defines the transition state distance, measured in contour length, to which the system has to contract before folding over the barrier occurs. With this model, we extrapolated the binding of all tethered-peptide constructs and the folding of FLNa20 (Figure 21 and Figure 37B, respectively).

Due to the non-linear entropic elasticity of the construct contributing to the contraction energy necessary to reach the transition state, the extrapolated folding/binding rate exhibits a curved shape (e.g. Figure 21). Because we measure during passive-mode experiments under equilibrium conditions, the binding/unbinding or folding/unfolding rates must follow the principle of detailed balance and are connected via the equilibrium free energy ΔG. For two equilibrium states i and j, we can write

$$\frac{\Delta G^0_{ij}}{k_B T} = \ln\left(\frac{k^0_i}{k^0_j}\right). \tag{18}$$

Because ΔG^0_{ij} is constant, a curved extrapolation to k^0_i implicates an inversely curved extrapolation k^0_j, as shown in Figure 21. Therefore,

we can calculate the unbinding/unfolding rate extrapolation starting from the fitted binding/folding extrapolation.

Nevertheless, we chose to independently fit Equation 16 to the unbinding/unfolding data with k_i^0 being the unfolding/unbinding rate constant at zero load. The protein length change ΔL_{jT} associated with the transition from j to T defines the transition state distance, measured in contour length, to which the system has to extend before unfolding over the barrier occurs. With this model, we could extrapolate the folding and unfolding rates of the tethered-peptide constructs (Figure 21 and Table 2) and FLNa20 (Figure 37B and Table 4) to zero-load over a force range of 6 pN.

For the tethered-peptide constructs, we performed several test for the applicability of this model. Notably, the equilibrium free energies derived from the extrapolated zero-force rates by Equation 18 lie close to the measured ΔG^0 values obtained from equilibrium populations of states (Table 2). Another test for consistency is the fact that the contour length increases to the transition state, $\Delta L_{open,T}$ and $\Delta L_{closed,T}$, add up to the total contour length change ΔL (Table 1 and Table 2). Finally, as an independet experimental verification, we also compared directly measured unbinding rates of peptides in solution with the corresponding tethered peptides in Chapter 6 and observed an excellent agreement.

5.7 THE LANGMUIR BINDING MODEL

In Chapter 9, we will investigate the enzyme dependent isomerization of FLNa20. Because we are studying single molecules the classic ensemble approach of Michaelis-Menten can not be used to describe the catalytic action of the enzyme. In our case, we are observing one single substrate molecule and titrate the enzyme concentration. Therefore the catalytic effect will be governed by the binding process.

In the framework of a Langmuir binding model the probability of a receptor R to bind a ligand L can be expressed in dependence of the concentration [L] and the dissociation constant K_D. The binding reaction of interest is characterized by the stoichiometric equation

$$L + R \rightleftharpoons LR. \tag{19}$$

This reaction is described by a dissociation constant and the law of mass action as

$$K_D = \frac{[L][R]}{[LR]}. \tag{20}$$

Because our interest lies in the probability that the receptor will be occupied by a ligand, we can write P_{bound} in terms of the concentration of free receptor and receptor-ligand complexes as

$$P_{bound} = \frac{[LR]}{[R] + [LR]}. \tag{21}$$

This amounts to the statement that we can use the fraction of receptors that are bound by ligands as a surrogate for the probability that a single receptor will be occupied by a ligand. Together with Equation 20 we can write Equation 21 as

$$P_{bound} = \frac{\frac{[L]}{K_D}}{1 + \frac{[L]}{K_D}} \tag{22}$$

and with $P_{unbound} = 1 - P_{bound}$ we finally get

$$P_{unbound} = \frac{1}{1 + \frac{[L]}{K_D}}. \tag{23}$$

5.8 METHODS FOR PROLINE ISOMERIZATION DEPENDENT FOLDING

In Chapter 8, I present an investigation of the unfolding and folding of FLNa20 depending on the isomerization of a native *cis* proline. In order to access all kinetic and energetic parameters, we used several analysis methods specifically adapted to the isomerization-dependent experiments. The reader might prefer to skip the following sections and come back to them later when reading the corresponding Chapter 8.

5.8.1 *Cis-trans separation of passive-mode traces*

Passive-mode traces, as shown in Figure 36 and Figure 38, were analyzed after the experiment according to the workflow depicted in Figure 15. First, the native and unfolded states were detected with a HMM based analysis (see Section 5.3).

In Figure 36 a deflection vs. dwell time scatter plot is shown. The folded dwell times (upper, blue and orange circles) clearly separate from the unfolded dwell times (lower, grey circles). While the dwell times of the unfolded state form a horizontally lengthened cluster, the dwell times of the folded states separate into two distinct groups because their dwell times differ by two orders of magnitude. The shorter-lived dwell times can be assign to the native *trans* state (N_{trans}) and the longer-lived ones to the native *cis* state (N_{cis}) by use of a threshold of 0.2 s (dashed vertical line in scatter plot of Figure 15). Because the *cis-trans* isomerization rate is considerably slower (on the

order of minutes) than the unfolding and refolding rate (on the order of seconds), we can use the identified *cis* and *trans* folded dwell times to detect isomerization events.

Starting from the beginning of a passive-mode trace, we sum up all unfolding and folding dwell times until we encounter a different native state dwell time. For example, starting with long-living folded dwell times in *cis*, we add up all dwell times until we detect a short-lived *trans* native state dwell time which signals that the system has switched to *trans*. Next, we sum up the unfolding and folding lifetimes for the current *trans* state until we again reach a long-lived *cis* native state lifetime and so on. Because our measurement is in thermodynamic equilibrium, we can separate the *cis* from the *trans* dwell times leading to two distinct passive-mode traces, one showing unfolding and folding for the *cis* state and the other for the *trans* state. From these traces, we extract the force-dependent unfolding and folding rates and folding probabilities shown in Figure 37B by following our standard method. This determines the horizontal transitions of the kinetic model in Figure 37A.

The vertical isomerization transitions can be addressed by analyzing the *cis* and *trans* dwell times. It is important to note that we don't distinguish between the isomerization path via the native or unfolded state. Instead, we measure effective isomerization rates (k_{ct}^{app} and k_{tc}^{app}, see Figure 40), which are a linear combination of the folded and unfolded path weighted with the probability to be in the native or unfolded state (Equation 28 and Equation 29). The force-dependent probabilities are determined from the *cis* and *trans* only traces generated as described above. Similar to the unfolding and folding rates, the effective isomerization rates k_{ct}^{app} and k_{tc}^{app} are determined by fitting a single exponential to the cumulative histogram of all collected *cis* and *trans* dwell times. In order to extract the microscopic isomerization rates k_{ct}^{N}, k_{tc}^{N}, k_{ct}^{U} and k_{tc}^{U}, Equation 28 and Equation 29 are fitted to the k_{ct}^{app} and k_{tc}^{app} data, respectively. The extracted fit parameters are shown in Table 5. For computational reasons, the extremely long passive-mode traces were resampled from 20 to 5 kHz before dwell time analysis. Only for the fast $N_{trans} \rightleftharpoons U_{trans}$ transitions, where full time resolution is required, 20 kHz data was used.

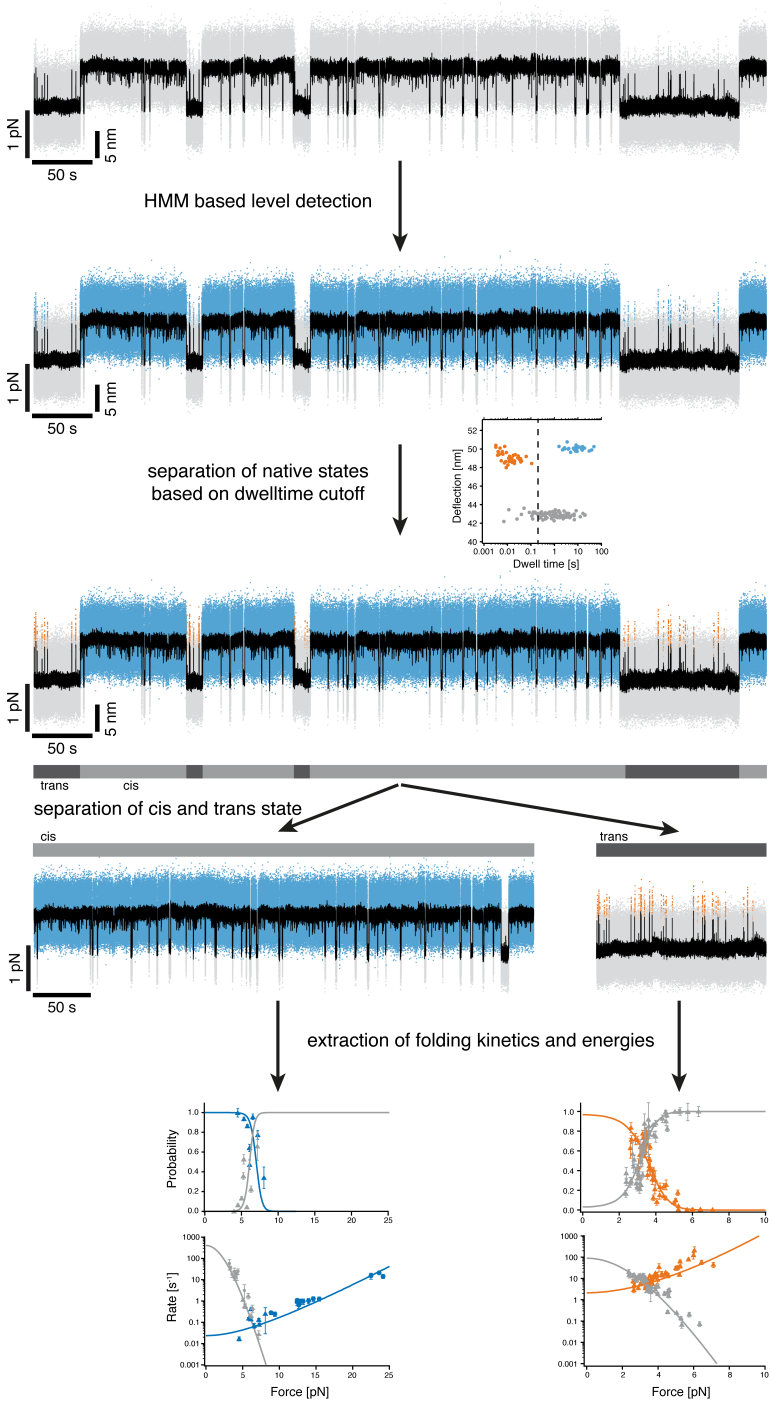

Figure 15: Workflow for passive-mode trace analysis.

5.8.2 *Jump experiments for isomerization dependent experiments*

As already mentioned in Section 5.8.2, a jump protocol can be useful to gather statistics in systems with slow kinetics. In order to extend the accessible force range in the isomerization dependent experiments presented in Chapter 8, we used the following jump protocol

shown in Figure 16. Starting in the native *cis* state, the trap separation

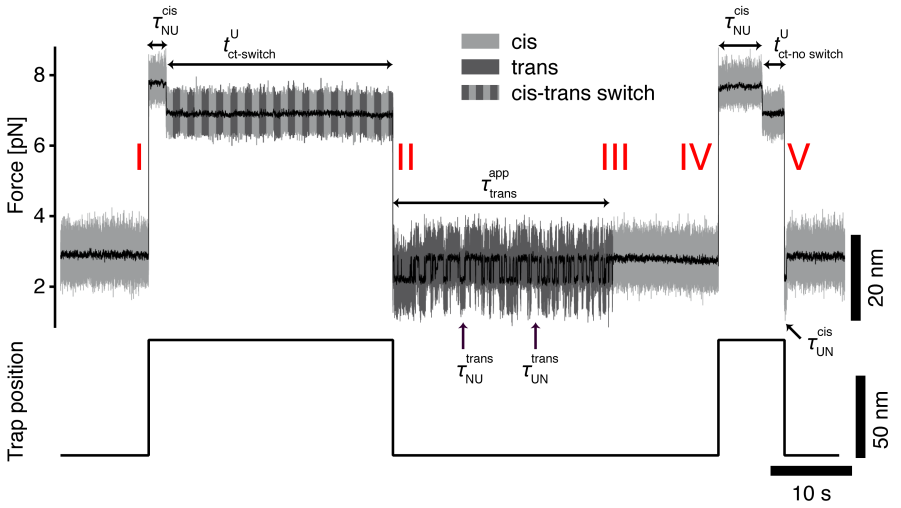

Figure 16: Principles of jump experiments used in Chapter 8. The upper trace shows a force vs. time plot as used for passive-mode measurements and accordingly the same color-code is used as in Figure 4. Because the exact moment of isomerization is not known during the unfolded waiting time $t^{U}_{ct\text{-}switch}$, alternating dark and light grey stripes are used. The black trace was moving-average filtered with 4.2 ms time window. The lower trace shows the trap position over time. Jumps and the *trans-cis* isomerization event are marked by red Roman numerals.

is increased instantaneously (less than 10 µs, see red I in Figure 16) and a force bias between 15 and 25 pN is applied to the folded domain. The time until unfolding is assigned as a native *cis* unfolding dwell time τ^{cis}_{NU} and is used to extend the range of measurable unfolding rate k^{cis}_{NU} (see circles in Figure 37B. After a fixed period the protein is relaxed to a low force around 4 pN where the isomerization state can be detected (see II in Figure 16). Depending on whether the proline switches to the *trans* isoform, the protein can show two distinct behaviors. A single step folding means the prolyl bond is still in the *cis* state while a series of unfolding and folding events indicates a previous switch to the *trans* state. According to the isomerization state, the previous high force waiting time is counted as $t^{U}_{ct\text{-}switch}$ or $t^{U}_{ct\text{-no switch}}$. In the next section, it is explained how these times can be used to determine the *cis-trans* isomerization rate $k^{U}_{ct}(F)$. In case the *cis-trans* isomerization has occured, the protein will rapidly fluctuate between the unfolded and native states (U_{trans} and N_{trans}), and the measured dwell times τ^{trans}_{NU} and τ^{trans}_{UN} are used to determine the *trans* unfolding and folding rates (k^{trans}_{NU} and k^{trans}_{UN}) shown in Fig. 2C. After a while the fluctuation stops because the prolyl bond switches back to the *cis* state which "locks" the protein in N_{cis} , due to the slow *cis* unfolding rate k^{cis}_{NU} and native state isomerization rate k^{N}_{ct} (see III in Figure 16). The time of fluctuation corresponds to the *trans* dwell

times τ^{app}_{trans}, which are used to extract k^{app}_{tc} (see circles in Figure 40B). To "unlock" the protein from N_{cis}, the force bias is again increased (see IV in Figure 16) leading to the unfolding of the protein. After a defined waiting time, the prolyl bond isoform is tested by jumping down (V in Figure 16). In this example, after the second jump down the protein readily refolds and then stays refolded, which means that no isomerization took place during the waiting step at high force. Therefore, the waiting time is counted as $t^{U}_{\text{ct-no switch}}$. From the folding dwell times τ^{cis}_{UN} the *cis* folding rate k^{cis}_{UN} is determined.

5.8.3 *Maximum-likelihood estimation of cis-trans isomerization rate*

During the aforementioned jump experiments, two different types of information are accumulated which enable us to determine the isomerization rates k^{app}_{tc} and $k^{U}_{ct}(F)$. While k^{app}_{tc} can be determined directly by measuring τ^{app}_{trans}, for the *cis-trans* isomerization we can only determine whether an isomerization has occurred during the given waiting time. Fortunately, we can use this information to extract the actual isomerization dwell time for the unfolded domain. Therefore, the waiting time after unfolding is varied and two time series are collected for a successful ($t^{U}_{\text{ct-switch}}$) or no ($t^{U}_{\text{ct-no switch}}$) isomerization. Based on this time series and the knowledge that isomerization follows exponential kinetics, the following likelihood functions are given as

$$\mathcal{L}(k^{U}_{ct} \mid t^{U}_{\text{ct-switch},1}, \ldots, t^{U}_{\text{ct-switch},n}) = \prod_{i=1}^{n} \left(1 - \exp(-k^{U}_{ct} \cdot t^{U}_{\text{ct-switch},i})\right) \quad (24)$$

in case of an isomerization event and

$$\mathcal{L}(k^{U}_{ct} \mid t^{U}_{\text{ct-no switch},1}, \ldots, t^{U}_{\text{ct-no switch},m}) = \prod_{j=1}^{m} \left(1 - \exp(-k^{U}_{ct} \cdot t^{U}_{\text{ct-no switch},j})\right) \quad (25)$$

when no isomerization has occured. To actually compute the maximum-likelihood estimate for k^{U}_{ct}, we calculate the total log-likelihood of the likelihood functions above

$$\ln \mathcal{L}(k^{U}_{ct} \mid t^{U}_{\text{ct-switch},1}, \ldots, t^{U}_{\text{ct-switch},n}, t^{U}_{\text{ct-no switch},1}, \ldots, t^{U}_{\text{ct-no switch},m}) = \sum_{i=1}^{n} \ln\left(1 - \exp(-k^{U}_{ct} \cdot t^{U}_{\text{ct-switch},i})\right) + \sum_{j=1}^{m} \ln\left(1 - \exp(-k^{U}_{ct} \cdot t^{U}_{\text{ct-no switch},j})\right). \quad (26)$$

Now, we can plot the log-likelihood function and estimate k^{U}_{ct} by finding the maximum. Figure 17 shows an exemplary log-likelihood graph where k^{U}_{ct} was estimated to $0.173\,s^{-1}$ for a force of 11.2 pN.

This method gives us the possibility to directly measure the force dependence of $k_{ct}^{U}(F)$ and to extend the accessible force range of k_{ct}^{app} shown in Figure 40A (circles) beyond the region of passive-mode experiments (triangles).

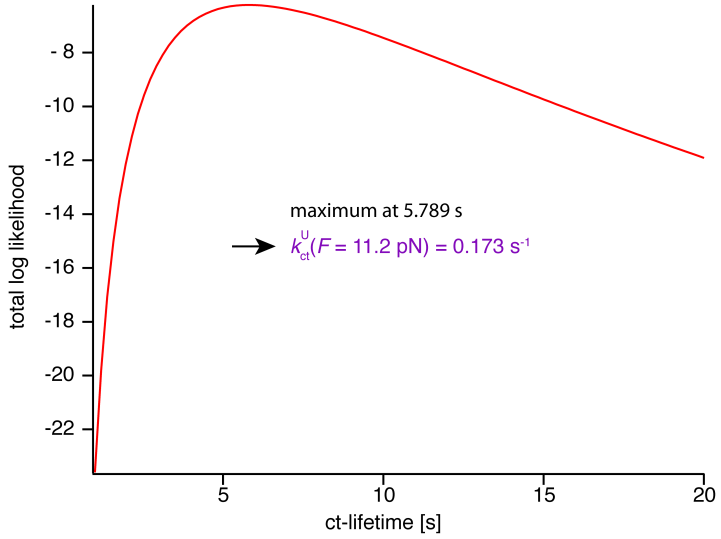

Figure 17: Total log-likelihood calculated from Equation 26 for a sample of waiting times measured at a force of 11.2 pN during jump experiments. Maximization gives an estimate for the unfolded *cis-trans* rate of $k_{ct}^{U}(11.2\,pN) = 0.173\,s^{-1}$.

5.8.4 *Multiple sequence alignment*

Protein sequences were obtained from corresponding PDB files and domain borders were estimated by visual inspection. In three cases i. e. domains 17 and 19 of FLNa and domain 20 of FLNb, there are two structures for the same domain. They could be omitted in the sequence alignment without any effect. For the sake of completeness, however, we included all 39 domains in the final multiple sequence alignment, which was performed using ClustalW within BioEdit [18, 40]. The result is shown in Figure 18.

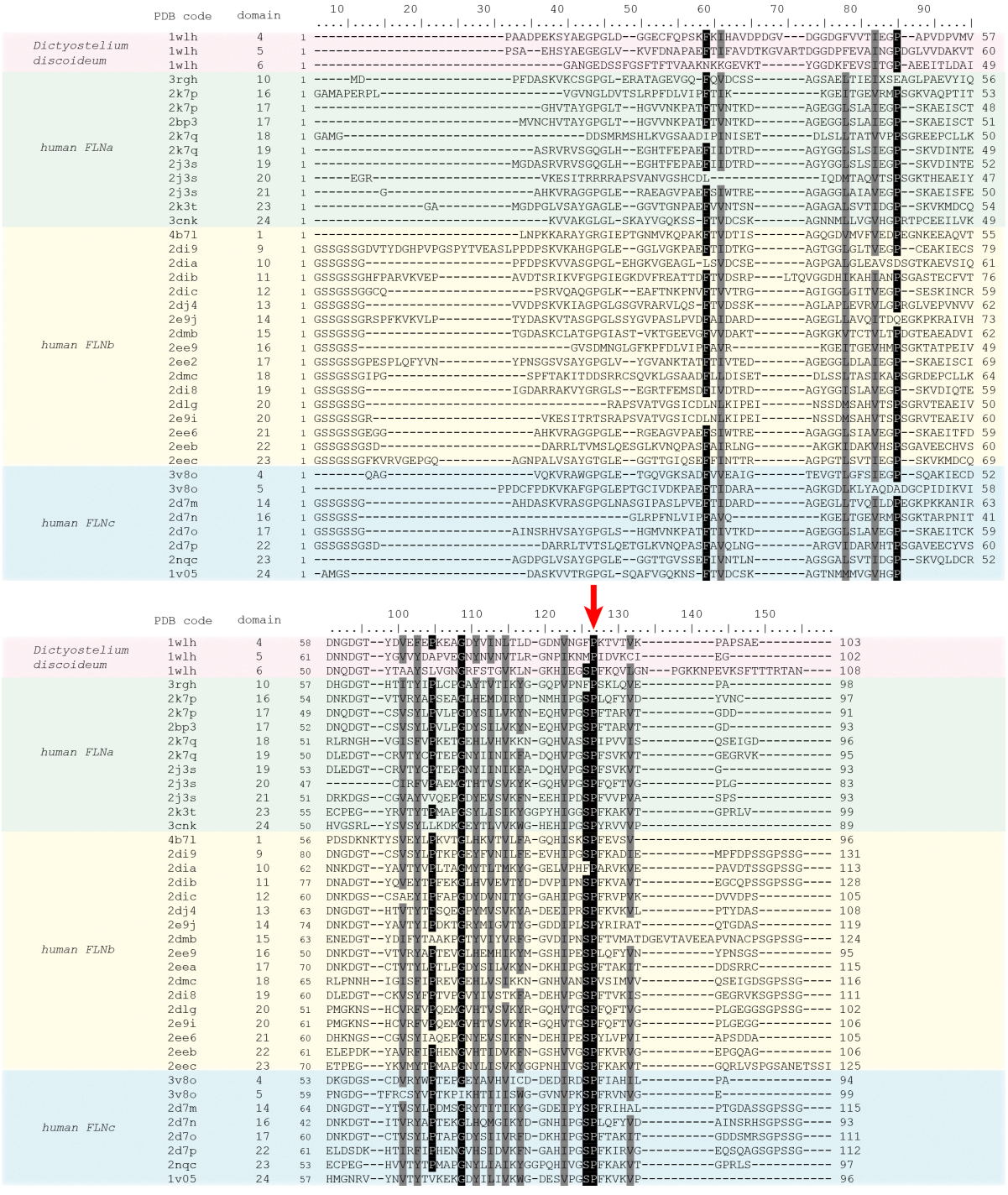

Figure 18: Shown is a multiple sequence alignment of available filamin domains using ClustalW [40, 18]. The highly conserved proline is marked with a red arrow.

Part III

RESULTS

In the third part of this thesis, I present the experimental results of my four research projects followed by an individual discussion for each chapter.

6

LIGAND BINDING TO FILAMINS MULTIRECEPTOR BINDING SITE

The main goal of this work was the characterization of the hypothesized autoinhibition mechanism of the filamin domain pair 20-21. Before investigating the domain-domain interaction and its effect on ligand binding, I first wanted to characterize the uninhibited binding site. The results of the corresponding experiments as well as the therefore developed mechanical competition assay are presented in the following chapter.

6.1 INTERACTION WITH TETHERED TARGET PEPTIDES

In a first set of experiments, the uninhibited mechanical binding strength of domain 21 to different interaction partners was studied. The investigated binding partners were the C-terminal peptide of GPIb's α-chain (GPIbα), the integrin β7 cytoplasmic tail peptide (ITβ7) as well as the filamin-interacting peptide of the integrin regulator migfilin (Mig) [50, 20]. In order to measure the interaction in our dumbbell assay, the respective interacting peptides were directly fused to the N-terminus of an isolated domain 21 of filamin (FLNa21) with a 6 amino acid residues spacer allowing the necessary flexibility. The resulting experimental geometry where the force is applied between the N-terminus of the binding peptide and the C-terminus of FLNa21 is shown in Figure 19. For details about the creation of these fusion constructs please refer to Section B.1. Upon stretching the DNA-protein

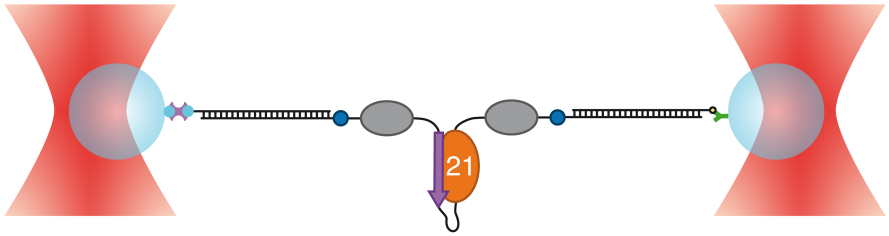

Figure 19: The mechanical binding strength of different interaction partners with the multireceptor binding site of FLNa21 was assayed with special fusion constructs. In these constructs the studied binding regions were directly tethered to FLNa21 via a flexible peptide linker. Specific attachment to functionalized silica beads via DNA handles resulted in the characteristic dumbbell geometry used in our dual beam optical tweezers.

construct in constant-velocity experiments, the force rises steeply beyond extensions of 320 nm, when the DNA is almost fully elongated

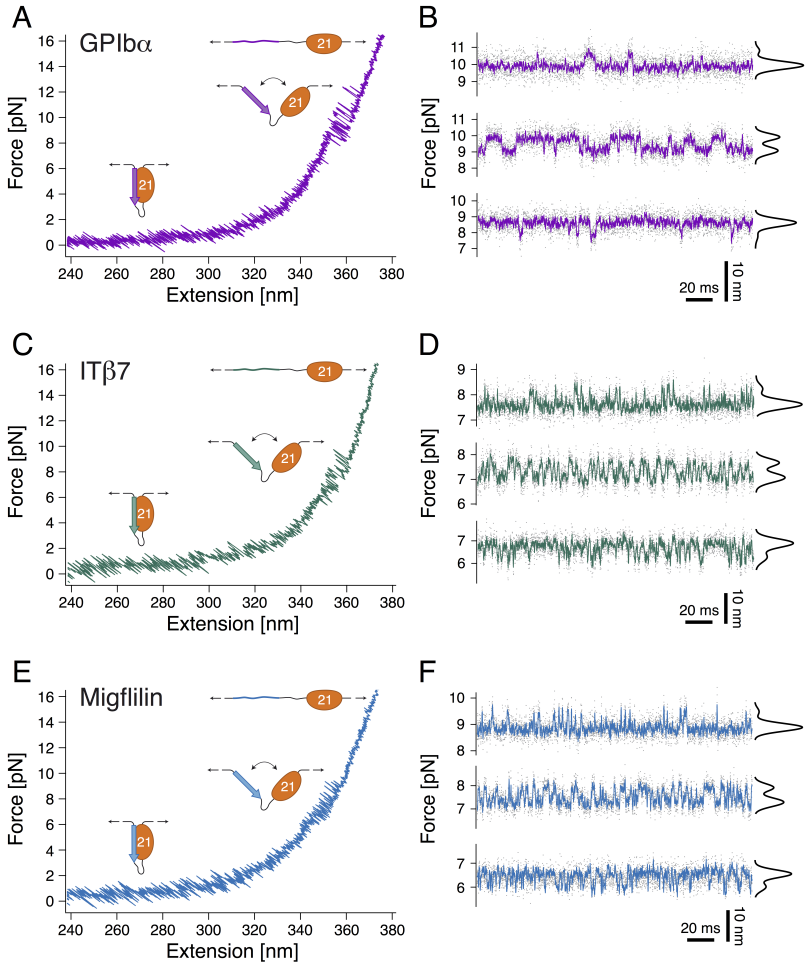

Figure 20: Interaction of filamin with tethered peptides in constant-velocity (left) and passive-mode (right) experiments.

(Figure 20A). At forces between 7 and 12 pN, rapid near-equilibrium fluctuations of binding and unbinding of the GPIbα peptide can be observed. The contour length gain during this transition ($\Delta L = 12.5 \pm 0.5$ nm) is in excellent agreement with the expected length gain if the 26 amino acid residues of the bound peptide detach and are fully stretched (see Table 1). To obtain a precise analysis of the force-dependent binding/unbinding kinetics of the peptide, we performed passive-mode measurements, hence imposing a constant average force-bias on the fluctuating molecule. Because only the separation of the trapping potentials is held constant, the force varies between the closed and open conformation. Here we define force-bias as the mean of the force acting on the closed/bound and open/unbound state. This allowed us to observe fluctuations between bound (high force) and unbound (low force) states for several minutes at different biasing forces (Figure 20B). At low forces, the molecule dwells predominantly in the bound state with few rapid excursions into the unbound state (Figure 20B, lower trace). With increasing force, the equilibrium (black

population distributions in Figure 20B) shifts to the unbound state together with altered kinetics (upper two traces of Figure 20B). The force-dependent population shift provides a direct measure for the free energy of binding in the absence of load of $10.6\,k_B\,T$ (see Figure 21A and Section 5.5). A dwell time analysis using a Hidden-Markov-Model (HMM, see Section 5.3) yields the force-dependent kinetics of GPIbα binding/unbinding (Figure 21B). Unbinding rates (circles) increase with force, while binding rates (triangles) drop with force. For extrapolation of the binding/unbinding branches to zero-force, we used a model that considers the compliance of the unfolded peptide leading to a curvature in the branches as discribed in Section 5.6.2.

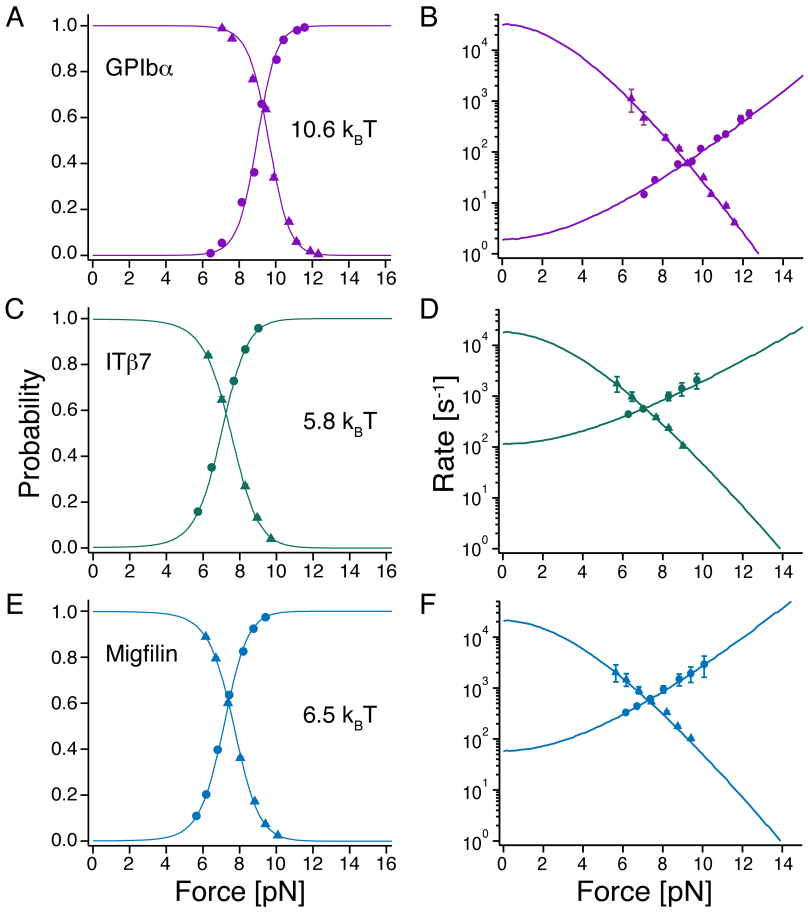

Figure 21: Equilibrium results of FLNa21 interacting with three different tethered peptides. (Left) Force-dependent equilibrium probabilities to be in the bound (triangles) or unbound (circles) state. Solid lines correspond to the globally fitted force-dependent probability as given by Equation 12. (Right) Opening (circles) and closing (triangles) rates as a function of force. The solid line is an extrapolation of the rates to zero load taking into account the compliance of all mechanical elements in the construct (see Section 5.6.2).

CONSTRUCT	ΔL	ΔL_{calc}	$\Delta L_{closed,T} + \Delta L_{open,T}$
	nm	nm	nm
FLNa21-ITβ7	11.6 ± 0.3	11.1	9.7
FLNa21-Mig	12.0 ± 0.5	11.9	10.9
FLNa21-GPIbα	12.0 ± 0.5	11.1	12.3
FLNa20-21 opening	14.5 ± 1.1	16.8	13.7
FLNa20	17.7 ± 0.3	18.0	n.d.
FLNa21	28.8 ± 0.5	29.5	n.d.

Table 1: Contour length increases. ΔL in column 2 is the experimentally determined contour length increase using the WLC model, which was applied to force-extension traces, as well as to constant distance measurements. Errors are given as the standard error of the mean. ΔL_{calc} in column 3 are calculated contour length increases based on the crystal structure (pdbID: 2J3S, see Section 5.2). In column 4, the sum of transition state positions (Table 2, columns 3 and 5) are given as determined by kinetic HMM analysis for constructs where equilibrium measurements were taken. For FLNa20 and FLNa21, no equilibrium measurements were performed and therefore the value is not determined.

The slopes of the binding/unbinding branches reflect the distance of the transition state from the unbound and bound states, respectively. The sum of those distances (12.3 nm, measured in contour length) as obtained from the fits, is very close to the total contour length of the peptide (12.5 nm), which supports the validity of the analysis. The fast binding rate at zero load of $34\,000\,s^{-1}$ reflects the effectively high concentration of the ligand due to tethering. For the unbinding rate, we find $1.9\,s^{-1}$ (see Table 2).

In comparison to GPIbα, the ITβ7 ligand exhibits a significantly lower unbinding force (Figure 20C) as well as free energy of binding ($5.8\,k_B\,T$, see Figure 21C). The major difference in kinetics (Figure 20D and Figure 21D) results from a much faster unbinding rate of $120\,s^{-1}$ at zero load while the binding rates are similar to the ones of GPIbα (see Table 2). Because the unbinding lengths of the tethered ligands and hence the effective concentrations for both peptides are identical, the similar binding rates indicate that rebinding speed is not influenced by details of the sequence. This is further supported by our data of migfilin (Figure 20E, Figure 20F and Figure 21F) that exhibits very similar binding rates. The unbinding rates and the binding free energy of migfilin ($6.5\,k_B\,T$) are in between those of GPIbα and ITβ7 (Figure 21E).

CONSTRUCT	k^0_{bind} $10^3\ s^{-1}$	$\Delta L_{open,T}$ nm	k^0_{unbind} s^{-1}	$\Delta L_{closed,T}$ nm	ΔG^0 $k_B\,T$
FLNa21-ITβ7	19.7 ± 0.9	6.5 ± 0.7	121 ± 9	3.2 ± 0.8	5.8 ± 0.6
FLNa21-Mig	31.2 ± 2.4	6.6 ± 1.1	61 ± 5	4.4 ± 0.7	6.5 ± 0.7
FLNa21-GPIbα	34.2 ± 1.6	7.7 ± 0.6	1.9 ± 0.6	4.5 ± 0.4	10.6 ± 1.1
FLNa20-21	4.9 ± 0.1	7.0 ± 0.6	173 ± 1	6.7 ± 0.3	3.4 ± 0.3

Table 2: Rate fit parameters of tethered-peptide constructs and the double domain construct. The corresponding fits are shown in Figure 21 and Figure 31.

6.2 SINGLE-MOLECULE MECHANICAL COMPETITION ASSAY: LIGANDS IN SOLUTION

In their physiological context, the membrane protein tails are not tethered to the filamin domains. Even though our assay gives valuable information about the unbinding kinetics under load, measuring the free binding and unbinding rates of the ligands requires a different experimental approach. Fluorescent single-molecule methods cannot be used at the high concentrations necessary for observing binding (up to 100 µM) due to the associated high background. We therefore developed a mechanical single-molecule assay that allows direct observation of binding/unbinding events of freely diffusing ligands at those concentrations. To this end, we observed the opening and closing fluctuations of a tethered FLNa21-GPIbα construct in the presence of freely diffusing GPIbα peptide in solution (Figure 22A).

To extract the dwell times of the fluctuating and quenched state, an HMM analysis is applied to appropriately smoothed data (white line in Figure 22), where the fluctuating state is averaged to its mean position whereas the binding/unbinding of solution ligands are still resolved.

Under load, the tethered ligand will constantly fluctuate between bound and unbound states as discussed in Section 6.1. Figure 22A shows a long passive-mode trace with a biasing force of 8.5 pN. In contrast with previous traces without ligands in solution (Figure 20B), we now observe not only the fluctuating state (regions with high standard deviation σ in Figure 22A and left cartoon), but also a mechanically quenched state (Figure 22A, low-σ regions and right cartoon). A zoom into this trace (Figure 22B) shows that in the fluctuating state (left), the construct undergoes rapid opening and closing transitions, while in the quenched state (right) the construct dwells in the open conformation. If the construct is in an open conformation, there will be a competition between the tethered ligand rebinding and a free ligand binding from solution. In the latter case (Figure 22A, right cartoon), rebinding of the tethered ligand will be suppressed and the opening/closing fluctuations vanish until the bound ligand spontaneously dissociates. The dwell times in the fluctuating state ($\tau_{unbound}$) as well as in the quenched state (τ_{bound}) now provide direct information about the binding kinetics of the ligand from solution. While

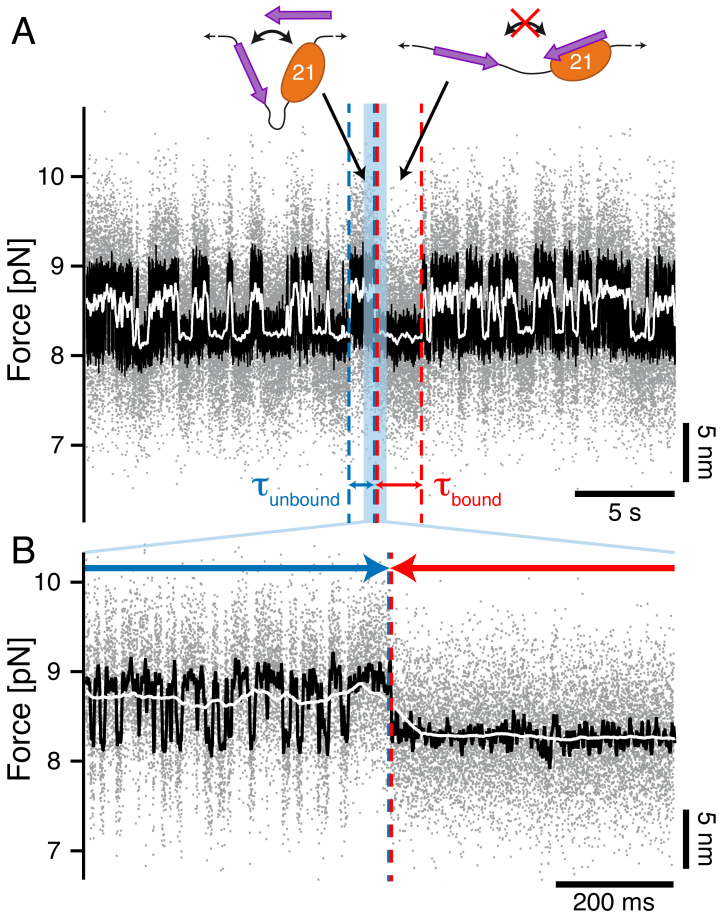

Figure 22: Single-molecule mechanical competition assay to study peptide binding from solution. (A) Passive-mode trace of GPIbα-FLNa21 held at a force bias of 8.5 pN in the presence of 2.3 µM GPIbα peptide in solution. Grey dots represent the 20 kHz raw data and lines represent moving-average filtered data with 2.5 ms (black) and 50 ms (white) time window. (B) A zoom into the blue region shows the transition between a fluctuating and a mechanically blocked state.

$1/\tau_{bound}$ directly yields the off-rate, $1/\tau_{unbound}$ depends on both the solution concentration of the ligand and the applied force:

$$\frac{1}{\tau_{unbound}} = k_{on} \cdot [ligand] \cdot P_{open}(F) \tag{27}$$

where k_{on} is the pseudo first-order on-rate, [ligand] is the concentration of ligand and $P_{open}(F)$ is the previously measured force-dependent probability for the tethered ligand to be in the open conformation (see Figure 21). For GPIbα we measured τ_{bound} and $\tau_{unbound}$ as a function of force and at two different ligand concentrations (Figure 23). As expected, $\tau_{unbound}$ decreases with force, because the probability for finding the tethered construct in an open conformation increases. This is also clearly visible in Figure 24, which shows three sample traces at different biasing forces with zooms (right) into transition re-

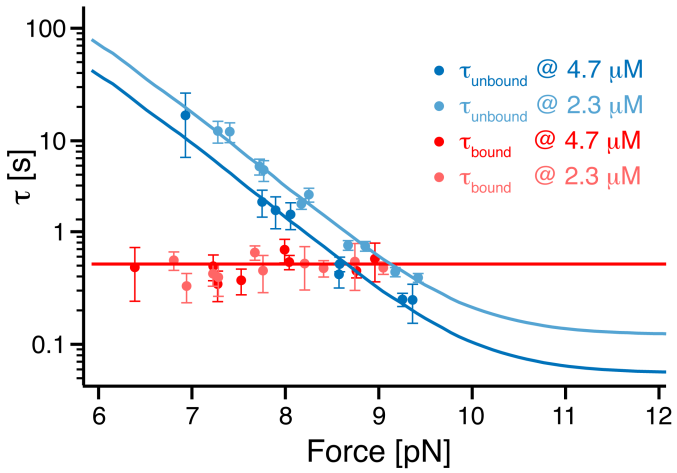

Figure 23: Single-molecule mechanical competition assay to study peptide binding from solution. Dependence of bound and unbound lifetimes as a function of applied force and ligand concentration.

gions between fluctuating and quenched state (blue shaded regions). In addition to its force dependence, $\tau_{unbound}$ decreases with increasing solution concentration (Figure 23). By fitting Equation 27 to the $\tau_{unbound}$-curves we obtain a pseudo first-order on-rate for GPIbα binding of $k_{on} = 3.7\,\mu M^{-1}\,s^{-1}$. It is important to note that the shape of the fit curves is pre-determined by $P_{open}(F)$, which is not a fit parameter but measured directly (Figure 21). The off-rate ($1/\tau_{bound}$) is independent of concentration as well as applied force and we find $k_{off} = 1.8\,s^{-1}$. Because of the independence of the ligand concentration, we can conclude that the binding process is governed by a dissociative displacement mechanism.

This competition assay now allows to determine the force-free on- and off-rates for all three different peptides. Figure 25 shows the dwell time vs. force plots of ITβ7 and Mig measured in competition with the corresponding tethered peptide. As for GPIbα, we find a force and concentration dependent $\tau_{unbound}$ and a constant τ_{bound}. Please note that we can also use different peptides as tethered probe and solution ligand. An overview of all tested combinations and concentrations and the measured on- and off-rates as well as the resulting K_D is given in Table 3.

6.3 DISCUSSION

Both experimental techniques, the force-loaded tethered-peptide constructs as well as the competing ligands from solution, showed the same hierarchy in binding strength, which is governed by the off-rate. Between GPIbα and ITβ7, it varies by two orders of magnitude. In contrast, the binding rate is almost identical. GPIbα exhibits by far the strongest binding to filamin of all peptides investigated. This

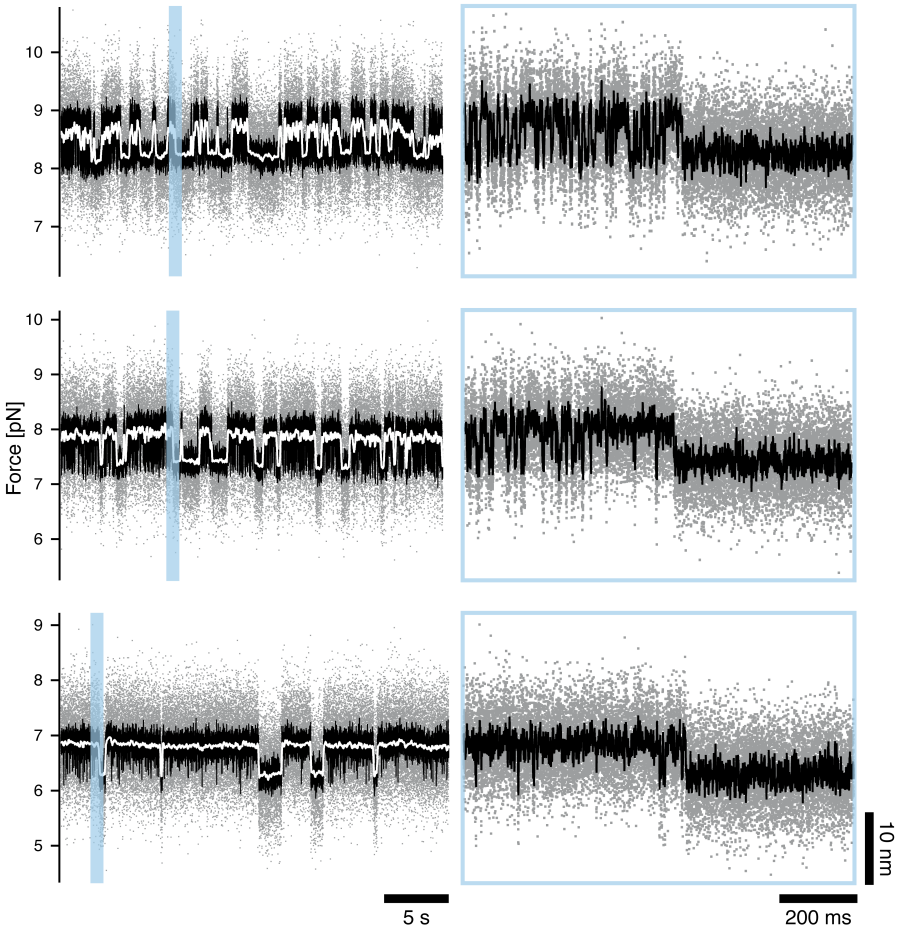

Figure 24: Single-molecule mechanical competition assay at different biasing forces. A zoom into a fluctuation-to-quench switch occurring in the blue shaded area is shown on the right of each trace. By increasing the force bias, the state population equilibrium of the tethered ligand is shifted to the unbound state and the binding site gets more and more exposed leading to an increased number of binding events of the ligand in solution.

finding is particularly important, because platelet integrity critically depends on the mechanical strength of this bond once attached to von Willebrand factor during blood clotting [19]. It has been shown that GPIbα binds von Willebrand factor on the extracellular side with forces similar to those we find for intracellular filamin binding [61]. This could provide a stable mechanism for transmitting force from the extracellular space to the actin cytoskeleton. The higher free energies of binding and interaction forces of migfilin relative to ITβ7 are consistent with migfilin's role in competing off the cytoplasmic tail of β-integrins from filamin during talin-mediated integrin activation [50, 20]. Even though the binding kinetics of the investigated ligands have not been measured before, the equilibrium binding constants (K_D) of the three peptides calculated from the kinetics agree

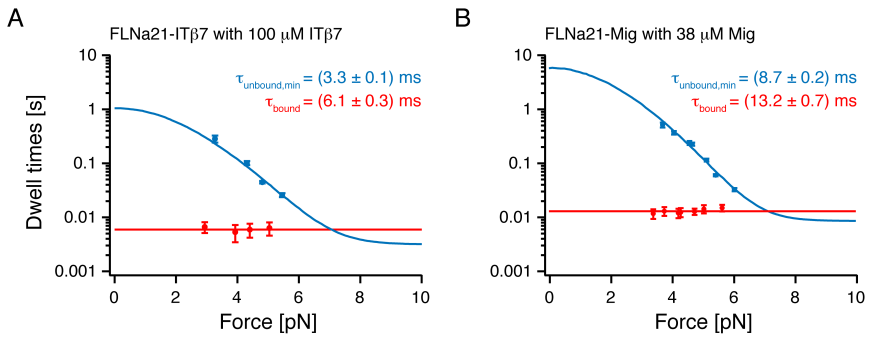

Figure 25: Force-dependent dwell times extracted from the single-molecule mechanical competition assay. Dwell times of fluctuating (blue) and quenched (red) state of different tethered-peptide constructs with corresponding peptides in solution. (A) ITβ7 binding is measured in competition with tethered ITβ7. (B) Migfilin binding is measured in competition with tethered migfilin. The solid lines are fits. For the force independent τ_{bound}, a simple line fit is used. For the force-dependent $\tau_{unbound}$, the fit is given by the inverse of Equation 27. The resulting optimized fit parameters $\tau_{unbound,min}$ and τ_{bound} are shown.

well with bulk measurements (Table 3) [51]. It is interesting to note that with K_Ds in the micromolar range and above, as well as lifetimes below a second, all those interactions are very dynamic. In the cellular context longer lifetimes could be realized by a cooperative action of several binding sites. In fact, for each filamin monomer multireceptor binding sites were reported not only for domain FLNa21, but also for domains 17 and 19. This already gives a total of 6 binding sites per filamin dimer.

With the newly developed single molecule mechanical competition assay, we were able to directly measure zero-load binding kinetics of ligands added into solution. The zero-load off-rates determined with the competition assay for the three ligands are in excellent agreement with the zero-force values that were extrapolated from the tethered-peptide constructs in Figure 21. This is the first direct experimental confirmation of the validity of the extrapolation method used.

The tethered ligand's effective concentration can be estimated from measured on-rates of tethered and non-tethered ligands to be about 10 mM. Compared to ligands added into solution (1–100 μM), this is at least two orders of magnitude higher. At the same time the load applied to the tethered ligand dramatically increases the off-rate. The combination of these two effects results in a much faster binding/unbinding fluctuation compared to the solution ligands (see Figure 22A and Figure 22B). Therefore, the same ligand can be used to probe the binding from solution with enough time resolution to separate between the quenched and the fluctuating states.

CONSTRUCT	PEPTIDE	$c_{peptide}$ µM	k_{on} $\mu M^{-1}\,s^{-1}$	k_{off} s^{-1}	K_D µM
FLNa21-ITβ7	ITβ7	50	3.03 ± 0.21	147 ± 31	48 ± 12
	ITβ7	100	3.06 ± 0.12	163 ± 4	53 ± 6
	Mig	38	3.89 ± 0.26	91.7 ± 14.1	24 ± 5
FLNa21-Mig	Mig	7.6	3.61 ± 0.13	75.2 ± 7.5	21 ± 3
	Mig	38	3.01 ± 0.08	76.0 ± 2.5	25 ± 3
FLNa21-GPIbα	GPIbα	2.3	3.57 ± 0.43	1.93 ± 0.07	0.54 ± 0.09
	GPIbα	4.7	3.83 ± 0.21	1.95 ± 0.15	0.51 ± 0.07

Table 3: Rates of peptide binding from solution measured with the single-molecule mechanical competition assay. The uncertainty of K_D in column 6 was calculated assuming a 10% maximal error for the concentration. All other errors are given as the standard error of the mean.

The accessible force range of the competition assay is limited due to the force dependence of the tethered probe peptide. At the lower limit, the tethered peptide is bound most of the time, thus blocking the binding site, and only very few binding events are observed. With increasing force, this number rises thus improving the statistical outcome. Simultaneously, the equilibrium of the tethered ligand is shifted to the open state. Increased dwell times in the open state can cause missed binding events of ligands from solution, which have fast off-rates in the range of the force-induced off-rates. This is usually not the case when the same ligand is used in solution and as tethered probe. Missed binding events would lead to an apparent force-dependent decrease of the off-rate. Therefore, a constant off-rate, as shown in Figure 23 and Figure 25, is an excellent proof that no binding events are missed. Another force-dependent constrain is the signal of the fluctuating state. For the analysis, the fluctuating state is treated as one level (see white traces in Figure 22 and Figure 24) with a mean position determined by averaging over the fluctuations. When the population distribution of the tethered ligand is shifted by force, also the average extension of the construct is shifted from the shorter closed position to the longer open position, while the signal of the quenched state remains at the position of the open state. Thus, the signal difference between quenched and fluctuating states decreases for increasing forces (Figure 24, white traces). As a consequence, data points were only taken starting from forces where a reasonable number of binding events could be observed. At the upper limit, we chose a force bias that produces a 50 % opening probability of the tethered

ligand, to ensure an exact separation between quenched and fluctuating states.

6.4 SUMMARY

In this chapter, we characterized the uninhibited multireceptor binding site found in FLNa21. We could directly test the mechanical stability of the interaction between binding regions of three different binding partners of filamin. To this end, we created and investigated fusion constructs, which had the ligands directly tethered to domain 21. In a second set of experiments, we directly measured the interaction of ligands from solution at zero load. We therefore developed a new single molecule mechanical competition assay, where the tethered peptide is used as a probe, which competes for the same binding site as ligands added into solution. The tethered peptides yielded the force-dependent binding and unbinding kinetics as well as the equilibrium free binding energy. This revealed a hierarchy in binding strength with GPIbα forming the most stable interaction. The same hierarchy is reflected in the on- and off-rates of ligands binding from solution. All three ligands exhibit similar on-rates, but have off-rates which differ by up to two orders of magnitude.

A comparison of both experiments gives an excellent agreement between directly measured off-rates (competition assay) and the extrapolated zero-load off-rates from force-dependent unbinding/binding rates. This is the first direct verification of the Berkemeier-Schlierf model (Section 5.6.2).

7

MECHANICAL RESPONSE OF THE AUTOINHIBITION

In a next set of experiments, we utilized the single-molecule mechanical competition assay (Section 6.2) to investigate the force-sensing mechanism of the domain pair 20-21 of human filamin A. As described in Section 2.3 the first β-strand or A-strand of domain 20 covers the multireceptor binding site of domain 21, thus autoinhibiting ligand binding. Can we see an autoinhibited conformation of the FLNa20-21 domain pair that is relieved with increasing loads?

7.1 STRETCH-AND-RELAX CYCLES REVEAL CONSECUTIVE UNFOLDING OF TWO DOMAINS

A force vs. extension curve of the domain pair FLNa20-21 is shown in Figure 26. Upon stretching (blue trace), we observe two major unfold-

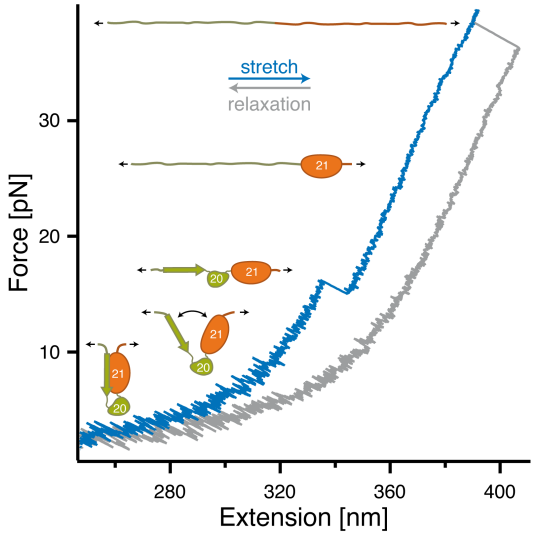

Figure 26: Low resolution stretch (blue) and relax (grey) trace of FLNa20. At forces around 15 pN, FLNa20 unfolds and at higher loads exceeding 30 pN, FLNa21 unfolds. Opening of the domain pair and release of the autoinhibition is not visible at this experimental resolution.

ing peaks around 15 and 37 pN, respectively. The lower peak exhibits a contour length change of $\Delta L = 17.7 \pm 0.3$ nm and the higher peak has a ΔL of 28.8 ± 0.5 nm. The lower force peak can be directly associated with unfolding of domain 20, while the high peak reflects unfolding of domain 21.

7.2 ISOLATED DOMAINS SHOW SAME BEHAVIOR AS IN DOUBLE DOMAIN CONSTRUCT

This assignment is confirmed by measurements with the isolated domains 20 and 21. Figure 27A shows an overlay of four typical force-extension curves of the single domain 20 construct including the A-strand (FLNa20). The colored traces represent extension traces, while grey traces show the relaxation. As in the two-domain construct (Figure 26), unfolding occurs at forces around 12 pN suggesting that also in the single domain the A-strand is detached from the rest of the folded domain body. The grey retraction curves display refolding at forces around 5 pN. As an example for single domain 21 unfolding, an overlay of four force-extension traces of a single domain 21 of human filamin A with tethered migfilin is shown in Figure 27B. The low-force binding/unbinding fluctuations of migfilin (cf. Figure 20E) are marked by a black arrow. At higher forces (25-30 pN), the unfolding of FLNa21 takes place as in the sample trace of the two-domain construct FLNa20-21. Furthermore, the migfilin peptide allows the demonstration that the peptide-domain interaction is specific for the folded structure of domain 21. After unfolding, the grey retraction curve shows no fluctuations compared to the extension trace at the corresponding force range around 6 pN. At zero load, the domain refolds, allowing repeated unfolding cycles with the same molecule. The mean unfolding force lies above the sampled maximal force of 35 pN. Therefore, unfolding events are rare and also happen during retraction cycles due to the slow moving speed of 10 nm/s. Compared

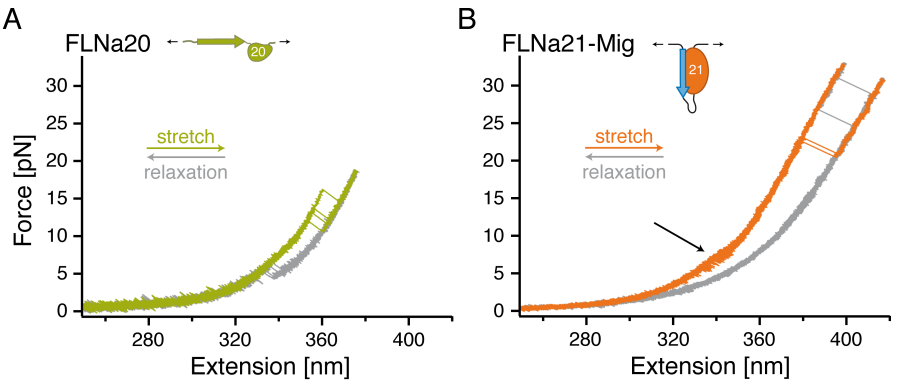

Figure 27: Single domain force-extension curves of FLNa20 and FLNa21. Colored traces represent extension traces, while grey traces show the relaxation. (A) Overlay of four stretch-and-relax cycles (50 nm/s) of one single domain 20 of human filamin A including the A-strand. (B) Overlay of four complete unfolding curves (10 nm/s of FLNa21-Mig. The black arrow at low forces markes the migfilin binding/unbinding fluctuations.

to other Ig-like domains of filamin [32, 103, 15], domain 20 appears

much more mechanically labile. This is independent of the presence of domain 21.

7.3 PASSIVE-MODE EXPERIMENTS WITH COMPETING LIGAND IN SOLUTION

A clear signal for opening the autoinhibited conformation, in which the A-strand of domain 20 is attached to domain 21, cannot be observed in the low resolution force-extension trace of Figure 26. The single-molecule mechanical competition assay now offers a possibility to study the force-dependent relief of autoinhibition and hence the force-sensing properties of the domain pair together with its force-dependent binding rate of ligands from solution. At a solution concentration of 2.7 µM GPIbα, a force-dependent change in the fluctuation pattern of the domain pair can be observed when held at a biasing force of 4.5 pN (Figure 28). As in Section 6.2, rapidly fluctuating high-σ regions are interrupted by quenched low-σ dwells. The quenched levels (e.g. right arrow in Figure 28) exhibit exactly the same lifetimes of GPIbα unbinding (τ_{bound} = 520 ms) as in Figure 22C. The high-σ regions in the high-bandwidth trace (left arrow) also re-

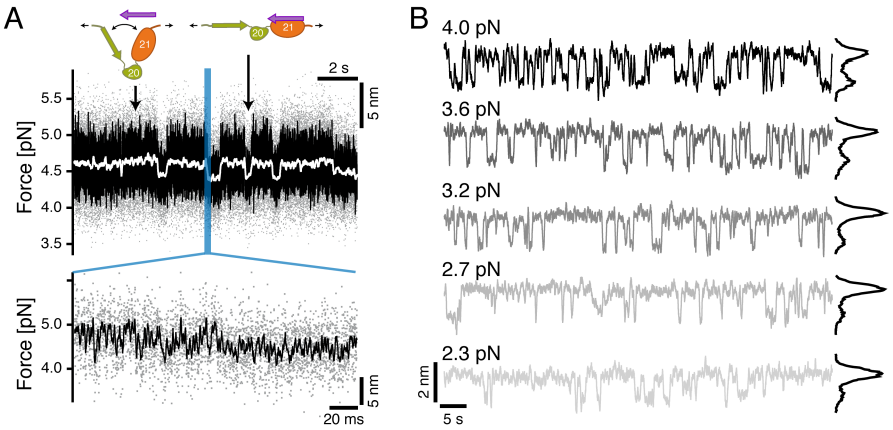

Figure 28: (A) Upper: competition assay of domain pair opening in the presence of 2.7 µM GPIbα peptide in solution observed at loads of 4.5 pN (color scheme as in Figure 22A). High-σ regions (opening-closing fluctuations) are interrupted with low-σ regions where bound peptide blocks fluctuations. Lower: zoom into a transition region. (B) Force-dependent binding of peptide from solution observed at biasing forces from 2.3 to 4.0 pN. From low to high loads, the binding probability (black histograms) increases constantly.

flect the same concentration dependence and pseudo first-order on-rate as before, which confirms the unbinding and rebinding of GPIbα peptides from solution. A zoom into the high-σ region (Figure 28A, inset) reveals that the molecular construct undergoes rapid transi-

tions between a closed and an open form. This can be seen in the strongly smoothed curves of Figure 28B. where increasing load increases the number of binding events observed. It is important to note that the force conditions shown were measured using the same molecule. The length change we observe between the closed and open conformations is 1.4 nm at a biasing force of 3.2 pN. From this length change, we can calculate a total contour length difference between the closed and open conformations of 14.5 ± 1.1 nm. This value is very close to the calculated contour length gain of 16.8 nm of a conformational change where the A-strand of FLNa20 detaches from FLNa21 and the domain pair opens up, as suggested by the crystal structure [65]. Combining the force and concentration-dependent binding kinetics of GPIbα to FLNa20 shown in Figure 29 allows reconstruction of the force-dependent gating-characteristics of the domain pair. In

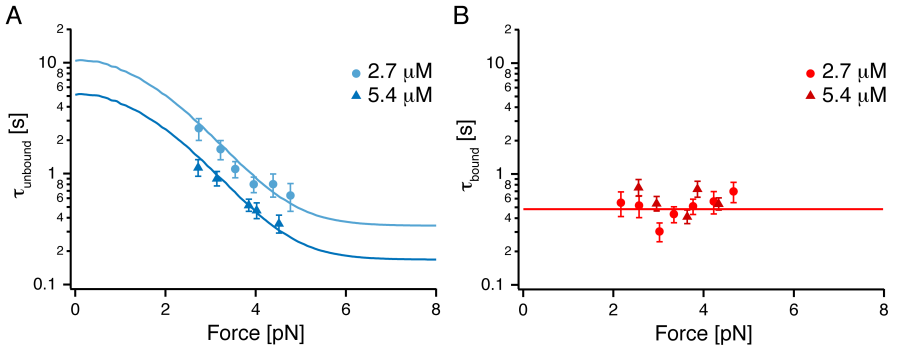

Figure 29: Force-dependent dwell times of GPIbα binding to FLNa20-21 measured with the single-molecule mechanical competition assay. (A) Dwell times of the unbound fluctuating state of FLNa20-21 with GPIbα at two different concentrations. (B) Dwell times of the bound or quenched state of FLNa20-21 for two different concentration of GPIbα. Solid lines are fits as described in Section 6.2.

Figure 30, three data sets at different peptide concentrations were normalized by their maximal peptide binding rates, giving a direct measurement of the force-dependent opening probabilities. The solid line represents the globally fitted opening probability with a force of half maximal opening $F_{1/2} = 3.9$ pN and a total free energy for opening of $2.8\, k_B T$. Furthermore, the force-dependent opening probability of FLNa20-21 was independently obtained (Figure 30, dashed line) from dwell time analysis of the unquenched regions using HMM analysis.

HMM analysis of FLNa20-21 opening

For the two-domain construct FLNa20-21, the probability to be in the open state $P_{open}(F)$ was determined with two independent methods. In addition to the solution-ligand based analysis, the equilib-

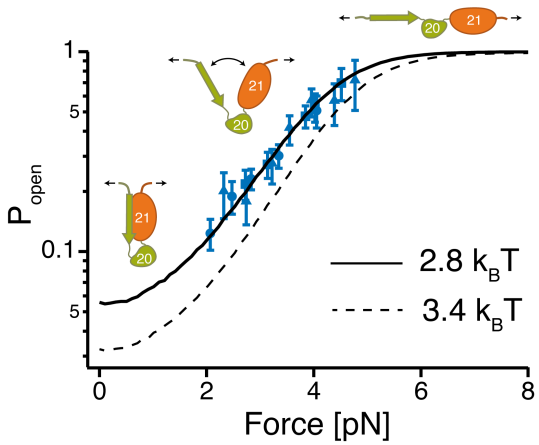

Figure 30: Force-dependent gating characteristics of the force-sensing domain pair as obtained from the force and concentration dependent dwell times of Figure 29A (blue data points, black solid line shows global fit). The three symbols (triangle, square and circle) denote three different solution concentrations. The dashed black line is an independent measure of the force-dependent opening probability as obtained from the HMM analysis of the fluctuating state where no ligand from solution is bound (Figure 31).

rium fluctuations of the A-strand opening were directly analyzed using the HMM state assignment. Figure 31A shows three sample traces of passive-mode measurements with HMM based assignment of the closed (upper, green) and open (lower, orange) state at three different biasing forces. Blue dashed lines mark state positions. The black line is a moving average of the 20 kHz data (colored lines) with 0.5 ms window size. Following the same procedure as for the tethered-ligand constructs presented in Section 6.1, the force-dependent opening probability (orange circles in Figure 31B) as well as the opening and closing kinetics (green circles and orange triangles in Figure 31C) could be determined. Because the analysis was carried out near the resolution limit at very low forces, we additionally tested the performance of the HMM analysis by reanalyzing data that was simulated using Brownian Dynamics and a Monte-Carlo model, based on the parameters extracted from the original data. As a comparison to the experimental data, Figure 31D shows three simulated passive-mode traces at biasing forces similar to data shown in Figure 31A. We performed Brownian Dynamics simulations of the experiment with the contour length and kinetic parameters given in Table 1 and Table 2 (for details see Section B.3). The simulated traces were analyzed with the same HMM based procedure as for the original data. The force-dependent probability of the simulated closed (green triangles) and open (orange circles) state is given in Figure 31E. The solid lines are global fits of Equation 12 to the original data shown in Figure 31B. Figure 31F are the force-dependent opening (green circles) and closing (orange triangles) rates of the simulated domain pair. Solid lines are

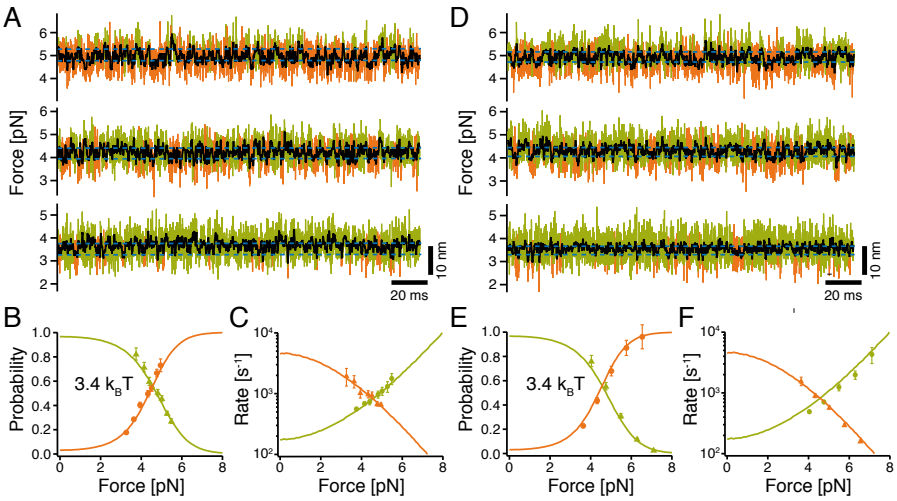

Figure 31: Kinetic HMM analysis of FLNa20-21 opening. (A)-(C) Experiment. (D)-(F) Simulation.

the zero-force extrapolations of the original data shown in Figure 31C. Notably, the original data and the simulation are in excellent agreement, which confirms the validity of our HMM analysis for low force conditions.

7.4 DISCUSSION

The force-gating characteristic we find for FLNa20 is tuned to surprisingly low forces. For comparison, the putative force-sensing titin-kinase domain acting in the high-force environment of muscle was reported to undergo force-activation at around 40 pN [43, 87]. However, *in vivo* and *in vitro* studies of the adhesion forces of integrins to fibronectin as well as the direct force-measurements within load-bearing focal adhesion of living cells have indicated that a relevant force scale within cells may be much lower: on the order of a few pN [55, 22, 37]. The force sensing of filamin seems to be tuned exactly to this force range. Another important aspect of the force sensing of filamin is its smooth opening characteristic. Unlike the common description of force induced structural changes within proteins as all or none events far from equilibrium, we find that filamin shifts its opening probability in a force-dependent and gradual manner from closed to open as indicated in the curve of Figure 30. This ensures a precise and well-controlled gating curve even though the involved binding energies lie below $4\,k_B\,T$. It has been argued that an autoinhibition of filamin seems unlikely in *in vitro* experiments, because it could be shown that an excess of ligand alone is able to convert the filamin domain pairs from a closed to an open conformation [49, 85]. However, this stood in apparent contrast to earlier reports that the isolated do-

main 21 binds stronger to ligands than the domain pairs [65], as well as to binding studies on strained filamin-crosslinked actin networks [27]. Our results are now able to reconcile this contradiction. Opening of the domain pair under load is, unlike a mechanical switch, a gradual process that shifts the binding constants by up to a factor of 17, and thus modulates affinity in a force-dependent manner.

A further important aspect of the force transmission through filamin is the transient and dynamic nature of the bonds involved. We find that even the strongest interaction of GPIbα with rod 2 domains of filamin, which critically determines platelet integrity under shear flow forces [19], is transient with a lifetime of less than a second even in the absence of force. How can a cell sustain mechanical loads applied over much longer time-scales? A view of the complete force transmission network helps to resolve this issue. Filamin does not offer only a single binding site to transmembrane receptors but instead, rod 2 has three reported domain pairs (Figure 32). Therefore,

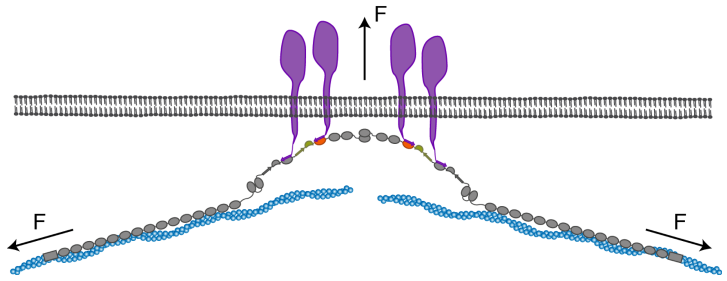

Figure 32: Model of the force-dependent binding and clustering of membrane receptors to filamin. Mechanical force in a strained cytoskeleton will lead to domain-pair opening in the rod 2 segment of filamin allowing the binding to membrane receptors. The simultaneous interaction with many domain pairs will significantly stabilize the cytoskeleton-membrane interaction and potentially induce clustering of receptors.

in a dimer of filamin, many interaction sites act in concert leading to a strong avidity effect. Because bond energies are additive, the lifetimes will increase exponentially, which leads to long-lasting multiple bonds. Interestingly, the binding to domain 17 is likely not autoinhibited [42]. The constitutively active domain 17 may be important for transiently recruiting filamin to the membrane receptor. The subsequent build-up of mechanical tension can then relieve the autoinhibition of the other domains promoting strong anchoring. The necessity of multiple parallel bonds for stable anchoring is in accord with the idea that the multiple binding sites of filamin can also induce clustering of transmembrane receptors [51, 73]. Alternatively, filamin interactions may be substituted or stabilized by other adaptor molecules. In the case of GPIbα, a candidate for such a molecule is 14-3-3ζ, which is required for firm adhesion and one of the 14-3-3ζ binding sites

on GPIbα overlaps with that of filamin [123]. An analogous function could be taken by talin in the case of integrin-based adhesion [65, 90].

In conclusion, we have shown that the rod 2 domain pair 20-21 of filamin acts as a force sensor that is precisely tuned to small forces in the low pN range. This force range is typically expected to act on single molecules in the cytoskeleton of cells. The dynamic equilibrium switching of this force sensor may provide a prototype for other force sensors found in living systems.

7.5 SUMMARY

Mechanical forces are important signals for cell response and development, but detailed molecular mechanisms of force sensing are largely unexplored. The cytoskeletal protein filamin is a key connecting element between the cytoskeleton and transmembrane complexes such as integrins or the von Willebrand receptor GPIb. In this chapter, I presented single-molecule mechanical measurements, which show how the immunoglobulin-like domain pair 20-21 of human filamin A acts as an autoinhibited force-activatable mechanosensor. We find that filamin force sensing is a highly dynamic process occurring in rapid equilibrium that increases the affinity to the target peptides by up to a factor of 17 between 2 and 5 pN. The observed equilibrium mechanism we find here can offer a general scheme for cellular force sensing.

8

FORCE-DEPENDENT ISOMERIZATION OF A CONSERVED PROLINE SWITCH

During the investigation presented in Chapter 7, we observed a peculiar folding behavior of FLNa20 that is caused by a native *cis* proline located in the last β-strand. Proline switches, controlled by *cis-trans* isomerization, have emerged as a particularly effective regulatory mechanism in a wide range of biological processes. In this chapter, I present single-molecule mechanical measurements, which we used to study the isomerization dependent folding of FLNa20. We will develop a full kinetic and energetic description of the highly conserved proline switch in the force sensing domain 20 and how prolyl isomerization modulates the force-sensing mechanism.

8.1 DOMAIN 20 EXHIBITS A BI-MODAL STABILITY

To study the force-dependent folding and unfolding dynamics of FLNa20 without the complicating interaction with FLNa21, we designed a construct where only the single domain FLNa20 was sandwiched between two ubiquitin domains, each carrying a cysteine residue to allow a dumbbell-type attachment of the construct in our optical tweezers experiment (see Figure 33A). A series of subsequent stretch (blue, orange) and relax (grey) cycles obtained on one molecule of FLNa20 is shown in Figure 33B. In stretch cycles, unfolding events can be observed both at high forces around 15 pN (traces in blue) as well as at low forces around 5 pN (traces in orange). Refolding readily occurs at forces around 3 pN in all traces at the pulling velocity used (200 nm/s). We already reported the high-force unfolding for the double and single domain constructs in Chapter 7 (FLNa20-21 in Figure 26 and FLNa20 in Figure 27A). The low-force unfolding is also observed in FLNa20-21 experiments but was omitted in Chapter 7 for the sake of clarity. The histogram of unfolding forces in Figure 33B (left) confirms that the observed unfolding events fall into two distinct classes. Both classes of unfolding events exhibit the same contour length increase (see Figure 33C). From this sample series, the switching kinetics between stable and unstable conformations can be estimated to several tens of seconds. Switching between conformations is reversible, hence permanent mechanical or chemical damage to the molecule cannot be an explanation for the observed effect. The observed switching kinetics is consistent with the proline isomerization kinetics seen in bulk experiments for oligopeptides [38].

All wildtype experiments were performed with a double-domain construct consisting of FLNa20-21 and a single-domain construct with FLNa20 alone. No difference between experiments with and without the presence of a folded domain 21 could be observed. Therefore, all data sets were combined in order to improve statistics.

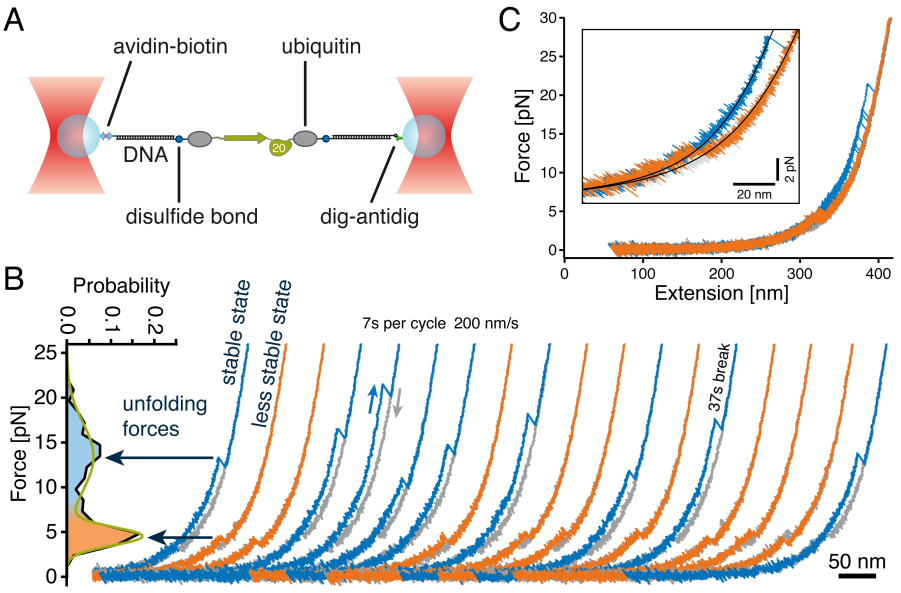

Figure 33: FLNa20 shows a bi-modal stability in single-molecule mechanical unfolding experiments. (A) Schematic of experimental setup. (B) Consecutive stretch-and-relax cycles of one single FLNa20 molecule. Successive stretch-and-relax cycles are separated by an x-offset and were moving-average filtered with a time window of 0.6 ms (raw data was recorded at 20 kHz). (C) Same traces as shown in (B) without an x-offset. The inset shows a zoom into the unfolding region of two sample traces, one stable and one less stable. The black lines represent a combined WLC model (see Section 5.1) fitted to the stable stretching traces.

8.2 A HIGHLY CONSERVED *cis* PROLINE CAUSES THE BI-MODAL STABILITY

A thorough examination of the FLNa20 structure led to the finding that FLNa20 exhibits a native *cis* proline just in front of the last β-strand (see Figure 34). Interestingly, a multiple sequence alignment shows that this *cis* proline residue is strictly conserved in all available 3D structures of filamin immunoglobulin-like domains (for details see Section 5.8.4).

To test this hypothesis, we removed the *cis* proline in position 2225 in the mutant P2225G. In this mutant mimicking the *trans* state of P2225, we only observed the low force population (see Figure 35A). As a control, removing the *trans* proline P2222 in the mutant P2222G led to no observable difference to the wildtype, and retained the bi-modal stability distribution (see. Figure 35B).

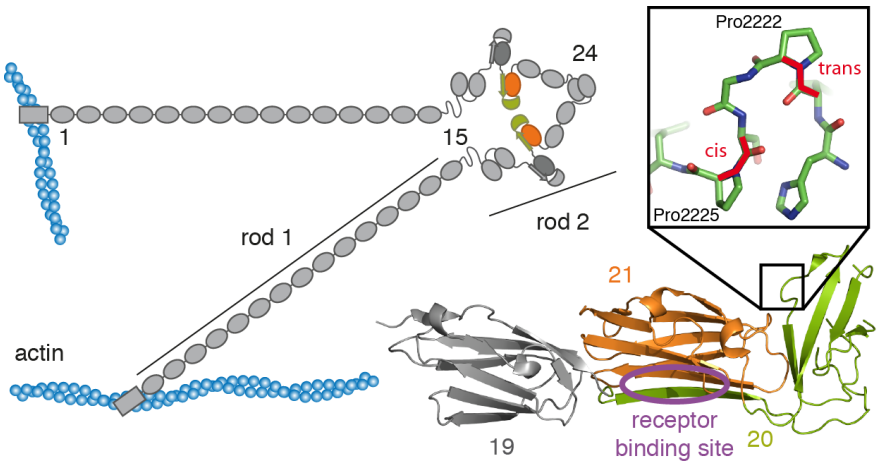

Figure 34: Native *cis* proline found in domain 20 of human filamin A. Left: Cartoon representation of a filamin dimer attached to actin. In the rod 2 region domain 19, 20 and 21 are color-coded dark grey, green and orange, respectively. Right: Crystal structure of domains 19-21 of human filamin A [65]. The receptor-binding region of domain 21 is marked in purple. Inset: Zoom into loop region in the G-strand of domain 20 where P2222 and P2225 are located. Peptidyl-prolyl bonds are marked in red.

8.3 FORCE-DEPENDENT FOLDING AND UNFOLDING

To observe the slow proline *cis-trans* isomerization kinetics in real time with a single molecule, we performed extremely long passive-mode experiments (see Figure 36, upper). We find, that the molecule switches between two states: one where the unfolded state (grey) dominates with interspersed short-lived folding events (orange) and another stable state where the native state dominates (blue) with only rarely populated unfolded states. The assignment of the respective *cis* and *trans* states is marked in the bar above the trace with *trans* states colored in dark grey and *cis* states in light grey, respectively. A zoom into the transition region between a *cis* and a *trans* state illustrates the differences in protein stability associated with isomerization (see Figure 36, lower right). It is important to note that both folded and unfolded states are populated in both *cis* and *trans* conformation, albeit with drastically different population probabilities. We can identify 4 different states (N_{cis}, U_{cis}, N_{trans}, U_{trans}) with the following lifetimes: $\tau_{N_{cis}}$, $\tau_{U_{cis}}$, $\tau_{N_{trans}}$, and $\tau_{U_{trans}}$, which are shown in the scatter plot of protein extension vs. dwell time (see Figure 36, lower left). In the *cis* state, we consistently observe the population of a short-lived intermediate state (see arrow in zoom of Figure 36) that is off-pathway for the unfolding transition, and hence, we lump this state into the lifetime of the native state (for more information and a structural interpretation please refer to Section A.1). A full kinetic and ther-

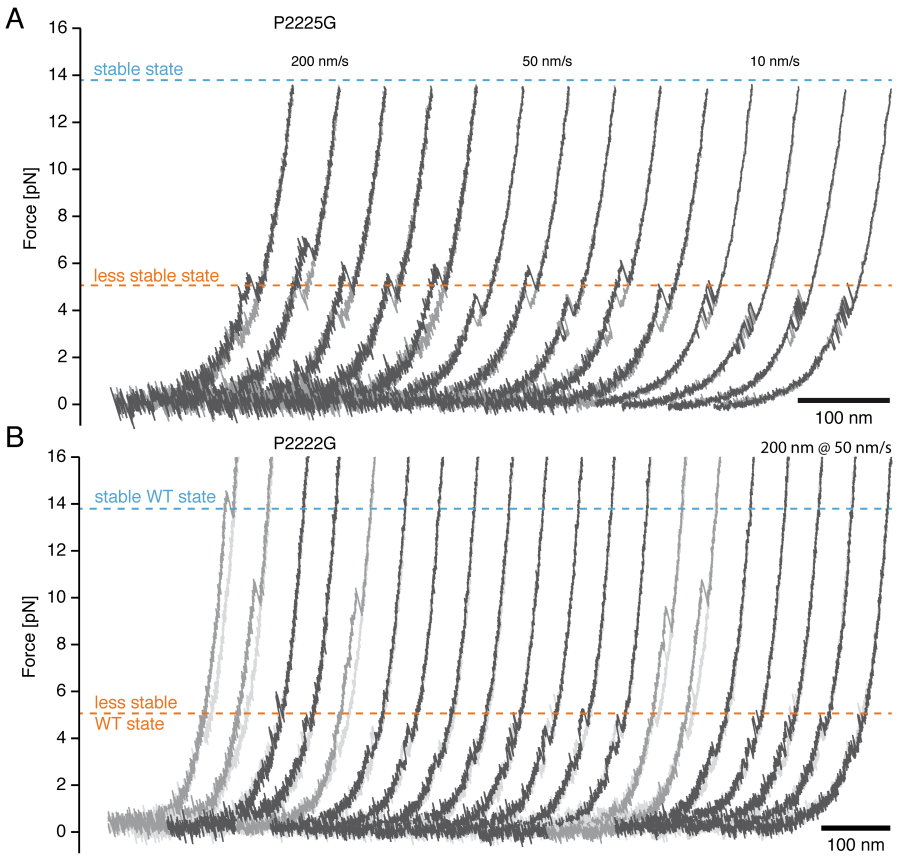

Figure 35: Stretch-and-relax cycles of two different proline-to-glycine mutants of FLNa20. The mean unfolding force found for the two native states of the wild type domain (see Figure 33B) are marked by a blue (stable state) and orange (less stable state) dashed line. (A) The P2225G mutant shows only the less stable (orange) state. (B) The P2222G mutant behaves as the wild type domain.

modynamic description of proline isomerization and its coupling to folding requires knowledge of all rates shown in the thermodynamic box model of Figure 37A. The protein can apparently exist in two distinct folded (N_{cis}, N_{trans}) as well as unfolded states (U_{cis}, U_{trans}). The horizontal transitions describe the folding/unfolding kinetics in the *cis* and *trans* states, while the vertical transitions describe proline isomerization rate constants in the native and unfolded states, respectively.

We first characterized the horizontal transitions, i. e. the force-dependent folding and unfolding kinetics in both *cis* and *trans* states (see Figure 37B). To separate *cis* from *trans* states, we used the vastly different lifetimes of their respective native states. The dwell time scatter plot in Figure 36 shows that, in the native state, two clouds (blue and orange) can be observed with lifetimes different by at least two orders of magnitude. Based on this criterion, we split the passive-mode traces and analyzed force-dependent folding kinetics as well

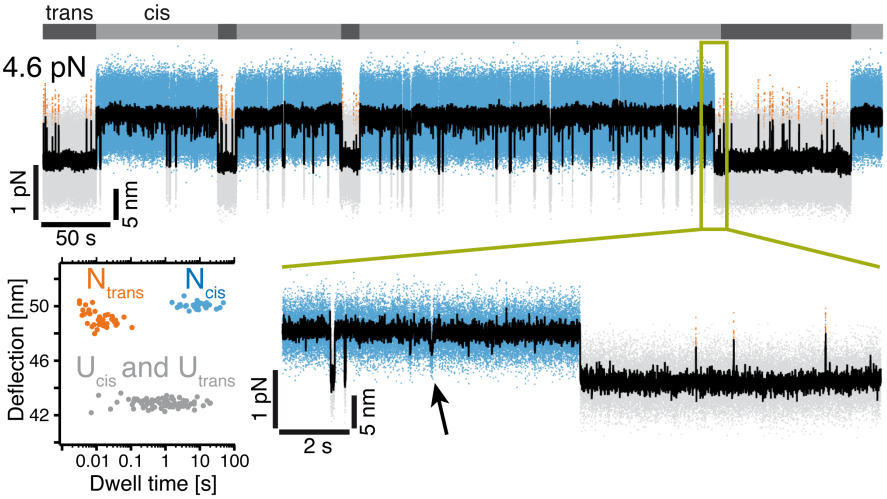

Figure 36: Extremely long and stable passive-mode trace of FLNa20 at a force bias of 4.6 pN acting on the unfolded state. The colored trace corresponds to 5-kHz data where the stable long lived native state N_{cis} is colored in blue, the less stable short lived N_{trans} in orange and both unfolded states U_{cis} and U_{trans} in light grey. The black trace was moving-average filtered with 4.2 ms time window. Above, the light and dark grey line denotes the *cis* and *trans* state. The zoom below shows a *cis* to *trans* transition and illustrates the different folding stabilites. A short-lived off-pathway intermediate observed in the *cis* state is marked with an arrow. On the lower left, a deflection vs. dwell time scatter plot shows, that the two native states N_{cis} and N_{trans} are kinetically well separated.

as equilibrium energetics for both states separately (for details see Section 5.8.1). Force-dependent Chevron plots as well as population probabilities are shown in Figure 37B. To enhance the accessible force range of our measurements to both the higher and lower ends for the *cis* state folding kinetics, we also performed force jump experiments, where the molecule was rapidly (within 10 µs) stepped to a high load to measure (circles in Figure 37B) (for details on jump experiments, see Section 5.8.2). For a summary of all measured thermodynamic and kinetic parameters see Table 4.

8.4 ISOMERIZATION KINETICS

We now turn towards the vertical transitions in our kinetic model (see Figure 37A) describing the kinetics of *cis-trans* isomerization in native and unfolded states, respectively. Figure 38 shows the population of *cis* (light grey) and *trans* states (dark grey) in passive-mode traces obtained at different bias forces (see Figure 39 for zooms into the *cis-trans* transition region). A strong dependence of the *cis-trans* population on mechanical force can be observed. At high loads (top trace) where the molecule is predominantly in the unfolded state, the

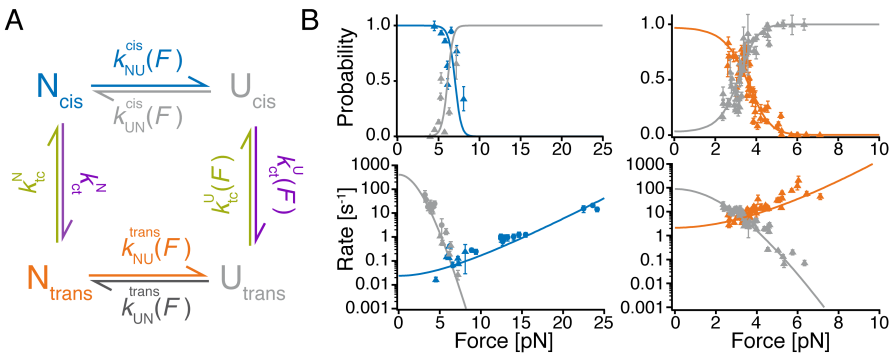

Figure 37: (A) Kinetic model for the folding and prolyl isomerization of FLNa20. (B) Unfolding and folding of *cis* (left) and *trans* state (right). The force-dependent equilibrium probabilities for the native (colored) and unfolded state (grey) are given in the upper graph while the lower shows the force-dependent unfolding (colored) and folding (grey) rates measured in passive mode (triangles) and jump experiments (circles).

trans state prevails. At lower loads, this population shifts strongly towards the *cis* state (middle and bottom trace). Apparently, the folding state of the protein strongly affects the *cis-trans* equilibrium of residue P2225. The assigned dwells in the *cis* and *trans* states now enable us to determine the load-dependent isomerization kinetics. It is important to note that the single-molecule traces do not directly allow for the observation of isomerization events, but we rather conclude on an isomerization event indirectly through the altered folding/unfolding kinetics as described above.

EXPERIMENT	WT		P2225G
FOLDING	$U_{cis} \rightarrow N_{cis}$	$U_{trans} \rightarrow N_{trans}$	$U \rightarrow N$
k^0_{UN} , s^{-1}	410 ± 60	89 ± 2	60 ± 10
ΔL_{UT} , nm	18.4 ± 0.6	19.5 ± 0.3	16.8 ± 0.9
UNFOLDING	$N_{cis} \rightarrow U_{cis}$	$N_{trans} \rightarrow U_{trans}$	$N \rightarrow U$
k^0_{NU} , s^{-1}	0.023 ± 0.002	2.1 ± 0.1	0.07 ± 0.01
ΔL_{NT} , nm	2.2 ± 0.3	7.5 ± 0.5	16.6 ± 0.6
ΔG^0 , $k_B T$	10.8 ± 1.1	3.4 ± 0.3	5.0 ± 0.5

Table 4: k^0_{UN} and k^0_{NU} are the folding and unfolding rates extrapolated to zero load. ΔL_{UT} and ΔL_{NT} are the distances from the initial unfolded (U or N) to the transition state (T) measured in contour length. Errors are given as the SEM.

Therefore, we cannot determine whether an isomerization event has occurred in the native or unfolded state of the protein. Hence, the

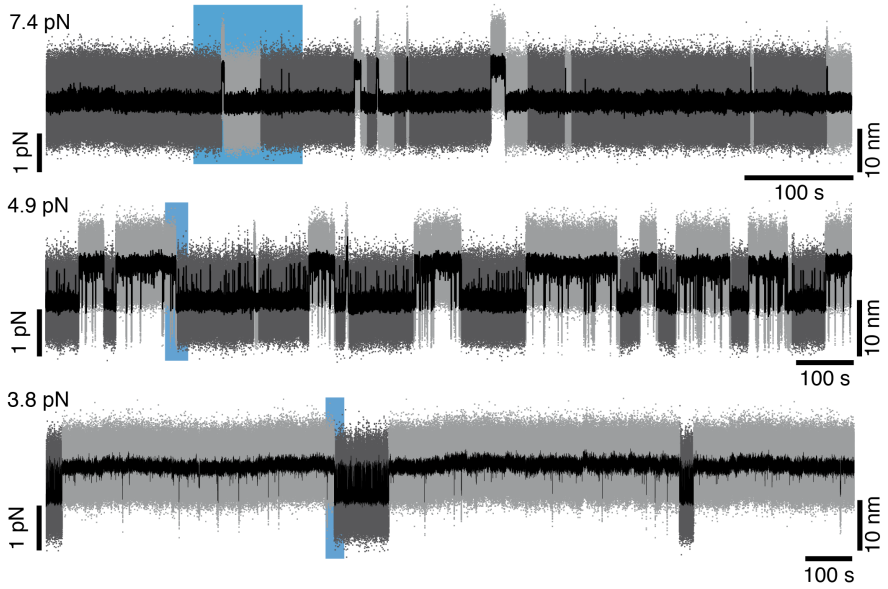

Figure 38: Extremely long and stable passive-mode traces at different biasing forces. Grey colored traces represent 5-kHz data where the *cis* and *trans* states are colored in light and dark grey, respectively. With rising force bias (from bottom to top) a drastic shift in the *cis-trans* population from *cis* to *trans* is observed. The black trace was moving-average filtered with 4.2 ms time window.

isomerization kinetics we observe is an apparent rate k_{ct}^{app} reflecting the sum of the rates of isomerization in the unfolded and in the native states according to:

$$k_{ct}^{app} = \left(1 - P_{U_{cis}}(F)\right) \cdot k_{ct}^{N} + P_{U_{cis}}(F) \cdot k_{ct}^{U}(F) \tag{28}$$

$$k_{tc}^{app} = (1 - P_{U_{trans}}(F)) \cdot k_{tc}^{N} + P_{U_{trans}}(F) \cdot k_{tc}^{U}(F) \tag{29}$$

where $P_{U_{cis}}(F)$ and $P_{U_{trans}}(F)$ are the measured force-dependent population probabilities for the unfolded protein shown in Figure 37B. k_{ct}^{N}, $k_{ct}^{U}(F)$, k_{tc}^{N} and $k_{tc}^{U}(F)$ are the microscopic isomerization rate constants for the unfolded (U) and native (N) states. The isomerization rate constants for the native state can be assumed to be force-independent because in the folded structure, the prolyl bond does not bear much load as force propagates through multiple parallel β-sheets. On the contrary, in the unfolded structure the force acts directly on the prolyl bond and is therefore force-dependent. Hence, the apparent isomerization rates (k_{ct}^{app} and k_{tc}^{app}) are plotted against the force acting on the unfolded protein. The force dependence of $k_{ct}^{U}(F)$ and $k_{tc}^{U}(F)$ is described by the Bell model introduced in Section 5.6. Figure 40A shows the observed apparent *cis-trans* rate k_{ct}^{app} and Figure 40B the apparent *trans-cis* rate k_{tc}^{app}.

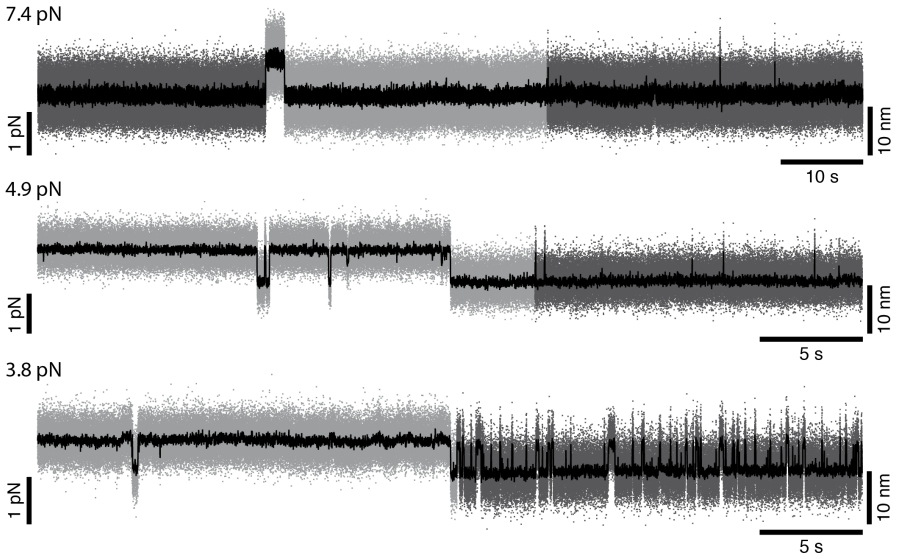

Figure 39: Zoom into traces of Figure 38 (blue areas). The extremely stable passive-mode measurements allow a detection of all timescales spanning six orders of magnitude, from fast unfolding ($1 \times 10^3\,s^{-1}$) to slow isomerization ($1 \times 10^{-3}\,s^{-1}$). Same color-code as Figure 38.

To compensate for deviations in trap stiffness calibration among different molecules, we corrected the forces acting in the measurement by using the load dependent population probabilities of the *trans* state as determined in Figure 37B (upper right). This recalibration procedure reduced the force scatter in the rate plots of Figure 40A and Figure 40B considerably. As described above, in addition to the passive-mode experiments (triangles in Figure 37B and Figure 40A), we also performed force jump experiments to enhance the accessible force range (circles in Figure 37B lower left, see Section 5.8.2). A fit to Equation 28 and Equation 29 yields the force-dependent vertical rate constants $k_{ct}^{U}(F)$, $k_{tc}^{U}(F)$ and the force-independent rate constant k_{tc}^{N}. Because in Figure 37A the lowest accessible data point is around forces of 4 pN, a fit cannot provide a very good estimate for k_{ct}^{N}. However, because in a cyclic thermodynamic path at equilibrium the product of the equilibrium constants must equal 1, k_{ct}^{N} is not a free parameter any more and can be directly calculated from the principles of detailed balance [118]. A summary of all rate constants including their force dependence can be found in Table 5. We find that the folding state of the protein exclusively affects the *cis-trans* isomerization. When the protein is folded, *cis-trans* isomerization (k_{ct}^{N}) is slower by more than 3 orders of magnitude as compared to the unfolded state ($k_{ct}^{U}(F)$). In contrast, k_{tc}^{N} and $k_{tc}^{U}(F)$ are identical within the resolution of our measurement indicating that the folding state of the protein domain does not influence *trans-cis* isomerization. The slopes of the plots in Figure 40A and Figure 40B at high loads (where the pro-

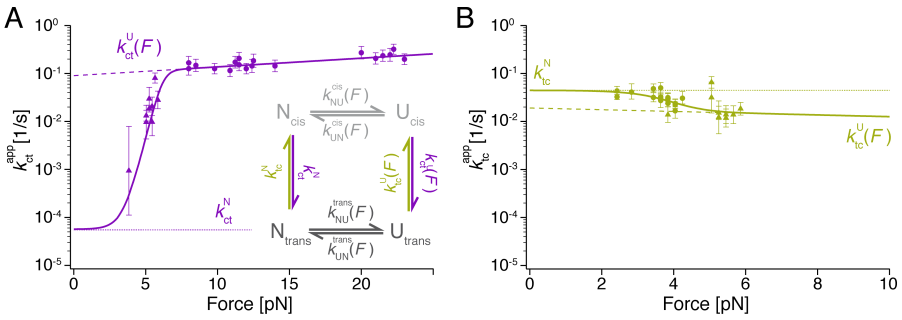

Figure 40: (A) Force-dependent *cis* to *trans* isomerization rates measured in passive mode (triangles) and jump experiments (circles). The dashed line corresponds to $k_{ct}^{U}(F)$, the dotted to k_{ct}^{N} and the continuous line to the probability weighted sum (Equation 28). (B) Force-dependent *trans* to *cis* isomerization rates measured in passive mode with same line style as in (A).

tein is unfolded) also allow estimating how force couples directly to the isomerization kinetics in the unfolded state. The extremely shallow slope (see dashed line in Figure 40A) indicates a very weak coupling to force consistent with transition state positions on the order of around one Ångström [17, 115].

ISOMERIZATION	k_{ct}^{0} , s^{-1}	k_{tc}^{0} , s^{-1}	$K_{ct/tc}$	
$N_{cis} \rightleftharpoons N_{trans}$	5.5×10^{-5}	0.046 ± 0.004	1.2×10^{-3}	1.2×10^{-3}
$U_{cis} \rightleftharpoons U_{trans}$	0.09 ± 0.02	0.019 ± 0.002	0.53	12.7
Δx , nm	0.17 ± 0.05	(0.17)	$F = 0\,pN$	$F = 10\,pN$

Table 5: Isomerization rates extrapolated to zero load for the native state (first row) and the unfolded state (second row). $k_{ct}^{N,0}$ is calculated based on the principles of detailed balance. Δx is the transition state distance from the unfolded state. For *trans–cis* isomerization, the accessible force range was not sufficient for a reliable fit with Δx as a free parameter. A symmetric value relative to the fitted *cis–trans* Δx is given in parentheses. The subdivided fourth column shows the equilibrium constant calculated for two different forces. Errors are given for all fitted parameters as the SEM.

8.5 DISCUSSION

Proline isomerization is a ubiquitous phenomenon in classical assays of protein folding [117]. It may therefore be surprising that proline isomerization has so far been elusive in single-molecule protein folding studies. A simple reason may be that the accessible observation time spans in single-molecule studies have often been limited to less than

a minute. The development of ultra-stable optical traps has made it possible to observe single molecules over minutes up to hours at time-resolutions in the sub-millisecond range [76, 116, 13, 108]. This technique is hence ideally suited to study, on the single-molecule level, the slow-time-scale heterogeneity that proline isomerization imposes on protein folding.

Furthermore, the unambiguous extraction of rates in complex thermodynamic reaction schemes can be tedious and is, in many cases, impossible using bulk methods. For the cyclic scheme in Figure 37A, all 8 kinetic rate constants cannot be extracted without assumptions [48]. We would like to point out that the direct access to rate constants possible in single-molecule experiments overcomes such limitations as we show in this study.

Proline isomerization rates have been studied extensively for peptides using spectroscopic methods. While the details of isomerization kinetics depend on the sequence of the flanking amino acids, in general, the kinetics is in the range of several minutes near 15 °C with $k_{tc}^{peptide}$ being a factor of 1-9 slower than $k_{ct}^{peptide}$ [126]. The kinetics of proline isomerization we find at 28 °C for the unfolded state ($k_{ct}^{U,0} = 0.09\,s^{-1}$, $k_{tc}^{U,0} = 0.019\,s^{-1}$) lie well within this range, if we consider the acceleration of the isomerization due to higher temperature.

Although in folded protein structures the majority of prolines is found in the *trans* state, there are a number of reported protein structures where the proline exhibits *cis* conformation. Among those, a small subset tolerates both proline conformers, albeit with different folding free energies and sometimes even different structures [53]. Such conformational heterogeneities are difficult to detect by structural methods if the relative population of the two native state conformations differ significantly [54]. For FLNa20, we find that the isomerization state of P2225 mostly affects the unfolding rate of the native state ($k_{NU}^{cis,0} = 0.023\,s^{-1}$ vs. $k_{NU}^{trans,0} = 2.1\,s^{-1}$), while folding rates are similar for *cis* and *trans* conformations ($k_{UN}^{cis,0} = 410\,s^{-1}$ vs. $k_{UN}^{trans,0} = 89\,s^{-1}$). The difference in free energy between the two states is $7.4\,k_B\,T$ making N_{cis} more than 3 times more stable than N_{trans}. In contrast, in a study of the N2 domain of the gene-3 protein of the filamentous phage fd by Jakob and Schmid, the isomerization state of proline 161 was reported to alter folding kinetics while leaving unfolding kinetics unaffected. Hence, in this protein, the proline residue is structured in the transition state of folding.

Proline isomerization not only affects folding, but in turn, the isomerization process is strongly influenced by the folding state of the protein [53]. Hence, in our case, the free energy liberated during the folding process can stabilize the *cis* over the *trans* conformation by either speeding up k_{tc}^{app} or slowing down k_{ct}^{app}, or a mixture of both. In FLNa20, we find that only k_{ct}^{app} is slowed down by more than 3 orders

of magnitude ($k_c t^N = 5.5 \times 10^{-5}\,s^{-1}$ vs. $k_{ct}^{U,o} = 0.09\,s^{-1}$) while k_{tc}^{app} is unaffected. Even though we don't have a structural interpretation for the clear partitioning of this effect into only one rate constant, it might suggest that the structural environments of P2225 are so distinct that the transition of *trans* to *cis* is not directly catalyzed, whereas the structured environment around *cis* P2225 directly increases the lifetime of the *cis* state. Another explanation rationalizing the lack of effect of folding on k_{tc}^{app} may be the superposition of compensating effects. An increased free energy bias toward *cis* would increase k_{tc}^{app}, but the constraints of a folded protein would slow down conformational changes. In the case of k_{ct}^{app}, these effects would reinforce each other to reduce the rate. A clear distinction between the two mechanisms is not possible at this point.

It has been suggested that mechanical forces may affect the function of mechanosensitive proteins by inducing *cis* to *trans* switching of proline residues [17]. Because the backbone length of a *cis* state of a proline is slightly shorter than in the *trans* state (on the order of around 1 Å [89]), one would expect that, in an unfolded polypeptide, mechanical load shifts the equilibrium even further towards the *trans* state. This effect can be observed in the high force region of the plots in Figure 40A and Figure 40A, where $k_{ct}^{app} \approx k_{ct}^{U}$ and $k_{tc}^{app} \approx k_{tc}^{U}$ since $P_N \approx 0$ and $P_U \approx 1$. A slight slope of the rate constants can be observed while k_{ct}^{app} increases with force and k_{tc}^{app} decreases. Consistent with the small ~ 1 Å length change associated with proline switching, these slopes are very shallow. A more detailed analysis would require the application of much higher loads as has been shown in molecular dynamics experiments [17]. Because the forces acting on filamin in its cytoskeletal environment are likely to be lower than tens of pN, we exclude force regulation through direct mechanical action on prolyl bonds.

Our measurements suggest, however, that a much more sensitive regulation of protein states through mechanical forces can be achieved by mechanical unfolding of a protein. The plot of the force-dependent change of k_{ct}^{app} in Figure 40A shows that in the region between 3 and 7 pN, where the *cis* conformation of FLNa20 unfolds, the switching rate of the P2225 changes by more than 3 orders of magnitude. In this context it is important to remember that FLNa20 together with its adjacent domain FLNa21 constitutes a mechanosensor domain pair as described in Section 2.3 and investigated experimentally in Chapter 7 (see Figure 41, lower left). At forces around 4 pN, the domain pair 20-21 opens up and thus exposes and activates the integrin/GPIb binding site on domain 21, while both domains still remain folded (see Figure 41, lower middle). If force increases further, domain 20 will unfold and destroy the environment that keeps P2225 stably in its *cis* conformation (see Figure 41, lower right). If forces act for a prolonged time, domain 20 will remain unfolded and a *cis* to *trans* switch can oc-

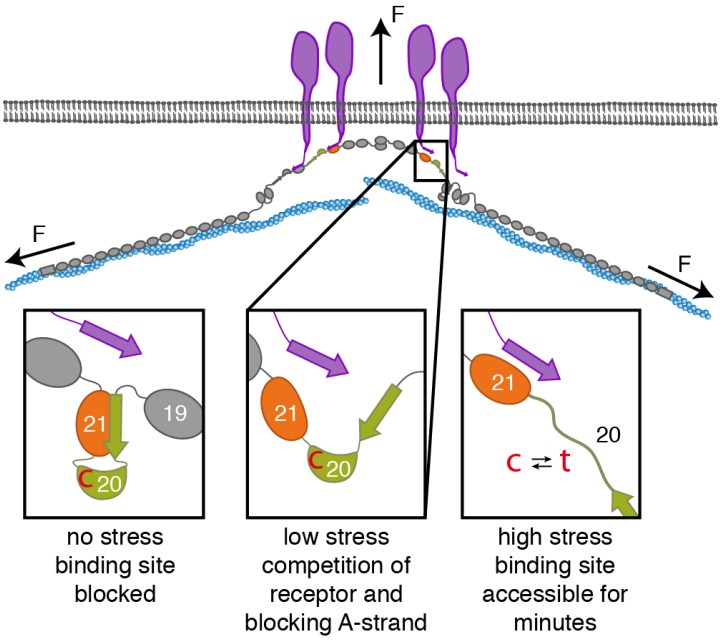

Figure 41: When unstrained, FLNa20 covers the receptor binding site present in FLNa21 (left box). Mechanical force in a strained cytoskeleton will lead to domain pair opening in the rod 2 segment of filamin, allowing the binding to membrane receptors (middle box). Under high stress FLNa20 unfolds and P2225 can isomerize to *trans* leading to a native state (N_{trans}) with drastically reduced stability (right box). The binding site would stay accessible even at lower forces up to minutes until P2225 isomerizes back into the *cis* state.

cur within a few seconds. Now, already very low forces will shift the equilibrium of domain 20 far into the unfolded state, preventing the autoinhibition of the binding site on domain 21 over tens of seconds until the proline switches back and FLNa20 folds into the more stable state N_{cis}, which allows the autoinhibition through domain-pair formation. Interestingly, a recent study using magnetic tweezers has suggested that FLNa20 may exist in two different unfolded forms [16]. Here, we provide evidence that the underlying mechanism is in fact proline isomerization.

Intriguingly, the presence of a *cis* proline within the G-strand is not exclusive to human FLNa20. A closer look at the structures of 36 different filamin domains including domains 4 to 5 of *Dictyostelium discoideum* reveals a *cis* proline in the same domain region. A multiple sequence alignment shows that this proline is the only residue that is 100% conserved in filamins (see Figure 18). It is often (80%) followed by a bulky aromatic residue (Tyr or Phe) known to stabilize the proline *cis* isomer [75]. This strong conservation is remarkable given an overall sequence identity of only 26% on average, and because *cis* prolines occur in less than 5% of the proteome [68]. For example immunoglobulin domains from other proteins like myomesin or titin do

not exhibit this *cis* proline. Even though we cannot clearly attribute a role for the *cis-trans* switch in all 24 domains of filamin, our results here highlight the potential consequences of such a switch for modulating protein stability and mechanosensing of this important cytoskeletal protein.

A proline-dependent switch mechanism has also been suggested for the shear sensing domain A2 of von Willebrand factor albeit with no direct experimental evidence [124]. A2 contains a native *cis* proline which may isomerize to *trans* after shear stress induced unfolding of domain A2. This isomerization would lead to greatly delayed refolding thus expediting cleavage by ADAMTS13 of von Willebrand factor during vessel repair. These examples suggest an emerging general role for proline *cis-trans* switches in mechanosensing.

The combination of high sensitivity and stability that can be achieved with state of the art optical trapping has allowed us to study the full kinetics and energetics of the coupling of a highly conserved proline switch to protein folding in a mechanosensor protein. More complex and physiologically relevant protein systems can now be studied in single-molecule mechanical assays.

8.6 SUMMARY

Proline switches, controlled by *cis-trans* isomerization, have emerged as a particularly effective regulatory mechanism in a wide range of biological processes. In the work presented in this chapter, we used single-molecule mechanical measurements to develop a full kinetic and energetic description of a highly conserved proline switch in the force-sensing domain 20 of human filamin and how prolyl isomerization modulates the force-sensing mechanism. Proline isomerization toggles domain 20 between two conformations: a stable *cis* conformation with slow unfolding favoring the autoinhibited closed conformation of filamin's force-sensing domain pair 20-21, and a less stable, uninhibited conformation promoted by the *trans* form. The data provide detailed insight into the folding mechanisms that underpin the functionality of this binary switch and elucidate its remarkable efficiency in modulating autoinhibition, thus combining two previously unconnected regulatory mechanisms: proline switches and mechanosensing.

9

OUTLOOK: THE EFFECT OF ISOMERASES ON A SINGLE PROLINE SWITCH

As described in Section 3.2, a whole enzyme machinery is involved in catalyzing *cis-trans* isomerization of proteins *in vivo* [70, 110, 96, 97]. Now that we can study the peptidyl-prolyl isomerization at the single-molecule level, we can take one further step in complexity and examine the influence of *cis/trans*-prolyl isomerases (e. g. FK506 bindig protein, cyclophilin or parvulin) on isomerization-dependent folding of proteins under load.

In this chapter, I describe how a *cis/trans* isomerase affects the proline switch investigated in Chapter 8. We tested two different enzymes: human CypA and bacterial SlyD from *Escherichia coli*. In the end, we chose SlyD as model enzyme because it is very well characterized and exhibits a high solubility as well as chemical and thermal stability (see Section 3.2). In contrast to the three projects reported in Chapter 6, Chapter 7 and Chapter 8, the following chapter is a status report about ongoing research. Therefore, there will be a major outlook section where I present first results and promising experimental approaches along with open questions.

CypA and SlyD belong to the family of cyclophilin and FKBP isomerases, respectively (see Section 3.2.1 and Section 3.2.2). Peptidyl-prolyl *cis/trans* isomerases catalyze the isomerization of the peptidyl-bond by lowering the high barrier separating the *cis* and *trans* isoforms. Therefore, we expect faster switching kinetics when adding an isomerase to the experiments used to investigate the proline switch reported in Chapter 8. In our mechanical single-molecule assay with FLNa20, we can achieve the best time resolution when measuring the *trans* lifetimes with the jump assay described in Section 5.8.2. After a jump to high forces above 10 pN the isomerization state is tested at low forces around 3.5 pN. Molecules in the *trans* state will rapidly fluctuate between folded and unfolded states, while *cis* molecules will stably lock into the native state. In such an experiment, the time resolution for *trans* dwell times is limited by the *trans* unfolded lifetimes, which at 3 pN are on the order of 100 ms (Figure 46, right). Addition of CypA and SlyD to these jump experiments indeed led to an accelerated *trans*-to-*cis* switching. The *trans* lifetime of FLNa20 was reduced from (37.2 ± 5.6) s to (15.3 ± 1.7) s in the presence of 7.2 µM CypA. The *trans* lifetime could be recovered to a no-CypA value of (32.4 ± 4.8) s when adding the CypA inhibitor cyclosporin A in an equimolar concentration into solution. This was tested for jump experiments with 3.6 and 7.2 µM of CypA/cyclosporin A. In the case

of SlyD, the catalytic effect was even more pronounced. Addition of 7.25 µM SlyD decreased the *trans* lifetime to (1.55 ± 0.05) s. As mentioned above, we chose SlyD as model isomerase for further investigations. Figure 42 shows the apparent *trans-cis* isomerization k_{tc}^{eff} of

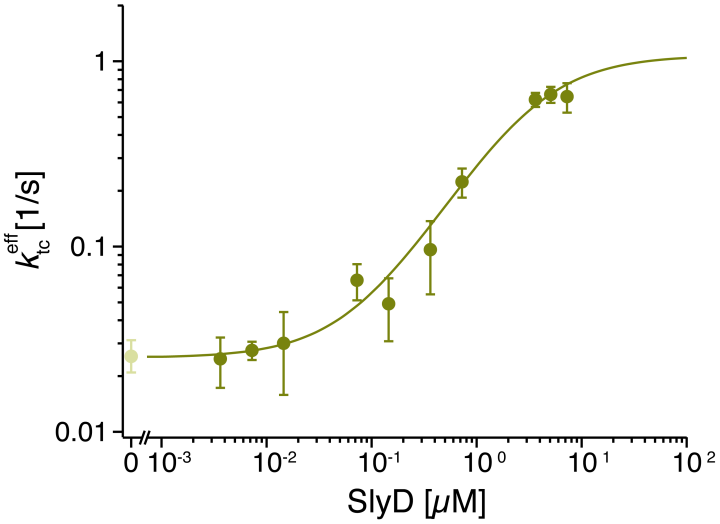

Figure 42: SlyD accelerates isomerization. The effective *trans*-to-*cis* isomerization rate increases with rising SlyD concentration and can be fitted with a Langmuir isotherm.

FLNa20 at 3.5 pN in dependence of the SlyD concentration. In the double logarithmic plot, k_{tc}^{eff} rises by almost two orders of magnitude from $0.025\,s^{-1}$ to $1.077\,s^{-1}$ following a Langmuir isotherm with a K_D value of 3.3 µM. Apparently, the *trans-cis* isomerization is accelerated in the presence of a micromolar SlyD concentration and governed by the binding process of SlyD to filamin. By using the jump assay, we have enough time resolution to resolve the *trans-cis* isomerization kinetics, which level around $1\,s^{-1}$.

9.0.1 *Langmuir isotherm describes the acceleration of trans-cis isomerization*

In the case of a single-molecule experiment, the classic ensemble approach of Michaelis-Menten can not be used to describe the catalytic action of the enzyme SlyD. In our case, we are observing one single substrate molecule and titrate the enzyme concentration. Therefore, we have to use the binding probabilities for a single receptor instead of concentrations.

In Section 5.7 we derived the probabilities for a single receptor to be bound (Equation 22) or not bound (Equation 23) to a ligand in dependence of the ligand concentration. In our case, FLNa20 represents the single receptor and the ligand corresponds to the SlyD added into solution. Furthermore, we assume that SlyD binding catalyzes the *cis*/*trans* isomerization in that SlyD binding switches the *trans*-

to-*cis* isomerization rate from the slower wildtype rate k_{tc}^{app} into the catalyzed faster rate $k_{tc}^{app,\,SlyD}$. This can be expressed as

$$k_{tc}^{eff}([SlyD]) = k_{tc}^{app} \cdot P_{unbound}([SlyD]) + k_{tc}^{app,\,SlyD} \cdot P_{bound}([SlyD]). \quad (30)$$

In Figure 42 the green line represents a fit of Equation 30 to the effective *cis*-to-*trans* rate data determined during jump experiments. The WT isomerization rate k_{tc}^{app}, the catalyzed rate $k_{tc}^{app,SlyD}$ as well as the dissociation constant K_D are free parameters. These were fitted to $k_{tc}^{app} = (0.025 \pm 0.003)\,s^{-1}$, $k_{tc}^{app,\,SlyD} = (1.077 \pm 0.197)\,s^{-1}$ and $K_D = (3.3 \pm 1.2)\,\mu M$. Notably, the model assumes only one free binding site. Because the fit is in excellent agreement with the data, we conclude that the catalytic action of SlyD on FLNa20 is not a cooperative process. This does not exclude the simultaneous binding of multiple SlyD molecules.

Please note that k_{tc}^{app} is a force-dependent linear combination of the trans-cis isomerization in the native and unfolded states.

9.1 EFFECT OF SLYD ON PASSIVE-MODE EXPERIMENTS

In a next set of experiments, we repeated the passive-mode measurements on FLNa20 reported in Chapter 8. The only difference was adding varying concentrations of SlyD to the measurement buffer right before starting the experiment, as done for the competition experiments described in Chapter 6. Figure 12 shows a comparison between two passive-mode traces taken under similar conditions, but one without (upper) and the other with 7.5 µM of SlyD (lower) added into the measuring buffer. Please note that the time scaling is the

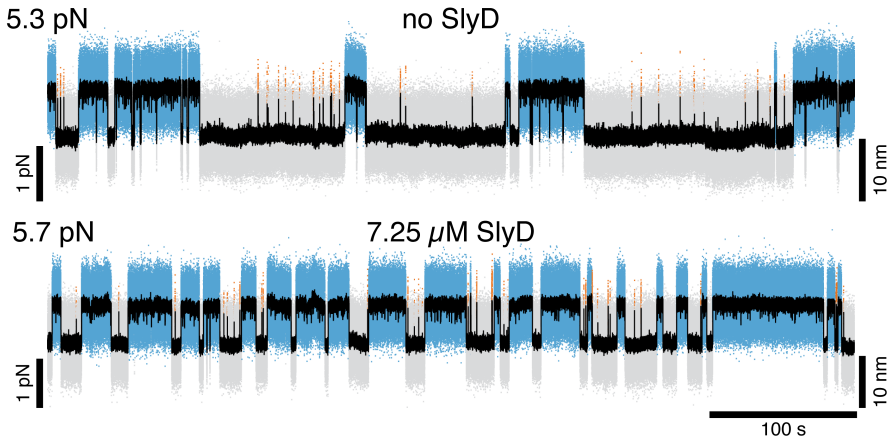

Figure 43: SlyD action on passive-mode experiments. Two long passive-mode experiments without (upper) and in the presence of SlyD (lower) taken at similar biasing forces. Both traces have the same time scaling.

same for both traces and that both traces were taken at a similar force bias. In the no-SlyD case, the mainly folded *cis* dwells are interrupted by extended *trans* periods, where the unfolded state dominates. Addition of SlyD leads to a drastic reduction of *trans* lifetimes, which

again causes an increase in the switching rate between blue (N_{cis}) and grey (mainly U_{trans}) dwells, and a population shift towards the folded state. At the same time, the dwell lengths of the native *cis* state seem to be unaffected. A comparison of the folded $((N_{cis}+N_{trans})/(N_{cis}+N_{trans}+U_{cis}+U_{trans}))$ and unfolded $(U_{cis}+U_{trans})/(N_{cis}+N_{trans}+U_{cis}+U_{trans}))$ populations is given in Figure 44, showing a clear shift of around 2 pN to higher forces for the 7.5 µM-SlyD experiment. This corresponds to a stabilization of about $2\,k_B\,T$. For this comparative analysis, we did not kinetically separate the folded states but only distinguished between folded or unfolded, which can be clearly identified using our HMM analysis. The shift to higher forces suggests that SlyD is not only acting as an enzyme (only affecting kinetics), but rather shifts the whole equilibrium. This can be caused by SlyD binding to the native *cis* state. Interestingly, Löw et al. reported that they

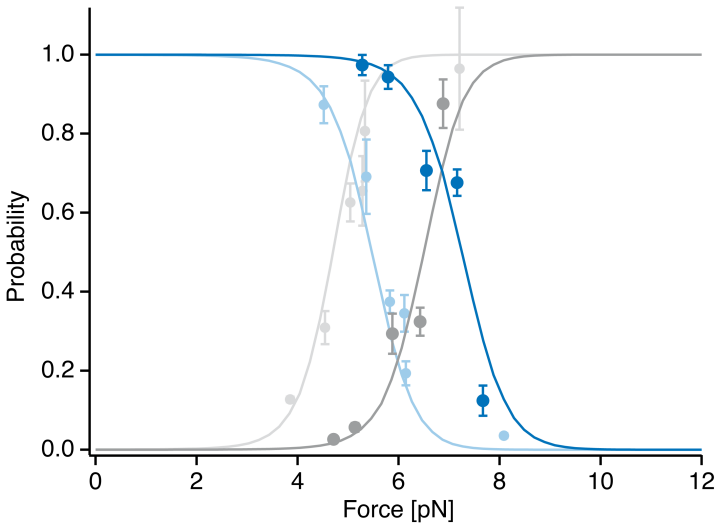

Figure 44: SlyD shifts folding probability of FLNa20. The blue and grey data points correspond to the total folded and unfolded state of FLNa20 in the presence of 7.5 µM SlyD. As a comparison also the corresponding no-SlyD data is shown in light colors. Solid lines are fits of Equation 12 to the data.

were able to co-crystalize *Thermus thermophilus* SlyD together with a tetrapetide bound to the isomerase domain [69]. The tetrapeptide was the standard substrate for the peptide-based prolyl isomerase assay and the prolyl peptide bond in the bound substrate was found to be in the *cis* conformation. On the other hand, binding to the N_{cis} state should also result in longer folded *cis* dwell times.

9.2 ISOMERIZATION KINETICS IN THE PRESENCE OF SLYD

We also tried to access the isomerization kinetics in our passive-mode experiments. One major concern regarding these experiments is the involved kinetic separation described in Section 5.8.1. There, we use

the folded dwell time length to discriminate between *cis* and *trans* state. Because the not catalyzed isomerization is slow, we attributed all unfolded dwell times between two length switches of the folded dwell times to the corresponding isomerization state. As reported, SlyD binds the unfolded protein and accelerates isomerization dramatically [128]. Based on the rates published by Zoldak et al., SlyD exhibits a binding rate of $174\,s^{-1}$ at 7.25 µM and dissociates with $25\,s^{-1}$. Combined with catalyzed isomerization kinetics on the order of $100\,s^{-1}$, a catalyzed back and forth isomerization would happen on the order of 100 ms. Compared to unfolded dwell times, which are on the order of 2 s around 5 pN, this implicates that we miss a non-negligible part of isomerization events while FLNa20 is unfolded. The

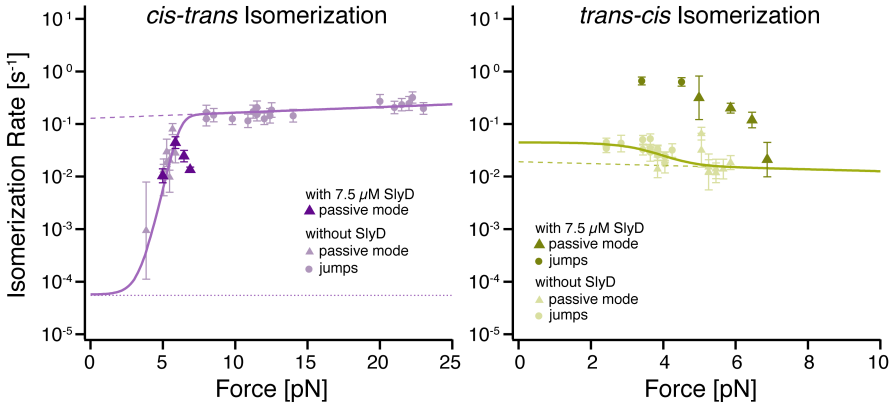

Figure 45: Isomerization kinetics of FLNa20 in the presence of 7.25 µM SlyD obtained from passive-mode experiments for the *cis-trans* (left) and *trans-cis* reaction (right). As a comparison WT data (see Figure 40) without SlyD is given in light colors along with the corresponding fits. For the *trans-cis* isomerization we included also jump experiments (circles).

force-dependent result is given in Figure 45 for the *cis*-to-*trans* (left) and the *trans*-to-*cis* (right) reaction. The uncatalyzed results along with the corresponding fits from Chapter 8 are given in light colors for easy comparison. Two jump experiments were added to the *trans-cis* plot (circles).

As already observed for the jump experiments, the *trans-cis* isomerization rate is accelerated in comparison to the WT data. At forces above 4 pN this effect decreases. The decrease lies in the force region where the protein shifts from mainly folded to predominately unfolded, i.e., more and more time is spent in the unfolded state. This leads to missed isomerization events and an underestimated *trans-cis* isomerization rate.

For the *cis-trans* isomerization (left), the first two points overlay with the WT data. The following points show again strong force-dependent decreases due to missed events. Based on the *trans-cis* results, already the first two points of the *cis-trans* isomerization rate

are affected by missed events. Therefore, the underlying isomerization rate should be accelerated compared to the WT data, as expected from an ideal enzyme that catalyzes both isomerization reactions.

9.3 FOLDING KINETICS IN THE PRESENCE OF SLYD

The issue of missed isomerization events also affects the correct determination of folding and unfolding kinetics of FLNa20 in the presence of SlyD in that the unfolded dwells are not correctly assigned to the right isomerization state. In addition to the passive-mode experiments, we used again the jump assay (Section 5.8.2) to extend the accessible force range and speed up measurement kinetics. The com-

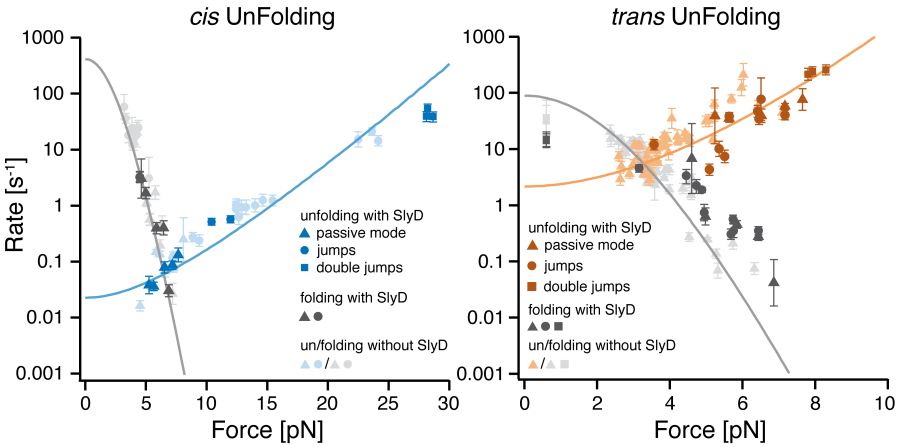

Figure 46: Passive-mode unfolding and folding kinetics of FLNa20 in the presence of 7.25 µM SlyD. WT data without SlyD are given in light colors.

bined kinetic folding and unfolding results in the presence of 7.25 µM SlyD are given in Figure 46 for the *cis* (left) and *trans* (right) states, respectively. As a comparison, the WT data without SlyD from Chapter 8 is again plotted in light colors along with the WT fits (solid lines). In addition to passive-mode and jump data, we also show some preliminary double-jump results. The underlying experiments are presented in the outlook of Section 9.5. The *cis* folding seems to be unchanged by the presence of SlyD and also the unfolding rates superimpose well with the WT data. In case of *trans* folding and unfolding, a slight shift to higher forces can be observed. Because *trans* and *cis* foldings are quite similar, the *cis*/*trans* mis-assignment due to missed events results in a surprisingly small effect. Nevertheless, we cannot draw exact conclusions based on these results, especially in regard to a potentially altered folding behavior caused by SlyD blocking the protein in the unfolded *cis* state, as it was observed by Zoldak et al. [128]. They reported a decelerated folding of ribonuclease T1 in the presence of more than 0.5 µM SlyD.

9.4 EXTENDED KINETIC MODEL AND MONTE-CARLO SIMULATIONS WITH SLYD

According to Scholz et al., SlyD binds only to the unfolded polypeptide chain with high affinity [101]. Based on this, we can expand the kinetic model presented in Figure 37A with two unfolded SlyD-bound states as shown in Figure 47. Zoldak et al. further reported that SlyD binds with $24 \times 10^6\,\mathrm{M}^{-1}\,\mathrm{s}^{-1}$ to the unfolded protein RCM-T1 and unbinds with $25\,\mathrm{s}^{-1}$ [128]. Numerical simulations of the folding

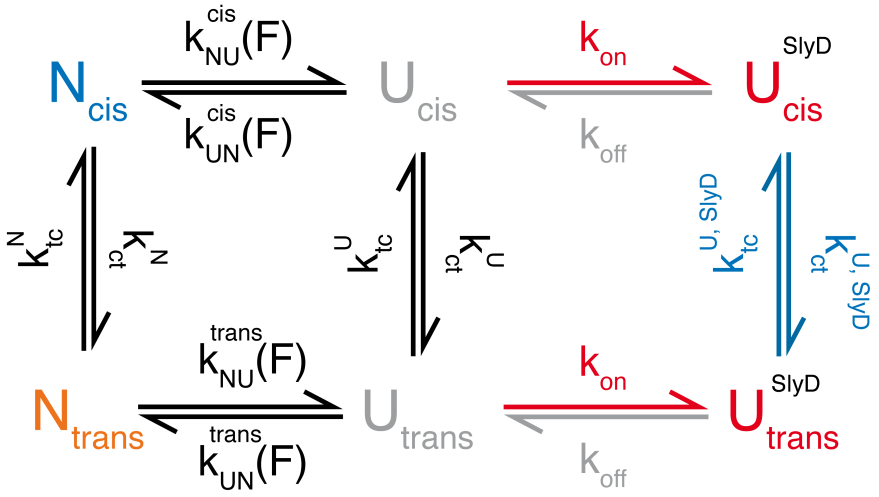

Figure 47: Kinetic model of FLNa20 folding in the presence of SlyD.

kinetics represented their data best with an assumed catalyzed *cis-trans* isomerization rate of $100\,\mathrm{s}^{-1}$ and a reverse rate of $16\,\mathrm{s}^{-1}$. Now, we can use the expanded model, together with the kinetic experimental results of Chapter 8 and the values reported by Zoldak et al., to simulate our passive-mode experiments at constant force bias. For details regarding the kinetic Monte-Carlo simulation see Section B.4.

A comparison of a measured and a simulated passive-mode trace taken at a force bias of 5.7 pN in the presence of 7.25 µM SlyD is given in Figure 48A and Figure 48B, respectively. The overall length and distribution of dwell times of both the measured and simulated traces are in excellent agreement, which validates the simulation as well as the proposed model. A zoom into the green marked region is given for the measured and simulated traces. The dark and light grey lines above the two zooms denote the isomerization state. For the measured trace, the assignment was done following the aforementioned method given in Section 5.8.1. In case of the simulation, the always accessible, correct isomerization state is given. Interestingly, this shows a fast switching between *cis* and *trans* while the molecule dwells in unfolded state. This fast isomerization kinetic is clearly visible in the second zoom of the simulated trace (lowest trace in Figure 48B).

In conclusion, the simulation shows that we have a correct assignment of the isomerization state for the folded protein, while we get drastic underestimated isomerization kinetics for the unfolded molecule.

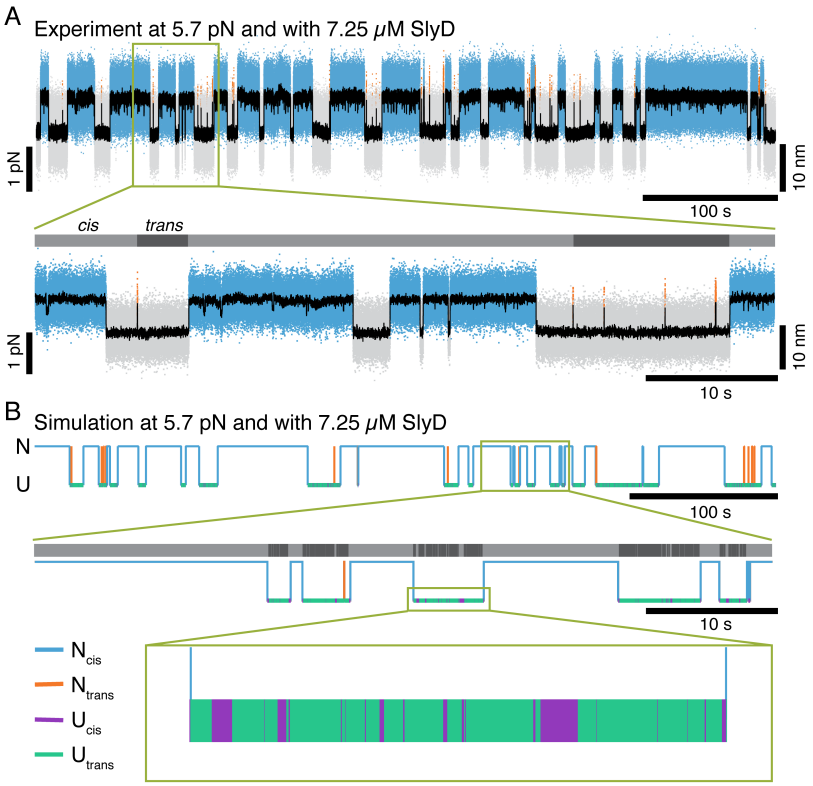

Figure 48: Comparison of a passive-mode trace taken at high SlyD concentration with a corresponding Monte-Carlo simulation. (A) Passive-mode trace taken at a biasing force of 5.7 pN and with 7.25 µM SlyD. (Upper) Full trace as given in Figure 43. (Lower) Zoom into a representative region with *cis* and *trans* folded dwells. The isomerization state assignment is given by the light and dark grey line above the zoom. (B) Monte-Carlo simulation of a passive-mode experiment taken at the same conditions as (A). (Upper) Full-length 500 s-trace with color-coding for N_{cis}, U_{cis}, N_{trans} and U_{trans}. The SlyD-bound states were lumped into the unfolded states. (Middle) Zoom into the green marked region of the full-length trace. The exact isomerization state is given above the zoom showing a high frequency switching between *cis* and *trans* while the protein is unfolded. This is clearly visible in a second zoom into an unfolded dwell (lower trace).

9.5 DISCUSSION

We could show that FLNa20 *cis/trans* switching is accelerated in the presence of isomerases. It is important to note that this holds for different classes of isomerases and different organisms. In fact, the hu-

man filamin domain studied here showed increased *trans-cis* rates in the presence of the human cyclophilin CypA or the bacterial FKBP SlyD. Further, we could block the catalytic activity of CypA by adding its inhibitor cyclosporin A. This emphasizes the generality of the investigated mechanisms.

Because of the issue of missed isomerization events at higher forces, where the protein is predominately unfolded, only the *trans-cis* isomerization could be measured with enough time resolution in jump experiments. As a control, passive-mode experiments were reproduced in Monte-Carlo simulations based on a proposed kinetic model of SlyD-dependent FLNa20 folding. The simulations showed a high switching kinetic for the unfolded protein leading to drastically underestimated isomerization kinetics when applying our *cis/trans* separation method.

For SlyD, we did a titration series of jump experiments with various concentrations spanning four orders of magnitude. The acceleration of the *trans-cis* isomerization could be modeled with a Langmuir isotherm of a simple two state binding model yielding a K_D value of 3.3 µM, which is in good agreement with findings of Zoldak et al. [128]. They reported a K_D of 0.5 µM for SlyD interacting with a permanently unfolded variant of RNase T1 (RCM-T1). Interestingly, high intracellular concentrations in the range of 5 to 10 µM have been found for cyclophilins and FKBPs [1, 95, 5]. The SlyD-catalyzed *trans-cis* isomerization rate was determined to $16\,s^{-1}$ in numerical simulatons by Zoldak et al.. In contrast, the apparent *trans-cis* rate measured in our jump assay is about $1\,s^{-1}$. However, one has to keep in mind that we do not directly measure the catalyzed isomerization $k_{tc}^{U,\,SlyD}$. Instead, $k_{tc}^{app,\,SlyD}$ is an apparent rate composed of a SlyD binding event followed by an *trans-cis* isomerization step, SlyD dissociation and a final *cis* folding of FLNa20. Unfortunately, all steps have relevant back-reaction rates. When we assume that the catalyzed isomerization is in equilibrium, we can estimate $k_{tc}^{app,\,SlyD}$ for a unidirectional reaction as follows

$$k_{tc}^{app,\,SlyD} \approx \left(\frac{1}{P_U^{trans} \cdot k_{on} \cdot [SlyD]} + \frac{1}{P_{cis}^{SlyD} \cdot k_{off}} \right)^{-1} . \tag{31}$$

With the reported rate constants of Zoldak et al., we get $4\,s^{-1}$, which is in good agreement with out measured value of $1\,s^{-1}$. Considering that we did not include the back reactions of SlyD binding/unbinding, an overestimation of $k_{tc}^{app,\,SlyD}$ is actually expected. Because the reported on-rate of $24 \times 10^6\,M^{-1}\,s^{-1}$ is only valid for binding to the unfolded protein, we corrected it in the calculation by the fraction of time FLNa20 spent in the unfolded *trans* state ($P_U^{trans} \approx 0.5$ at forces applied during our jump assay). Further, we omitted the *cis* folding rate because it is on a much faster timescale (about $100\,s^{-1}$).

In conclusion, the good agreement between our measured value and the estimate of $k_{tc}^{app,\,SlyD}$ based on the values of Zoldak et al. shows that $k_{tc}^{app,\,SlyD}$ is indeed governed by SlyD binding and unbinding. This again supports the Langmuir binding model (Section 9.0.1) used to fit the jump-assay data in Figure 42.

9.6 OUTLOOK

One major goal of future measurements is the increase of time resolution in order to avoid missed isomerization events. Because we are limited by the intrinsic folding rate of FLNa20, this can be achieved by extending the jump assays. A jump to even lower forces, where FLNa20 folds faster, will further increase the time resolution. However, this is limited by the maximal folding rate at zero load. This means that in theory we would get the best time resolution at zero load. On the other hand, we would have no length signal in this force regime. As a compromise, we can use a double-jump protocol where the protein is cycled between three force biases: one at zero load and the other two at a medium force (6 pN) and at a high force (30 pN). The zero-load level assures the fastest refolding rate. The folding state is tested at the mid-level, where *cis* and *trans* native states can be discriminated according to their different lifetimes. Finally, fast unfolding from the stable *cis* native state is achieved by jumping to the high force level to speed up the whole experiment.

Because the folding and unfolding process can be described as a an over-damped diffusion process in a potential [8], which results in a memoryless process, the jump dwells can be much shorter than a typical folding dwell time. This ensures a high time resolution for the refolding at zero load. Notably, the jump dwell length is only limited by the bead relaxation, which allows jump dwells down to 1 ms. First experiments with this jump protocol are quite promising and unfolding and folding rates based on those experiments were already included in Figure 46.

A completely different approach, which is being developed in our lab, is based on the combination of single-molecule force spectroscopy and single-molecule fluorescence. By adding fluorescently labeled SlyD into our optical trap experiments in combination with a confocal fluorescence detection at the protein position, we could directly measure the binding of SlyD to FLNa20. With such an approach we could answer the following open questions.

- Does SlyD bind only to the unfolded or also to the folded state?
- How many SlyD molecules bind at the same time?
- Is SlyD dissociation affected by force?

- How often does SlyD bind in jump experiments without catalyzing a *cis* folding?
- Is SlyD binding slowing down folding?

The expanded kinetic model shown in Figure 47 together with the reported rate constants of Zoldak et al. was used to create a transition rate matrix for a kinetic Montecarlo simulation (see Section B.4). With these simulations we could reproduce our passive-mode experiments and confirmed the issue of missed isomerization events. It can also be used to simulate the jump experiments in order to access the rate constants hidden in $k_{tc}^{app,\,SlyD}$.

The combination of faster jumps, single-molecule fluorescence detection and further simulations would give us a better time resolution in the isomerization domain together with a direct measurement of SlyD binding to FLNa20 in dependence of folding and force. These experiments and accompanying simulations would constitute a promising tool for studying in great detail the action of a single enzyme on a force loaded substrate. This should enable us not only to verify the proposed kinetic model, but also to directly measure all microscopic rate constants.

9.7 SUMMARY

In this chapter, I described experiments which studied the isomerization dependent folding of FLNa20 in the presence of peptidyl-prolyl *cis/trans* isomerases. Jump experiments showed a concentration dependent acceleration of the *trans*-to-*cis* isomerization for isomerases originating from different organisms and exhibiting totally different structures. This emphasizes the generality of the studied mechanism. In case of human CypA, the catalytic effect was completely blocked upon addition of its inhibitor cyclosporin. For the bacterial SlyD, we observed a higher catalytic activity. In our single-molecule measurements the acceleration is governed by binding and unbinding of SlyD to and from the stretched substrate. This was quantified by fitting a Langmuir binding mode, which assumes only one binding site. The resulting K_D and apparent rate $k_{tc}^{app,\,SlyD}$ are in good agreement with literature values supporting the validity of our experimental approach.

Passive-mode experiments in the presence of SlyD reproduced an increased *trans-cis* isomerization rate constant, but turned out to be affected by missed isomerization events while FLNa20 dwells in the unfolded state. This leads to a force-dependent underestimation of the transition rates. Surprisingly, force-dependent state probabilities of the passive-mode experiments showed a significant shift to higher forces compared to the no-SlyD experiments, which could indicate a SlyD-binding to the native *cis* state. However, this was not observed

in the extracted folding and unfolding rates, which again depend on the inaccurate kinetic separation of *cis* and *trans* dwells, due to missed events.

In conclusion, the experiments presented here demonstrate how mechanical single-molecule experiments can be used as a powerful tool to investigate the molecular action of enzymes in great detail. The thereby discovered molecular mechanisms are necessary in order to understand more complex processes *in vivo*.

Part IV

APPENDIX

A

SUPPLEMENTARY EXPERIMENTS ON FILMAIN

In this appendix chapter, I show supplementary results concerning filamin. Some were done as controls (e.g. the FLNa20 deletion mutant) for the experiments presented in Part III, others were smaller side projects that were stopped because of limited time (e.g. filamin domain 18 and 19 experiments).

A.1 HUNTING THE MINIMAL FOLDING PART OF DOMAIN 20

During the investigations of Chapter 7, we pose the question whether the single domain 20 fully folds including the A-strand, which is detached from domain 20 in the two-domain construct 20-21. Already in the constant-velocity experiments done with FLNa20-21, we found no difference in regard of the unfolding contour length change of domain 20 in presence or absence of a folded domain 21. Additionally, we observed the same length increase for the single domain construct FLNa20. This means, that we never observe an A-strand binding to domain 20. Either, it really never binds the domain body, or it already detaches at low forces where we have not enough length resolution. A next open question is the structural cause of the pre-

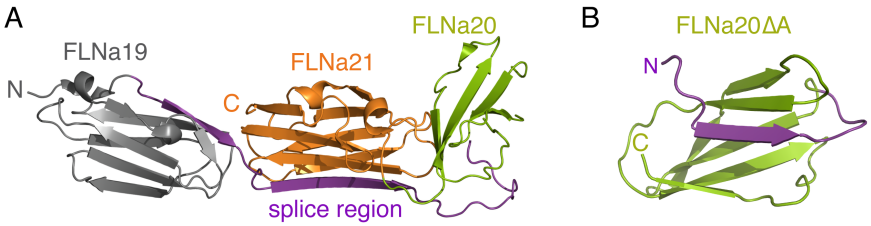

Figure 49: Splicing can produce deletions in the force sensing region of filamin. (A) Structure of domains 19 to 21 of human filamin A. By splicing the purple colored part of the protein can be deleted. The splicing region starts at the last β-strand of FLNa19 and stops after the second β-strand of FLNa20. (B) Fully resolved structure of domain 20 lacking the A-strand (FLNa20ΔA).

flipping state, which we observed in the native *cis* state (see arrow in Figure 36). Averaging over several unfolding transitions revealed no short-lived intermediate. We therefore categorized the pre-flipping as an off-pathway intermediate and lumped it into the native *cis* dwell times during further analysis. However, we assumed that the flip-

ping was caused by a partial unfolding attempt starting from the N-terminus. A closer look also revealed this kind of intermediate in the shorter lived *trans* native states. To test this hypothesis, we produced a deletion mutant where the A and B strands were missing. Interestingly, a spliced variant of filamin was reported which lacked the residues 2140 to 2171 in domains 19 and 20. This part is colored purple in the three domain crystal structure shown in Figure 49A. Because in this structure a part of domain 20 is not fully resolved, I also show a completely resolved structure of domain 20 lacking the A-strand in Figure 49B (personal communication, Jari Ylänne, 2013). This structure shows that the B-strand of domain 20 is part of the spliced deletion. For our deletion mutant, we chose the same boundaries as in the natural splicing variant. Figure 50 shows a comparison

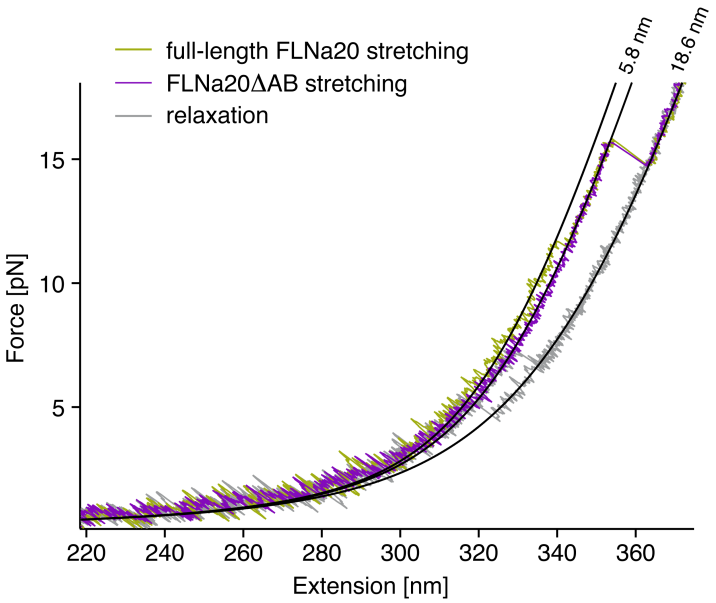

Figure 50: Stretch-and-relax cycle of deletion mutant (purple) and WT (green) FLNa20. Relaxation traces are shown in grey. The black lines are WLC models fitted to the stretching traces.

of two sample constant-velocity traces done on the full length (green extension, grey relaxation trace) and on the shortened FLNa20ΔAB mutant (purple extension, grey relaxation trace). Both traces overlay perfectly and have an identical main unfolding length, which is in excellent agreement with the reported value given in Table 1. A closer look at the full-length trace reveals a small unfolding step at around 11 pN with a contour length increase of 5.8 nm. This perfectly matches the estimated length increase associated with the B-strand unfolding of domain 20 ($\Delta L = 6.2$ nm). In contrast to the equilibrium experiments done in passive mode, the non-equilibrium constant-velocity experiments favor an on-pathway unfolding of the B-strand. A sample passive-mode trace with the deletion mutant of domain 20 is given in Figure 51. It shows the same bi-modal stability as for the

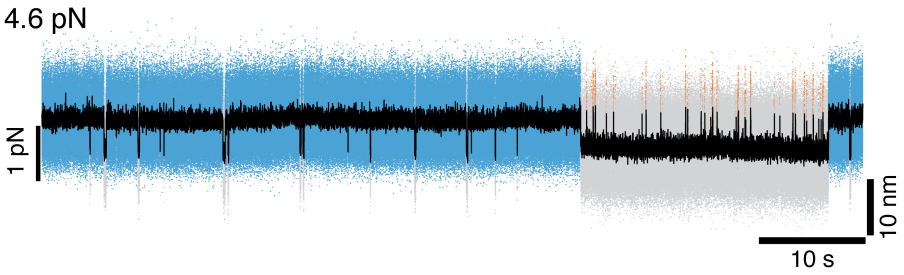

Figure 51: Passive-mode trace of FLNa20ΔAB lacking the first two β-strands.

full-length construct, but lacks the short lived off-pathway intermediate. This supports the structural interpretation of the intermediate observed in the complete domain 20.

SPLICING OF FILAMIN

For protein production, DNA is first transcribed into messenger RNA, which then is translated into the protein. Between transcription and translation, the pre-messenger RNA can undergo several modifications like splicing, capping or tailing, resulting in the matured messenger RNA. During splicing the non-coding introns are removed and the coding exons joined [93]. For many eukaryotic introns, splicing is done in a series of reactions which are catalyzed by the spliceosome, a complex of small nuclear ribonucleoproteins, but there are also self-splicing introns. In the case of alternative splicing the exon composition of the same pre-RNA can vary, thus creating a range of unique proteins. For filamin the purple colored region shown in Figure 49A and Figure 49B can be deleted by alternative splicing. This would abolish the autoinhibition mechanism leading to an always active receptor binding site. The experiments with the deletion mutant FLNa20ΔAB lacking the first two β-strands support the hypothesis that the spliced filamin variant is folded despite the deletion. Therefore, splicing would constitute an additional regulation mechanism, which can avoid the force sensing of FLNa20-21. Finally, domain 19 is lacking the last β-strand in the spliced filamin variant. Whether this affects the folding stability of domain 19 remains unsettled.

A.2 FILAMIN DOMAINS 18-19

In solution structures, the domains 18-19 of human filamin A show a similar structure as domains 20-21 (pdbID: 2K7Q). For comparison and in order to test the generality of the complex behavior of FLNa20-21, a similar construct was prepared with domains 18-19. Only a few preliminary experiments were done on this construct. The results are summarized in Figure 52 and Figure 53. As expected, the two-domain construct FLNa18-19 exhibits a similar unfolding pattern as FLNa20-

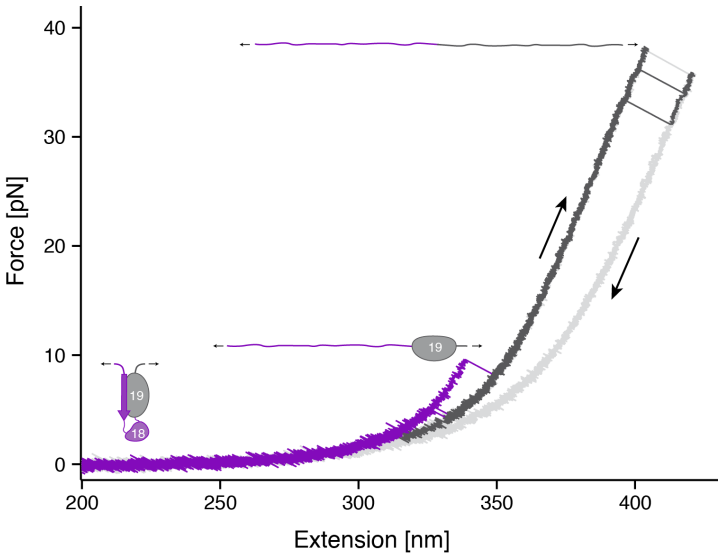

Figure 52: Stretch-and-relax cycles of FLNa18-19. Overlay of 3 stretch-and-relax cycles exhibiting an unfolding of both domains. The region of the stretching trace until unfolding of domain 18 is colored in purple followed by a dark grey coloring. The relaxation traces are colored in light grey. Similar to FLNa20-21 domain 18 unfolds already at low forces below 10 pN, while domain 19 is much more stable and unfolds at forces above 30 pN.

21 (see Figure 52). First, the less stable domain 18 unfolds at forces around 10 pN followed the unfolding of domain 19 at forces above 30 pN. While the typical Ig-like domains 19 and 21 exhibit a similar stability, domain 18 is even more labile compared to the corresponding domain 20.

This is also reflected in passive-mode experiments (see Figure 53). As already mentioned in Chapter 8, domain 18 exhibits the same highly conserved native *cis* proline at the beginning of the last β-strand. This causes again a bi-modal stability distribution, which is clearly visible in the drastically shorter dwell times of the grey colored folded state dwells (probably N_{trans}), as compared to the purple colored folded state dwells (probably N_{cis}).

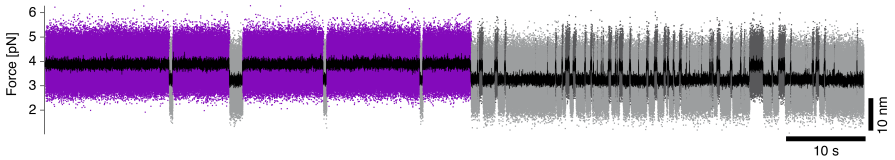

Figure 53: Passive-mode trace of FLNa18-19. Domain 18 exhibits a bi-modal stability similar to FLNa20. A switch from the stable presumably *cis* form (N_{cis} colored in purple) into the unstable *trans* form (N_{trans} colored in dark grey) happens in the middle of the trace.

B

MATERIAL AND METHODS

B.1 MOLECULAR CLONING

All protein constructs were inserted between two ubiquitin domains with terminal cysteines using molecular cloning techniques and expressed in *Escherichia coli*. The ubiquitins serve as spacer-molecules to prevent direct reaction of the terminal cysteines later used for DNA-handle coupling. Because ubiquitin domains are mechanically much more stable than Ig-like domains [98], they do not unfold at our exerted force range and thus do not interfere during the single-molecule mechanical measurements. To study the binding site of domain 21 of human filamin A, the corresponding 13-15 amino acid long binding regions of GPIbα, Migfilin and ITβ7 were tethered to the N-terminus of domain 21 via a flexible 6 amino acid glycine-serine-linker. The resulting amino acid sequences are the following.

B.1.1 *Sequences of investigated constructs*

B.1.1.1 *Tethered-peptide constructs*

GPIBα-FLNA21. MACKMQIFVKTLTGKTITLEVEPSDTIENVKAKI
QDKEGIPPDQQRLIFAGKQLEDGRTLSDYNIQKESTLHLVLR
LRGGELGGSGG**PTFRSSLFLWVRP**GGSGGSGPLGEGGAHK
VRAGGPGLERAEAGVPAEFSIWTREAGAGGLAIAVEGPSKA
EISFEDRKDGSCGVAYVVQEPGDYEVSVKFNEEHIPDSPFVV
PVASPSSGGSGGTMQIFVKTLTGKTITLEVEPSDTIENVKAKI
QDKEGIPPDQQRLIFAGKQLEDGRTLSDYNIQKESTLHLVLR
LRGGKCLEHHHHHH.

MIGFILIN-FLNA21. MACKMQIFVKTLTGKTITLEVEPSDTIENVKA
KIQDKEGIPPDQQRLIFAGKQLEDGRTLSDYNIQKESTLHLV
LRLRGGELGGSGG**PEKRVASSVFITLAP**GGSGGSGPLGEGG
AHKVRAGGPGLERAEAGVPAEFSIWTREAGAGGLAIAVEG
PSKAEISFEDRKDGSCGVAYVVQEPGDYEVSVKFNEEHIPDS
PFVVPVASPSSGGSGGTMQIFVKTLTGKTITLEVEPSDTIENV
KAKIQDKEGIPPDQQRLIFAGKQLEDGRTLSDYNIQKESTLH
LVLRLRGGKCLEHHHHHH.

ITβ7-FLNA21. MACKMQIFVKTLTGKTITLEVEPSDTIENVKAKIQ
DKEGIPPDQQRLIFAGKQLEDGRTLSDYNIQKESTLHLVLRL
RGGELGGSGG**PLYKSAITTTINP**GGSGGSGPLGEGGAHKVR
AGGPGLERAEAGVPAEFSIWTREAGAGGLAIAVEGPSKAEIS
FEDRKDGSCGVAYVVQEPGDYEVSVKFNEEHIPDSPFVVPV

ASPSSGGSGGTMQIFVKTLTGKTITLEVEPSDTIENVKAKIQD
KEGIPPDQQRLIFAGKQLEDGRTLSDYNIQKESTLHLVLRLR
GGKCLEHHHHHH.

The bold characters denote the peptide binding regions, whereas the underlined sequence corresponds to domain 21 of human filamin A.

B.1.1.2 *Autoinhibition construct*

For investigation of the autoinhibition mechanism, the following amino acid sequence of domains 20 and 21 was used. To prevent further undesired disulfide bonds in the two-domain construct, one cysteine in domain 21 (`Cys2293`; all numbers are used as in the crystal structure; pdbID: `2J3S`), and two in domain 20 of human filamin A were mutated to serines (`Cys2160`, `Cys2199`). All point mutations are marked by bold red characters. The underlined sequence region corresponds to domain 20-21 of filamin.

FLNA20-21. MACKMQIFVKTLTGKTITLEVEPSDTIENVKAKIQDK
EGIPPDQQRLIFAGKQLEDGRTLSDYNIQKESTLHLVLRLRG
GELGGSGGSGEGRVKESITRRRRAPSVANVGSH**S**DLSLKIPEI
SIQDMTAQVTSPSGKTHEAEIVEGENHTY**S**IRFVPAEMGTHT
VSVKYKGQHVPGSPFQFTVGPLGEGGAHKVRAGGPGLERA
EAGVPAEFSIWTREAGAGGLAIAVEGPSKAEISFEDRKDGS**S**
GVAYVVQEPGDYEVSVKFNEEHIPDSPFVVPVASPSSGGSGG
TMQIFVKTLTGKTITLEVEPSDTIENVKAKIQDKEGIPPDQQR
LIFAGKQLEDGRTLSDYNIQKESTLHLVLRLRGGKCLEHHH
HHH.

B.1.1.3 *Proline constructs*

FLNA20-21 P2222G. MACKMQIFVKTLTGKTITLEVEPSDTIENVK
AKIQDKEGIPPDQQRLIFAGKQLEDGRTLSDYNIQKESTLHL
VLRLRGGELGGSGGSGEGRVKESITRRRRAPSVANVGSH**S**DL
SLKIPEISIQDMTAQVTSPSGKTHEAEIVEGENHTY**S**IRFVPAE
MGTHTVSVKYKGQHV**G**GSPFQFTVGPLGEGGAHKVRAGG
PGLERAEAGVPAEFSIWTREAGAGGLAIAVEGPSKAEISFED
RKDGS**S**GVAYVVQEPGDYEVSVKFNEEHIPDSPFVVPVASPS
SGGSGGTMQIFVKTLTGKTITLEVEPSDTIENVKAKIQDKEGI
PPDQQRLIFAGKQLEDGRTLSDYNIQKESTLHLVLRLRGGKC
LEHHHHHH.

FLNA20-21 P2225G. MACKMQIFVKTLTGKTITLEVEPSDTIENVK
AKIQDKEGIPPDQQRLIFAGKQLEDGRTLSDYNIQKESTLHL
VLRLRGGELGGSGGSGEGRVKESITRRRRAPSVANVGSH**S**DL
SLKIPEISIQDMTAQVTSPSGKTHEAEIVEGENHTY**S**IRFVPAE
MGTHTVSVKYKGQHVPGS**G**FQFTVGPLGEGGAHKVRAGG
PGLERAEAGVPAEFSIWTREAGAGGLAIAVEGPSKAEISFED

RKDGSSGVAYVVQEPGDYEVSVKFNEEHIPDSPFVVPVASPS
SGGSGGTMQIFVKTLTGKTITLEVEPSDTIENVKAKIQDKEGI
PPDQQRLIFAGKQLEDGRTLSDYNIQKESTLHLVLRLRGGKC
LEHHHHHH.

FLNA20-21 P2222G AND P2225G. MACKMQIFVKTLTGKTITLEV
EPSDTIENVKAKIQDKEGIPPDQQRLIFAGKQLEDGRTLSDY
NIQKESTLHLVLRLRGGELGGSGGSGEGRVKESITRRRRAPS
VANVGSHSDLSLKIPEISIQDMTAQVTSPSGKTHEAEIVEGE
NHTYSIRFVPAEMGTHTVSVKYKGQHVGGSGFQFTVGPLG
EGGAHKVRAGGPGLERAEAGVPAEFSIWTREAGAGGLAIA
VEGPSKAEISFEDRKDGSSGVAYVVQEPGDYEVSVKFNEEHI
PDSPFVVPVASPSSGGSGGTMQIFVKTLTGKTITLEVEPSDTIE
NVKAKIQDKEGIPPDQQRLIFAGKQLEDGRTLSDYNIQKEST
LHLVLRLRGGKCLEHHHHHH.

B.1.1.4 *Single domain constructs*

In order to distinguish the force signals of the individual domains and for a thorough investigation of the proline dependent folding of FLNa20, the following single-domain construct was designed and produced.

FLNA20. MACKMHPFVKTLTGETITLEVEPSDTIENVKAKIQDKEG
IPPDQQRLIFAGKQLEDGRTLSDYNIQKESTLHLVLRLRGGE
LGGSGGSGEGRVKESITRRRRAPSVANVGSHSDLSLKIPEISI
QDMTAQVTSPSGKTHEAEIVEGENHTYSIRFVPAEMGTHTV
SVKYKGQHVPGSPFQFTVGPLGEGSGGSGGTMQIFVKTLTG
KTITLEVEPSDTIENVKAKIQDKEGIPPDQQRLIFAGKQLEDG
RTLSDYNIQKESTLHLVLRLRGGKCLEHHHHHH.

B.1.1.5 *Spliced deletion mutant of domain 20*

A deletion mutant of FLNa20 lacking the first two β-strands was produced in order to mimic filamin splicing.

FLNA20ΔAB. MACKMHPFVKTLTGETITLEVEPSDTIENVKAKIQD
KEGIPPDQQRLIFAGKQLEDGRTLSDYNIQKESTLHLVLRLR
GGELGGSGGSIQDMTAQVTSPSGKTHEAEIVEGENHTYSIRF
VPAEMGTHTVSVKYKGQHVPGSPFQFTVGPLGEGSGGSGG
TMQIFVKTLTGKTITLEVEPSDTIENVKAKIQDKEGIPPDQQR
LIFAGKQLEDGRTLSDYNIQKESTLHLVLRLRGGKCLEHHH
HHH.

B.1.1.6 *Double domain construct of domains 18-19*

The generality of the folding mechanism found for FLNa20-21 was tested with an analogous two-domain construct consisting of domains 18-19.

FLNA18-19. MACKMQIFVKTLTGKTITLEVEPSDTIENVKAKIQDK
EGIPPDQQRLIFAGKQLEDGRTLSDYNIQKESTLHLVLRLRG
GELGGSGGSGDDSMRMSHLKVGSAADIPINISETDLSLLTAT
VVPPSGREEPSLLKRLRNGHVGISFVPKETGEHLVHVKKNG
QHVASSPIPVVISQSEIGDASRVRVSGQGLHEGHTFEPAEFIID
TRDAGYGGLSLSIEGPSKVDINTEDLEDGTSRVTYSPTEPGN
YIINIKFADQHVPGSPFSVKVTGEGSGGSGGTMQIFVKTLTG
KTITLEVEPSDTIENVKAKIQDKEGIPPDQQRLIFAGKQLEDG
RTLSDYNIQKESTLHLVLRLRGGKCLEHHHHHH.

B.2 EXPERIMENTAL PROCEDURE

Protein-DNA constructs were mixed with silica beads (1 µm diameter, Bangs Laboratories, Inc.), which were previously covalently functionalized with anti-digoxigenin Fab fragments (Roche). These constructs were subsequently mixed with streptavidin coated silica beads (1 µm diameter, Bangs Laboratories, Inc.). Measurements were carried out at room temperature in PBS (10 mM phosphate buffer, 2.7 mM potassium chloride and 137 mM sodium chloride, pH 7.4, at 25 °C), with an added oxygen scavenger system (26 U/ml glucose oxidase, 17 000 U/ml catalase, 0.65 % glucose). The protein-DNA coupled beads were introduced into a flow cell consisting of a coverslip attached to a glass slide via Nescofilm (Bando Chemical Industries Ltd.) and pretreated with bovine serum albumin (Sigma-Aldrich Co.). Trapped beads were brought into close proximity to build a bead-DNA-protein dumbbell. Protein-DNA concentrations were adjusted to only sparsely cover the beads leading mainly to single tethered dumbbells. The trapping potentials were then separated with a constant velocity yielding force vs. extension traces or held at a constant separation to record force vs. time traces. When a dumbbell was successfully tested for single tether formation through stretch-and-relax cycles, further investigations of the reported equilibrium fluctuations followed at various constant trap positions. In the resulting force vs. time traces, the state population and dwell times were determined using HMM analysis.

B.3 BROWNIAN DYNAMICS SIMULATIONS

In order to test the state assignment based on the HMM analysis, we performed simulations of our equilibrium measurements and afterwards analyzed these with the same procedures used for the original measurements. Therefore, we simulated the thermal movement of both beads in their traps using Brownian Dynamics [74, 108]. Mimicking the experimental setup, the two beads were connected with a linker consisting of DNA, modeled by an eWLC (Equation 1), in series with a worm-like chain term (Equation 2). The contour length of the protein depended on the state (open/closed, Table 1), which was

determined for each time step using a Monte-Carlo generator. The transition probabilities used for the Monte-Carlo generator were calculated from the rates determined in the experiment (Table 2). During the simulation, the response of the two beads to the length change of the protein was calculated using Brownian Dynamics. The signal was treated as in the original experiments. Therefore, data points were taken with 100 kHz and subsequently sampled down to 20 kHz. After the simulation of a full trajectory, the difference signal of the two beads was calculated and analyzed using the HMM method. An example for such a simulated trace is shown in Figure 31D.

B.4 KINETIC MONTE-CARLO SIMULATIONS

The network of the proline dependent folding of FLNa20 as well as the extended network in the presence of SlyD was simulated using the four- and six-state Markov models shown in Figure 32 and Figure 47, respectively. First, the quadratic transition rate matrix was initialized with the zero-load rate constants (Table 4 and Table 5). The transition rate constants from the native states to the unfolded states and back under force were determined following the Berkemeier-Schlierf model (Section 5.6.2). The force-dependent isomerization rate constants were calculated from Equation 28 and Equation 29. In case of the six-state model with SlyD binding, a first oder binding model with $k_{on} = 24 \times 10^6\,M^{-1}\,s^{-1}$ and $k_{off} = 25\,s^{-1}$ was used. Using this transition rate matrix, trajectories can be generated as follows: at each simulation step, the dwell time in the current state i was drawn from an exponential distribution with the lifetime $\tau = \left(\sum_{j\neq i} k_{ij}\right)^{-1}$. The subsequent state l was chosen with probabilities $P_l = k_{il} \cdot \tau$. The resulting trajectories were analyzed in the same way as the HMM assigned trajectories of the passive-mode experiments. A sample trace of such a simulation is given in Figure 48B.

B.5 DRIFT CORRECTION

For a successful dwell time analysis, the baseline of long time traces (typically 100 s) at low forces (2 to 4 pN) has to be constant, as shown in Figure 28B. Therefore, low frequency drift was corrected for by subtracting a manually adjusted spline.

BIBLIOGRAPHY

[1] R P Agarwal, G A Threatte, and R A McPherson. Temperature-dependent binding of cyclosporine to an erythrocyte protein. *Clinical chemistry*, 1987. (Cited on page 89.)

[2] Peter C Anthony, Christian F Perez, Cuauhtémoc García-García, and Steven M Block. Folding energy landscape of the thiamine pyrophosphate riboswitch aptamer. *Proceedings Of The National Academy Of Sciences Of The United States Of America*, 109(5):1485–1489, January 2012. (Cited on page 23.)

[3] A Ashkin. Forces of a single-beam gradient laser trap on a dielectric sphere in the ray optics regime. *Biophysj*, 61(2):569–582, February 1992. (Cited on page 23.)

[4] A Ashkin and J M Dziedzic. Optical trapping and manipulation of viruses and bacteria. *Science (New York, NY)*, 235(4795):1517–1520, March 1987. (Cited on page 23.)

[5] Gail Baughman, Gregory J Wiederrecht, Fon Chang, Mary M Martin, and Suzanne Bourgeois. Tissue Distribution and Abundance of Human FKBP51, an FK506-Binding Protein That Can Mediate Calcineurin Inhibition. *Biochemical and biophysical research communications*, 232(2):437–443, March 1997. (Cited on page 89.)

[6] G I Bell. Models for the specific adhesion of cells to cells. *Science (New York, NY)*, 200(4342):618–627, May 1978. (Cited on page 35.)

[7] Morten Bertz, Matthias Wilmanns, and Matthias Rief. The titin-telethonin complex is a directed, superstable molecular bond in the muscle Z-disk. *Proceedings Of The National Academy Of Sciences Of The United States Of America*, 106(32):13307–133310, August 2009. (Cited on page 22.)

[8] Robert B Best and Gerhard Hummer. Coordinate-dependent diffusion in protein folding. *Proceedings Of The National Academy Of Sciences Of The United States Of America*, 107(3):1088–1093, January 2010. (Cited on pages 30 and 90.)

[9] J F Brandts, H R Halvorson, and M Brennan. Consideration of the Possibility that the slow step in protein denaturation reactions is due to cis-trans isomerism of proline residues. *Biochemistry*, 14(22):4953–4963, November 1975. (Cited on pages 4 and 11.)

[10] J F Brandts, M Brennan, and Lung-Nan Lin. Unfolding and refolding occur much faster for a proline-free proteins than for most proline-containing proteins. *Proceedings Of The National Academy Of Sciences Of The United States Of America*, 74(10):4178–4181, October 1977. (Cited on pages 4 and 11.)

[11] T Breuder, C S Hemenway, N R Movva, M E Cardenas, and J Heitman. Calcineurin is essential in cyclosporin A- and FK506-sensitive yeast strains. *Proceedings Of The National Academy Of Sciences Of The United States Of America*, 91(12):5372–5376, June 1994. (Cited on page 13.)

[12] C Bustamante, J F Marko, E D Siggia, and S Smith. Entropic elasticity of lambda-phage DNA. *Science (New York, NY)*, 265 (5178):1599–1600, September 1994. (Cited on page 31.)

[13] Ciro Cecconi, Elizabeth A Shank, Carlos Bustamante, and Susan Marqusee. Direct observation of the three-state folding of a single protein molecule. *Science (New York, NY)*, 309(5743): 2057–2060, September 2005. (Cited on pages 23, 26, 31, and 76.)

[14] J B Charbonnier, P Belin, M Moutiez, E A Stura, and E Quéméneur. On the role of the cis-proline residue in the active site of DsbA. *Protein science : a publication of the Protein Society*, 8(1):96–105, January 1999. (Cited on pages 4 and 12.)

[15] Hu Chen, Hongxia Fu, Xiaoying Zhu, Peiwen Cong, Fumihiko Nakamura, and Jie Yan. Improved high-force magnetic tweezers for stretching and refolding of proteins and short DNA. *Biophysical journal*, 100(2):517–523, January 2011. (Cited on page 60.)

[16] Hu Chen, Saranya Chandrasekar, Michael P Sheetz, Thomas P Stossel, Fumihiko Nakamura, and Jie Yan. Mechanical perturbation of filamin A immunoglobulin repeats 20-21 reveals potential non-equilibrium mechanochemical partner binding function. *Scientific reports*, 3:1642, April 2013. (Cited on page 78.)

[17] Jian Chen, Scott A Edwards, Frauke Gräter, and Carsten Baldauf. On the cis to trans isomerization of prolyl-peptide bonds under tension. *The journal of physical chemistry B*, 116(31):9346–9351, August 2012. (Cited on pages 75 and 77.)

[18] Ramu Chenna, Hideaki Sugawara, Tadashi Koike, Rodrigo Lopez, Toby J Gibson, Desmond G Higgins, and Julie D Thompson. Multiple sequence alignment with the Clustal series of programs. *Nucleic acids research*, 31(13):3497–3500, July 2003. (Cited on pages 29, 43, and 44.)

[19] Susan L Cranmer, Katrina J Ashworth, Yu Yao, Michael C Berndt, Zaverio M Ruggeri, Robert K Andrews, and Shaun P Jackson. High shear-dependent loss of membrane integrity and defective platelet adhesion following disruption of the GPIbα-filamin interaction. *Blood*, 117(9):2718–2727, March 2011. (Cited on pages 3, 8, 54, and 65.)

[20] Mitali Das, Sujay Subbayya Ithychanda, Jun Qin, and Edward F Plow. Migfilin and Filamin as Regulators of Integrin Activation in Endothelial Cells and Neutrophils. *PloS one*, 6(10):e26355, October 2011. (Cited on pages 47 and 54.)

[21] Iwijn De Vlaminck and Cees Dekker. Recent advances in magnetic tweezers. *Annual review of biophysics*, 41:453–472, 2012. (Cited on page 22.)

[22] Armando del Rio, Raul Perez-Jimenez, Ruchuan Liu, Pere Roca-Cusachs, Julio M Fernandez, and Michael P Sheetz. Stretching single talin rod molecules activates vinculin binding. *Science (New York, NY)*, 323(5914):638–641, January 2009. (Cited on page 64.)

[23] Hendrik Dietz and Matthias Rief. Exploring the energy landscape of GFP by single-molecule mechanical experiments. *Proceedings Of The National Academy Of Sciences Of The United States Of America*, 101(46):16192–16197, November 2004. (Cited on page 32.)

[24] Olivia du Roure, Alexandre Saez, Axel Buguin, Robert H Austin, Philippe Chavrier, Pascal Silberzan, Pascal Siberzan, and Benoit Ladoux. Force mapping in epithelial cell migration. *Proceedings Of The National Academy Of Sciences Of The United States Of America*, 102(7):2390–2395, February 2005. (Cited on page 21.)

[25] Olga Dudko, Gerhard Hummer, and Attila Szabo. Intrinsic Rates and Activation Free Energies from Single-Molecule Pulling Experiments. *Physical review letters*, 96(10):108101, March 2006. (Cited on page 28.)

[26] Barbara Eckert, Andreas Martin, Jochen Balbach, and Franz X Schmid. Prolyl isomerization as a molecular timer in phage infection. *Nature structural & molecular biology*, 12(7):619–623, July 2005. (Cited on pages 4, 11, and 12.)

[27] A J Ehrlicher, F Nakamura, J H Hartwig, D A Weitz, and T P Stossel. Mechanical strain in actin networks regulates FilGAP and integrin binding to filamin A. *Nature*, 478(7368):260–263, October 2011. (Cited on pages 10 and 65.)

[28] Phillip J Elms, John D Chodera, Carlos Bustamante, and Susan Marqusee. The molten globule state is unusually deformable under mechanical force. *Proceedings Of The National Academy Of Sciences Of The United States Of America*, 109(10):3796–3801, March 2012. (Cited on page 23.)

[29] Adam J Engler, Shamik Sen, H Lee Sweeney, and Dennis E Discher. Matrix elasticity directs stem cell lineage specification. *Cell*, 126(4):677–689, August 2006. (Cited on pages 3 and 21.)

[30] E Evans and K Ritchie. Dynamic strength of molecular adhesion bonds. *Biophysj*, 72(4):1541–1555, April 1997. (Cited on page 28.)

[31] J Friedman and I Weissman. Two cytoplasmic candidates for immunophilin action are revealed by affinity for a new cyclophilin: one in the presence and one in the absence of CsA. *Cell*, 66(4): 799–806, August 1991. (Cited on page 13.)

[32] S Furuike. Mechanical unfolding of single filamin A (ABP-280) molecules detected by atomic force microscopy. *FEBS letters*, 498(1):72–75, June 2001. (Cited on page 60.)

[33] J Christof M Gebhardt. *Energielandschaften einzelner Proteine gemessen mit der optischen Pinzette*. Dissertation, Technische Universität München, München, 2009. (Cited on page 25.)

[34] J Christof M Gebhardt, Thomas Bornschlögl, and Matthias Rief. Full distance-resolved folding energy landscape of one single protein molecule. *Proceedings Of The National Academy Of Sciences Of The United States Of America*, 107(5):2013–2018, February 2010. (Cited on pages 25, 26, and 35.)

[35] Scott Gehler, Massimiliano Baldassarre, Yatish Lad, Jennifer L Leight, Michele A Wozniak, Kristin M Riching, Kevin W Eliceiri, Valerie M Weaver, David A Calderwood, and Patricia J Keely. Filamin A-beta1 integrin complex tunes epithelial cell response to matrix tension. *Molecular biology of the cell*, 20(14):3224–3238, July 2009. (Cited on pages 3 and 7.)

[36] M Glogauer, P Arora, D Chou, P A Janmey, G P Downey, and C A McCulloch. The role of actin-binding protein 280 in integrin-dependent mechanoprotection. *The Journal of biological chemistry*, 273(3):1689–1698, January 1998. (Cited on pages 3 and 7.)

[37] Carsten Grashoff, Brenton D Hoffman, Michael D Brenner, Ruobo Zhou, Maddy Parsons, Michael T Yang, Mark A McLean, Stephen G Sligar, Christopher S Chen, Taekjip Ha, and Martin A

Schwartz. Measuring mechanical tension across vinculin reveals regulation of focal adhesion dynamics. *Nature*, 466(7303): 263–266, July 2010. (Cited on pages 21 and 64.)

[38] Christoph Grathwohl and Kurt Wüthrich. NMR studies of the rates of proline cis–trans isomerization in oligopeptides. *Biopolymers*, 20(12):2623–2633, 1981. (Cited on page 67.)

[39] William J Greenleaf, Michael T Woodside, Elio A Abbondanzieri, and Steven M Block. Passive all-optical force clamp for high-resolution laser trapping. *Physical review letters*, 95(20): 208102, November 2005. (Cited on page 28.)

[40] Tom A Hall. BioEdit: a user-friendly biological sequence alignment editor and analysis program for Windows 95/98/NT. 41: 95–98, 1999. (Cited on pages 29, 43, and 44.)

[41] Y Harada and T Asakura. Radiation forces on a dielectric sphere in the Rayleigh scattering regime. *Optics Communications*, 1996. (Cited on page 24.)

[42] Outi Heikkinen, Perttu Permi, Harri Koskela, Olli Carpén, Jari Ylänne, and Ilkka Kilpeläinen. Solution structure of the first immunoglobulin domain of human myotilin. *Journal of biomolecular NMR*, 44(2):107–112, June 2009. (Cited on pages 4 and 65.)

[43] Outi K Heikkinen, Salla Ruskamo, Peter V Konarev, Dmitri I Svergun, Tatu Iivanainen, Sami M Heikkinen, Perttu Permi, Harri Koskela, Ilkka Kilpeläinen, and Jari Ylänne. Atomic structures of two novel immunoglobulin-like domain pairs in the actin cross-linking protein filamin. *The Journal of biological chemistry*, 284(37):25450–25458, September 2009. (Cited on pages 7 and 64.)

[44] Armin Hoffmann and Michael T Woodside. Signal-pair correlation analysis of single-molecule trajectories. *Angewandte Chemie (International ed in English)*, 50(52):12643–12646, December 2011. (Cited on page 28.)

[45] Masahiko Hoshijima. Mechanical stress-strain sensors embedded in cardiac cytoskeleton: Z disk, titin, and associated structures. *American journal of physiology. Heart and circulatory physiology*, 290(4):H1313–25, April 2006. (Cited on page 3.)

[46] Josep M Huguet, Cristiano V Bizarro, Núria Forns, Steven B Smith, Carlos Bustamante, and Felix Ritort. Single-molecule derivation of salt dependent base-pair free energies in DNA. *Proceedings Of The National Academy Of Sciences Of The United States Of America*, 107(35):15431–15436, August 2010. (Cited on page 23.)

[47] Eric G Huizinga, Shizuko Tsuji, Roland A P Romijn, Marion E Schiphorst, Philip G de Groot, Jan J Sixma, and Piet Gros. Structures of glycoprotein Ibalpha and its complex with von Willebrand factor A1 domain. *Science (New York, NY)*, 297(5584):1176–1179, August 2002. (Cited on pages 3 and 7.)

[48] A Ikai and C Tanford. Kinetics of unfolding and refolding of proteins. I. Mathematical analysis. *Journal of molecular biology*, 73(2):145–163, January 1973. (Cited on page 76.)

[49] Sujay Subbayya Ithychanda and Jun Qin. Evidence for multisite ligand binding and stretching of filamin by integrin and migfilin. *Biochemistry*, 50(20):4229–4231, May 2011. (Cited on page 64.)

[50] Sujay Subbayya Ithychanda, Mitali Das, Yan-Qing Ma, Keyang Ding, Xiaoxia Wang, Sudhiranjan Gupta, Chuanyue Wu, Edward F Plow, and Jun Qin. Migfilin, a molecular switch in regulation of integrin activation. *The Journal of biological chemistry*, 284(7):4713–4722, February 2009. (Cited on pages 47 and 54.)

[51] Sujay Subbayya Ithychanda, Dennis Hsu, Hanhan Li, Linda Yan, David D Liu, Darwen Liu, Mitali Das, Edward F Plow, and Jun Qin. Identification and characterization of multiple similar ligand-binding repeats in filamin: implication on filamin-mediated receptor clustering and cross-talk. *The Journal of biological chemistry*, 284(50):35113–35121, December 2009. (Cited on pages 8, 55, and 65.)

[52] Bharat Jagannathan, Phillip J Elms, Carlos Bustamante, and Susan Marqusee. Direct observation of a force-induced switch in the anisotropic mechanical unfolding pathway of a protein. *Proceedings Of The National Academy Of Sciences Of The United States Of America*, 109(44):17820–17825, October 2012. (Cited on page 29.)

[53] Roman P Jakob and Franz X Schmid. Energetic coupling between native-state prolyl isomerization and conformational protein folding. *Journal of molecular biology*, 377(5):1560–1575, April 2008. (Cited on pages 4, 12, and 76.)

[54] Roman P Jakob and Franz X Schmid. Molecular determinants of a native-state prolyl isomerization. *Journal of molecular biology*, 387(4):1017–1031, April 2009. (Cited on page 76.)

[55] Guoying Jiang, Grégory Giannone, David R Critchley, Emiko Fukumoto, and Michael P Sheetz. Two-piconewton slip bond between fibronectin and the cytoskeleton depends on talin. *Nature*, 424(6946):334–337, July 2003. (Cited on page 64.)

[56] Pengju Jiang and Iain D Campbell. Integrin binding immunoglobulin type filamin domains have variable stability. *Biochemistry*, 47(42):11055–11061, October 2008. (Cited on pages 3 and 7.)

[57] Dana Kahra, Michael Kovermann, Christian Löw, Verena Hirschfeld, Caroline Haupt, Jochen Balbach, and Christian Gerhard Hübner. Conformational plasticity and dynamics in the generic protein folding catalyst SlyD unraveled by single-molecule FRET. *Journal of molecular biology*, 411(4):781–790, August 2011. (Cited on page 16.)

[58] Harini Kaluarachchi, Duncan E K Sutherland, Alex Young, Ingrid J Pickering, Martin J Stillman, and Deborah B Zamble. The Ni(II)-binding properties of the metallochaperone SlyD. *Journal of the American Chemical Society*, 131(51):18489–18500, December 2009. (Cited on page 14.)

[59] T Kiefhaber, H P Grunert, U Hahn, and F X Schmid. Replacement of a cis proline simplifies the mechanism of ribonuclease T1 folding. *Biochemistry*, 29(27):6475–6480, July 1990. (Cited on pages 4 and 12.)

[60] Tiila Kiema, Yatish Lad, Pengju Jiang, Camilla L Oxley, Massimiliano Baldassarre, Kate L Wegener, Iain D Campbell, Jari Ylänne, and David A Calderwood. The molecular basis of filamin binding to integrins and competition with talin. *Molecular cell*, 21(3):337–347, February 2006. (Cited on page 8.)

[61] Jongseong Kim, Cheng-Zhong Zhang, Xiaohui Zhang, and Timothy A Springer. A mechanically stabilized receptor-ligand flex-bond important in the vasculature. *Nature*, 466(7309):992–U123, 2010. (Cited on page 54.)

[62] Thomas A Knappe, Barbara Eckert, Peter Schaarschmidt, Christian Scholz, and Franz X Schmid. Insertion of a chaperone domain converts FKBP12 into a powerful catalyst of protein folding. *Journal of molecular biology*, 368(5):1458–1468, May 2007. (Cited on page 15.)

[63] Michael Kovermann, Robert Zierold, Caroline Haupt, Christian Löw, and Jochen Balbach. NMR relaxation unravels interdomain crosstalk of the two domain prolyl isomerase and chaperone SlyD. *Biochimica et biophysica acta*, 1814(7):873–881, July 2011. (Cited on page 16.)

[64] Michael Kovermann, Franz X Schmid, and Jochen Balbach. Molecular function of the prolyl cis/trans isomerase and metallochaperone SlyD. *Biological chemistry*, 394(8):965–975, August 2013. (Cited on pages 14 and 17.)

[65] Yatish Lad, Tiila Kiema, Pengju Jiang, Olli T Pentikäinen, Charlotte H Coles, Iain D Campbell, David A Calderwood, and Jari Ylänne. Structure of three tandem filamin domains reveals auto-inhibition of ligand binding. *The EMBO journal*, 26(17): 3993–4004, September 2007. (Cited on pages 4, 7, 10, 62, 65, 66, and 69.)

[66] Markita P Landry, Patrick M McCall, Zhi Qi, and Yann R Chemla. Characterization of photoactivated singlet oxygen damage in single-molecule optical trap experiments. *Biophysical journal*, 97(8):2128–2136, October 2009. (Cited on page 27.)

[67] J Liu, J D Farmer, W S Lane, J Friedman, I Weissman, and S L Schreiber. Calcineurin is a common target of cyclophilin-cyclosporin A and FKBP-FK506 complexes. *Cell*, 66(4):807–815, August 1991. (Cited on page 13.)

[68] Stephan Lorenzen, Björn Peters, Andrean Goede, Robert Preissner, and Cornelius Frömmel. Conservation of cis prolyl bonds in proteins during evolution. *Proteins*, 58(3):589–595, February 2005. (Cited on page 78.)

[69] Christian Löw, Piotr Neumann, Henning Tidow, Ulrich Weininger, Caroline Haupt, Beatrice Friedrich-Epler, Christian Scholz, Milton T Stubbs, and Jochen Balbach. Crystal structure determination and functional characterization of the metallochaperone SlyD from Thermus thermophilus. *Journal of molecular biology*, 398(3):375–390, May 2010. (Cited on pages 15 and 84.)

[70] Kun Ping Lu, Greg Finn, Tae Ho Lee, and Linda K Nicholson. Prolyl cis-trans isomerization as a molecular timer. *Nature Chemical Biology*, 3(10):619–629, October 2007. (Cited on pages 4, 11, 12, 13, and 81.)

[71] Sarah C R Lummis, Darren L Beene, Lori W Lee, Henry A Lester, R William Broadhurst, and Dennis A Dougherty. Cis-trans isomerization at a proline opens the pore of a neurotransmitter-gated ion channel. *Nature*, 438(7065):248–252, November 2005. (Cited on page 4.)

[72] S.C.R. Lummis, D.L. Beene, L.W. Lee, H.A. Lester, R.W. Broadhurst, and D.A. Dougherty. Cis–trans isomerization at a proline opens the pore of a neurotransmitter-gated ion channel. *Nature*, 438(7065):248–252, 2005. (Cited on page 11.)

[73] Christopher D Lynch, Nils C Gauthier, Nicolas Biais, Andre M Lazar, Pere Roca-Cusachs, Cheng-Han Yu, and Michael P Sheetz. Filamin depletion blocks endoplasmic spreading and

destabilizes force-bearing adhesions. *Molecular biology of the cell*, 22(8):1263–1273, 2011. (Cited on pages 3, 8, and 65.)

[74] M Manosas, J-D Wen, P T X Li, S B Smith, C Bustamante, I Tinoco, and F Ritort. Force unfolding kinetics of RNA using optical tweezers. II. Modeling experiments. *Biophysical journal*, 92(9):3010–3021, May 2007. (Cited on page 102.)

[75] Hai Yun Meng, Krista M Thomas, Aaron E Lee, and Neal J Zondlo. Effects of i and i+3 residue identity on cis-trans isomerism of the aromatic(i+1)-prolyl(i+2) amide bond: implications for type VI beta-turn formation. *Biopolymers*, 84(2):192–204, 2006. (Cited on page 78.)

[76] Jeffrey R Moffitt, Yann R Chemla, David Izhaky, and Carlos Bustamante. Differential detection of dual traps improves the spatial resolution of optical tweezers. *Proceedings Of The National Academy Of Sciences Of The United States Of America*, 103 (24):9006–9011, June 2006. (Cited on pages 25 and 76.)

[77] M Mücke and F X Schmid. Intact disulfide bonds decelerate the folding of ribonuclease T1. *Journal of molecular biology*, 239 (5):713–725, June 1994. (Cited on page 15.)

[78] M Mücke and F X Schmid. Folding mechanism of ribonuclease T1 in the absence of the disulfide bonds. *Biochemistry*, 33(48): 14608–14619, December 1994. (Cited on page 15.)

[79] Fumihiko Nakamura, Regina Pudas, Outi K Heikkinen, Perttu Permi, Ilkka Kilpeläinen, Adam D Munday, John H Hartwig, Thomas P Stossel, and Jari Ylänne. The structure of the GPIb-filamin A complex. *Blood*, 107(5):1925–1932, March 2006. (Cited on page 8.)

[80] Fumihiko Nakamura, Thomas P Stossel, and John H Hartwig. The filamins: organizers of cell structure and function. *Cell adhesion & migration*, 5(2):160–169, February 2011. (Cited on pages 3, 7, and 8.)

[81] Warwick S Nesbitt, Erik Westein, Francisco Javier Tovar-Lopez, Elham Tolouei, Arnan Mitchell, Jia Fu, Josie Carberry, Andreas Fouras, and Shaun P Jackson. A shear gradient-dependent platelet aggregation mechanism drives thrombus formation. *Nature medicine*, 15(6):665–673, June 2009. (Cited on pages 3 and 7.)

[82] T A Nieminen, VLY Loke, and A B Stilgoe. Optical tweezers computational toolbox. *Journal of Optics A: Pure and Applied Optics*, 9(8), 2007. (Cited on page 24.)

[83] Günter Pappenberger, Annett Bachmann, Rita Müller, Hüseyin Aygün, Joachim W Engels, and Thomas Kiefhaber. Kinetic mechanism and catalysis of a native-state prolyl isomerization reaction. *Journal of molecular biology*, 326(1):235–246, February 2003. (Cited on pages 4 and 12.)

[84] Ulla Pentikainen and Jari Ylänne. The regulation mechanism for the auto-inhibition of binding of human filamin A to integrin. *Journal of molecular biology*, 393(3):644–657, October 2009. (Cited on pages 4 and 10.)

[85] Ulla Pentikainen, Pengju Jiang, Heikki Takala, Salla Ruskamo, Iain D Campbell, and Jari Ylänne. Assembly of a filamin four-domain fragment and the influence of splicing variant-1 on the structure. *The Journal of biological chemistry*, 286(30):26921–26930, July 2011. (Cited on page 64.)

[86] Erwin J G Peterman, Frederick Gittes, and Christoph F Schmidt. Laser-induced heating in optical traps. *Biophysj*, 84(2 Pt 1):1308–1316, February 2003. (Cited on page 27.)

[87] Elias M Puchner, Alexander Alexandrovich, Ay Lin Kho, Ulf Hensen, Lars V Schäfer, Birgit Brandmeier, Frauke Gräter, Helmut Grubmüller, Hermann E Gaub, and Mathias Gautel. Mechanoenzymatics of titin kinase. *Proceedings Of The National Academy Of Sciences Of The United States Of America*, 105(36):13385–13390, September 2008. (Cited on page 64.)

[88] Ziba Razinia, Toni Mäkelä, Jari Ylänne, and David A Calderwood. Filamins in Mechanosensing and Signaling. *Annual review of biophysics*, February 2012. (Cited on pages 7 and 9.)

[89] Ulf Reimer and Gunter Fischer. Local structural changes caused by peptidyl-prolyl cis/trans isomerization in the native state of proteins. *Biophysical Chemistry*, 96(2-3):203–212, May 2002. (Cited on page 77.)

[90] Pere Roca-Cusachs, Nils C Gauthier, Armando del Rio, and Michael P Sheetz. Clustering of alpha(5)beta(1) integrins determines adhesion strength whereas alpha(v)beta(3) and talin enable mechanotransduction. *Proceedings Of The National Academy Of Sciences Of The United States Of America*, 106(38):16245–16250, September 2009. (Cited on page 66.)

[91] Lorenz Rognoni, Johannes Stigler, Benjamin Pelz, Jari Ylänne, and Matthias Rief. Dynamic force sensing of filamin revealed in single-molecule experiments. *Proceedings Of The National Academy Of Sciences Of The United States Of America*, November 2012. (Cited on page vii.)

[92] Lorenz Rognoni, Tobias Möst, Gabriel Zoldak, and Matthias Rief. Force-dependent isomerization kinetics of a highly conserved proline switch modulates the mechanosensing region of filamin. *Proceedings Of The National Academy Of Sciences Of The United States Of America*, April 2014. (Cited on pages vii and 22.)

[93] Scott William Roy and Walter Gilbert. The evolution of spliceosomal introns: patterns, puzzles and progress. *Nature reviews. Genetics*, 7(3):211–221, March 2006. (Cited on page 97.)

[94] Zaverio M Ruggeri, Jennifer N Orje, Rolf Habermann, Augusto B Federici, and Armin J Reininger. Activation-independent platelet adhesion and aggregation under elevated shear stress. *Blood*, 108(6):1903–1910, September 2006. (Cited on pages 3 and 7.)

[95] Bernhard Ryffel, Brian M Foxwell, Andrew Gee, Brigitte Greiner, Gaetane Woerly, and Michael J Mihatsch. Cyclosporine-Relationship of Side Effects to Mode of Action. *Transplantation*, 46(2):90S, August 1988. (Cited on page 89.)

[96] Paramita Sarkar, Charles Reichman, Tamjeed Saleh, Raymond B Birge, and Charalampos G Kalodimos. Proline cis-trans isomerization controls autoinhibition of a signaling protein. *Molecular cell*, 25(3):413–426, February 2007. (Cited on pages 4, 12, and 81.)

[97] Cordelia Schiene-Fischer, Tobias Aumüller, and Gunter Fischer. Peptide Bond cis/trans Isomerases: A Biocatalysis Perspective of Conformational Dynamics in Proteins. *Topics in current chemistry*, May 2011. (Cited on page 81.)

[98] Michael Schlierf, Hongbin Li, and Julio M Fernandez. The unfolding kinetics of ubiquitin captured with single-molecule force-clamp techniques. *Proceedings Of The National Academy Of Sciences Of The United States Of America*, 101(19):7299–7304, May 2004. (Cited on pages 26, 33, and 99.)

[99] Michael Schlierf, Felix Berkemeier, and Matthias Rief. Direct observation of active protein folding using lock-in force spectroscopy. *Biophysical journal*, 93(11):3989–3998, December 2007. (Cited on pages 28 and 35.)

[100] C Scholz, T Schindler, K Dolinski, J Heitman, and F X Schmid. Cyclophilin active site mutants have native prolyl isomerase activity with a protein substrate. *FEBS letters*, 414(1):69–73, September 1997. (Cited on page 13.)

[101] Christian Scholz, Barbara Eckert, Franz Hagn, Peter Schaarschmidt, Jochen Balbach, and Franz Xaver Schmid.

SlyD proteins from different species exhibit high prolyl isomerase and chaperone activities. *Biochemistry*, 45(1):20–33, January 2006. (Cited on pages 14, 15, 16, and 87.)

[102] G Schreiber, G Haran, and H-X Zhou. Fundamental aspects of protein-protein association kinetics. *Chemical reviews*, 109(3): 839–860, March 2009. (Cited on page 16.)

[103] Ingo Schwaiger, Angelika Kardinal, Michael Schleicher, Angelika A Noegel, and Matthias Rief. A mechanical unfolding intermediate in an actin-crosslinking protein. *Nature structural & molecular biology*, 11(1):81–85, January 2004. (Cited on page 60.)

[104] Ingo Schwaiger, Michael Schleicher, Angelika A Noegel, and Matthias Rief. The folding pathway of a fast-folding immunoglobulin domain revealed by single-molecule mechanical experiments. *EMBO reports*, 6(1):46–51, January 2005. (Cited on page 29.)

[105] D E Stewart, A Sarkar, and J E Wampler. Occurrence and role of cis peptide bonds in protein structures. *Journal of molecular biology*, 214(1):253–260, July 1990. (Cited on page 11.)

[106] Johannes Stigler. *Complex Ligand-dependent Folding of Single Proteins Observed with Optical Tweezers*. Dissertation, Technische Universität München, München, 2012. (Cited on page 25.)

[107] Johannes Stigler and Matthias Rief. Hidden markov analysis of trajectories in single-molecule experiments and the effects of missed events. *Chemphyschem : a European journal of chemical physics and physical chemistry*, 13(4):1079–1086, March 2012. (Cited on page 32.)

[108] Johannes Stigler, Fabian Ziegler, Anja Gieseke, J Christof M Gebhardt, and Matthias Rief. The complex folding network of single calmodulin molecules. *Science (New York, NY)*, 334(6055): 512–516, October 2011. (Cited on pages 22, 26, 76, and 102.)

[109] Alexander B Stilgoe, Timo A Nieminen, Gregor Knöener, Norman R Heckenberg, and Halina Rubinsztein-Dunlop. The effect of Mie resonances on trapping in optical tweezers. *Optics Express*, 16(19):15039, 2008. (Cited on page 24.)

[110] G Stoller, K P Rücknagel, K H Nierhaus, F X Schmid, G Fischer, and J U Rahfeld. A ribosome-associated peptidyl-prolyl cis/trans isomerase identified as the trigger factor. *The EMBO journal*, 14(20):4939, 1995. (Cited on page 81.)

[111] K Svoboda and S M Block. Biological applications of optical forces. *Annual review of biophysics and biomolecular structure*, 23: 247–285, 1994. (Cited on page 24.)

[112] Simon F Tolić-Nørrelykke, Erik Schäffer, Jonathon Howard, Francesco S Pavone, Frank Jülicher, and Henrik Flyvbjerg. Calibration of optical tweezers with positional detection in the back focal plane. *The Review of scientific instruments*, 77(10):103101, 2006. (Cited on page 25.)

[113] M Tropschug, I B Barthelmess, and W Neupert. Sensitivity to cyclosporin A is mediated by cyclophilin in Neurospora crassa and Saccharomyces cerevisiae. *Nature*, 342(6252):953–955, December 1989. (Cited on page 13.)

[114] V Tugarinov, A Zvi, R Levy, and J Anglister. A cis proline turn linking two beta-hairpin strands in the solution structure of an antibody-bound HIV-1IIIB V3 peptide. *Nature structural biology*, 6(4):331–335, April 1999. (Cited on pages 4 and 12.)

[115] Alexei Valiaev, Dong Woo Lim, Terrence G Oas, Ashutosh Chilkoti, and Stefan Zauscher. Force-induced prolyl cis-trans isomerization in elastin-like polypeptides. *Journal of the American Chemical Society*, 129(20):6491–6497, May 2007. (Cited on page 75.)

[116] M D Wang, H Yin, R Landick, J Gelles, and S M Block. Stretching DNA with optical tweezers. *Biophysj*, 72(3):1335–1346, March 1997. (Cited on page 76.)

[117] William J Wedemeyer, Ervin Welker, and Harold A Scheraga. Proline cis-trans isomerization and protein folding. *Biochemistry*, 41(50):14637–14644, December 2002. (Cited on pages 4, 11, 12, and 75.)

[118] Rud Wegscheider. Über simultane Gleichgewichte und die Beziehungen zwischen Thermodynamik und Reactionskinetik homogener Systeme. *Monatshefte für Chemie/Chemical Monthly*, 32(8):849–906, 1911. (Cited on page 74.)

[119] Ulrich Weininger, Caroline Haupt, Kristian Schweimer, Wenke Graubner, Michael Kovermann, Thomas Brüser, Christian Scholz, Peter Schaarschmidt, Gabriel Zoldak, Franz X Schmid, and Jochen Balbach. NMR solution structure of SlyD from Escherichia coli: spatial separation of prolyl isomerase and chaperone function. *Journal of molecular biology*, 387(2):295–305, March 2009. (Cited on page 14.)

[120] A Wlodawer, L A Svensson, L Sjölin, and G L Gilliland. Structure of phosphate-free ribonuclease A refined at 1.26 A. *Biochemistry*, 27(8):2705–2717, April 1988. (Cited on page 12.)

[121] Kirk M Wolter. Introduction to Variance Estimation. *Springer-Verlag, New York*, 1985. (Cited on page 33.)

[122] Michael T Woodside, Peter C Anthony, William M Behnke-Parks, Kevan Larizadeh, Daniel Herschlag, and Steven M Block. Direct measurement of the full, sequence-dependent folding landscape of a nucleic acid. *Science (New York, NY)*, 314(5801): 1001–1004, November 2006. (Cited on page 23.)

[123] Yanhong Yuan, Weilin Zhang, Rong Yan, Yi Liao, Lili Zhao, Changgeng Ruan, Xiaoping Du, and Kesheng Dai. Identification of a novel 14-3-3zeta binding site within the cytoplasmic domain of platelet glycoprotein Ibalpha that plays a key role in regulating the von Willebrand factor binding function of glycoprotein Ib-IX. *Circulation research*, 105(12):1177–1185, December 2009. (Cited on page 66.)

[124] Qing Zhang, Yan-Feng Zhou, Cheng-Zhong Zhang, Xiaohui Zhang, Chafen Lu, and Timothy A Springer. Structural specializations of A2, a force-sensing domain in the ultralarge vascular protein von Willebrand factor. *Proceedings Of The National Academy Of Sciences Of The United States Of America*, 106(23): 9226–9231, June 2009. (Cited on page 79.)

[125] Gabriel Zoldak and Franz X Schmid. Cooperation of the prolyl isomerase and chaperone activities of the protein folding catalyst SlyD. *Journal of molecular biology*, 406(1):176–194, February 2011. (Cited on pages 15 and 16.)

[126] Gabriel Zoldak, Tobias Aumüller, Christian Lücke, Jozef Hritz, Chris Oostenbrink, Gunter Fischer, and Franz X Schmid. A library of fluorescent peptides for exploring the substrate specificities of prolyl isomerases. *Biochemistry*, 48(43):10423–10436, November 2009. (Cited on page 76.)

[127] Gabriel Zoldak, Linn Carstensen, Christian Scholz, and Franz X Schmid. Consequences of domain insertion on the stability and folding mechanism of a protein. *Journal of molecular biology*, 386 (4):1138–1152, March 2009. (Cited on page 14.)

[128] Gabriel Zoldak, Anne-Juliane Geitner, and Franz X Schmid. The prolyl isomerase SlyD is a highly efficient enzyme but decelerates the conformational folding of a client protein. *Journal of the American Chemical Society*, 135(11):4372–4379, March 2013. (Cited on pages 15, 85, 86, 87, 89, 90, and 91.)